

Diffusion Magnetic Resonance Imaging of the Human Spinal Cord In Vivo: Feasibility and  
Application of Advanced Diffusion Models

By

Samantha By

Dissertation

Submitted to the Faculty of the  
Graduate School of Vanderbilt University  
in partial fulfillment of the requirements  
for the degree of

DOCTOR OF PHILOSOPHY

in

Biomedical Engineering

August 31, 2017

Nashville, Tennessee

Approved:

Seth A. Smith, Ph.D.

Adam Anderson, Ph.D.

Richard Dortch, Ph.D.

William A. Grissom, Ph.D.

E. Brian Welch, Ph.D.

Copyright © 2017 by Samantha By  
All Rights Reserved

To my parents

## ACKNOWLEDGEMENTS

First and foremost, I would like to thank my Ph.D. advisor Dr. Seth A. Smith. Since day one, your guidance and support have been central to this work. You remind me to always have the bigger picture in mind, but also somehow manage to engage in my pessimistic antics at the same time. I will always be inspired by your enthusiasm and perseverance towards your work. I thank you for your patience, encouragement, and wisdom over the years, but most of all, thank you for being a great role model.

I would like to thank the members of my committee—Drs. Adam Anderson, Richard Dortch, Will Grissom, and Brian Welch. Thank you for all of your insight, time, and encouragement along the way. I am also grateful to our collaborators Drs. Francesca Bagnato and Siddharama Pawate for making the clinical aspect of this dissertation possible. I gratefully acknowledge Drs. Bennett Landman, Junzhong Xu and Saikat Sengupta for always offering their technical expertise. To my lab members – Alex, Kristin, Rob, Bailey, Ben – thanks for providing your support and encouragement, both in and outside of lab. I would also like to thank everyone at VUIIS, who has made my experience a pleasurable one. I'm honored to have received my training at such a renowned institute.

Lastly, I would be remiss not to thank my family and friends for their support. You have always kept me grounded, reminding me of what is important. To my parents, thank you for instilling in me an appreciation for education and a strong work ethic. Max, you have been a constant source of strength. I can't thank you enough for your unconditional support, which has been integral in so many ways.

## TABLE OF CONTENTS

	Page
ACKNOWLEDGEMENTS .....	iv
LIST OF TABLES .....	vii
LIST OF FIGURES.....	viii
 Chapter	
1. Introduction .....	1
1.1 Motivation .....	1
1.2 Approach .....	1
1.3 Innovation.....	2
1.4 Objectives and Outline .....	3
 2. Background .....	5
2.1 Spinal Cord.....	5
2.2 Multiple Sclerosis.....	6
2.3 Diffusion Imaging.....	8
2.4 Challenges in Diffusion Imaging of the Spinal Cord .....	19
 3. Quantifying the Impact of Underlying Measurement Error on Cervical Spinal Cord Diffusion Tensor Imaging at 3T.....	22
3.1 Introduction .....	22
3.2 Methods .....	24
3.3 Results .....	30
3.4 Discussion.....	36
 4. Neurite Orientation Dispersion and Density Imaging: Application to MS.....	40
4.1 Introduction .....	40
4.2 Methods .....	44
4.3 Results .....	48

4.4 Discussion.....	52
5. Spherical Mean Technique: Application to MS.....	55
5.1 Introduction .....	55
5.2 Methods .....	59
5.3 Results .....	61
5.4 Discussion.....	65
6. Diffusion Basis Spectrum Imaging: Application to MS .....	67
6.1 Introduction .....	67
6.2 Methods .....	69
6.3 Results .....	73
6.4 Discussion.....	79
7. Comparison of Biophysical Models to DTI and DKI .....	82
7.1 Introduction .....	82
7.2 Methods .....	83
7.3 Results .....	85
7.4 Discussion.....	92
8. Towards Clinical Applicability: Reducing Scan Times and Increasing Coverage of Multi-Shell Diffusion Protocols.....	96
8.1 Introduction .....	96
8.2 Methods .....	97
8.3 Results .....	99
8.4 Discussion.....	107
9. Conclusions and Future Directions .....	110
BIBLIOGRAPHY .....	113

## LIST OF TABLES

Table	Page
1. Overview of diffusion sequences. ....	25
2. Mean ( $\pm$ standard deviation) of DTI-derived parameters over all participants for both scans at the 9-minute breakdown for white matter (WM) and gray matter (GM). ....	33
3. Summary of NODDI model. ....	43
4. Clinical and demographic characteristics of patients. ....	44
5. Reproducibility metrics for NODDI. ....	50
6. Summary of SMT model. ....	58
7. Reproducibility of SMT-derived indices. ....	63
8. Summary of DBSI model. ....	70
9. Reproducibility of DBSI-derived indices. ....	75
10. Reproducibility metrics for DKI and DTI. ....	86
11. BIC of NODDI, SMT and DKI. ....	91
12. Summary of Reduced Acquisition Schemes. ....	97

## LIST OF FIGURES

Figure	Page
1. Axial view of the spinal cord, highlighting major components. ....	5
2. Heterogeneity of MS. ....	7
3. Free, hindered, and restricted diffusion. ....	9
4. Schematic of pulsed gradient spin echo (PGSE) diffusion sequence. ....	10
5. Overview of diffusion models. ....	17
6. Outer volume suppression with diffusion sequence. ....	19
7. Cardiac triggering parameters. ....	20
8. Flowchart describing image processing scheme. ....	27
9. Additional ROIs overlaid on mFFE for error map processing. ....	29
10. DTI maps of a representative healthy volunteer acquired from different gradient schemes at different scan time equivalents. ....	31
11. Error bias maps, calculated as the difference from the gold standard, using all control data for gradient schemes of 6, 15 and 32 directions at 4.5, 9, and 18 minutes. ....	35
12. Examples of ROI identification. ....	46
13. Maps and histograms of fitted parameters using NODDI in controls. ....	49
14. Example images from NODDI. ....	51
15. Comparison of $v_{in}$ , $v_{iso}$ , and ODI. ....	52
16. Varying tissue geometries and effect on $\mu$ FA and FA. ....	56
17. Mean SMT-derived maps and reproducibility in controls. ....	62
18. Anatomical images (top), SMT-derived maps $v_{ax}$ (middle) and $D_{ax}$ (bottom) are displayed for control (left) and two patients. ....	64
19. Application of SMT in MS cohort. ....	64
20. DBSI-derived maps and histograms. ....	74
21. Anatomical images (top), with DBSI-derived maps following, are displayed for control (left) and two patients (right). ....	76
22. Boxplots highlighting group trends for DBSI-derived indices in healthy controls and MS patients. ....	78
23. Goodness-of-fit comparison for healthy control and MS patient. ....	79



24. Example images from DKI. ....	87
25. Comparison of MK, AK and RK. ....	87
26. Example images from DTI. ....	88
27. Comparison of FA, MD, AD and RD. ....	89
28. Contrast in diffusion maps. ....	90
29. Comparison of NODDI and DKI fit. ....	92
30. Effect of reduced acquisition schemes on NODDI-derived parameters. ....	100
31. Effect of reduced acquisition schemes on NODDI in MS patient. ....	101
32. Effect of reduced acquisition schemes on SMT-derived parameters. ....	102
33. Effect of reduced acquisition schemes on SMT in MS patient. ....	103
34. SNR dependency with slice gap. ....	103
35. Comparison of half, multi-slice, and multiband acquisition. ....	104
36. NODDI-derived indices for the comparing schemes for the same slice. ....	105
37. SMT-derived indices for the comparing schemes for the same slice. ....	107

# CHAPTER 1

## Introduction

### 1.1 Motivation

The spinal cord is a vital organ in the central nervous system (CNS) and is responsible for all communication between the brain and the peripheral nervous system. Electrical signals are transmitted up and down the spinal cord via distinct bundles of axonal tracts located in the white matter to convey sensory and motor information. Damage to these axons, possibly by neurodegenerative disease or trauma, can be devastating and may result in irreversible loss of neurological function. One such example is in multiple sclerosis (MS), an autoimmune disease that is marked by inflammation, demyelination, gliosis and axonal loss (1). While conventional magnetic resonance imaging (MRI) techniques can point to the location of the damage (2), these techniques do not typically offer specific information on the microscopic pathology of the tissue, such as axonal loss and myelin damage. Therefore, there is a need for advanced noninvasive MRI techniques that are sensitive to specific aspects of MS pathology in the spinal cord to understand its development and degeneration in vivo, which could have significant clinical implications on diagnosis and treatment of the disease.

### 1.2 Approach

Quantitative MRI measurements, and in particular diffusion imaging, may reveal further microstructural insight on specific fiber bundles in the cervical spinal cord, which would be useful in the diagnosis and management of neurodegenerative diseases. Diffusion imaging has become a rapidly growing area of study, offering significant insight into microstructural abnormalities in MS. With diffusion MRI, the signal is sensitive to the random motion (displacement) of water molecules, which are restricted and/or hindered by fibrous structures or barriers (e.g. cell and axon membranes and myelin sheaths). Therefore, diffusion MRI offers an opportunity to indirectly probe microstructural integrity. However, the majority of diffusion MRI in the literature relies on the utilization of a simple model that summarizes all water compartments within the tissue of interest. Clinically, the most conventionally used model is the

diffusion tensor (diffusion tensor imaging, DTI), which models heterogeneous water displacement with a single three-dimensional tensor (3). While DTI has demonstrated sensitivity to changes in tissue microstructure such as demyelination and axonal loss (4-6), a major drawback is that DTI does not account for structural heterogeneity and is affected by multiple confounding tissue properties, resulting in reduced specificity of the derived indices to pathologic variations of clinical importance. Additionally, DTI assumes that the underlying probability distribution function of diffusion is Gaussian, which is not true due to the restricted nature of diffusion in axons, especially when higher b-values are used (7,8). Diffusion kurtosis imaging (DKI) has been introduced to quantify the degree of non-Gaussianity of the probability density function with the kurtosis (9), but it still suffers from limitations of probing specific tissue compartments. Other groups have developed biophysical diffusion models – models consisting of multiple compartments in order to more accurately characterize the diffusion signal in the presence of multiple tissue compartments or milieu (10-17). Unlike the signal models such as DTI or DKI, biophysically based methods can provide indices related to specific compartments of white matter microstructure. However, with biophysical models, often times assumptions need to be specified in order to simplify the complexity of the models, and it is difficult to simplify assumptions for a large cohort of patients.

### **1.3 Innovation**

Currently, there is a lack of diffusion techniques optimized for the spinal cord in vivo. While many of the aforementioned techniques have been successfully implemented in the brain, application to the cervical spinal cord has been hampered due to its small size, in addition to physiological challenges from the cardiac and respiratory cycles (18). Furthermore, while biophysical models offer the potential to distinguish specific aspects of MS pathology, very few studies have investigated their utility in the spinal cord of MS. In particular, we will investigate the sensitivity of neurite orientation dispersion and density imaging (NODDI), spherical mean technique (SMT), and diffusion basis spectrum imaging (DBSI) in the cervical segment of the spinal cord.

## 1.4 Objectives and Outline

The central hypothesis of this work is that diffusion MRI techniques can be developed and optimized to provide high sensitivity to microstructural changes in the cervical spinal cord, potentially serving as biomarkers for MS. The hypothesis will be evaluated through the completion of the following aims:

Aim 1: Develop and optimize existing DTI techniques for the cervical spinal cord.

Aim 2: Develop multi-shell diffusion techniques for the cervical spinal cord.

Aim 3: Optimize multi-shell diffusion techniques for translation to clinical implementation.

Following an introduction to the subject matter, the dissertation chapters will be divided based on each aim. Chapter 2 will include a brief description of the spinal cord and MS. An introduction to diffusion MRI will be provided, and the chapter will end with a summary of the challenges and current state of diffusion MRI in spinal cord imaging.

Chapter 3 discusses the first aim, reporting the development and optimization of existing DTI techniques for the spinal cord in terms of gradient direction scheme and acquisition time for high accuracy and reproducibility. In doing so, the bias and SNR dependency in DTI measurements will be understood, and an empirical framework for spinal cord diffusion will be established.

The remainder of this dissertation will focus on more advanced multi-shell, biophysical diffusion models by exploring their use in both healthy controls and MS patients. First (Chapter 4), the NODDI model will be explored by implementing this model in a cohort of healthy controls in order to assess the feasibility and reproducibility of this technique. The NODDI model will then be applied in a cohort of patients with MS to assess its ability to detect white matter pathology. SMT (Chapter 5) and DBSI (Chapter 6) will next be assessed in a similar manner. In Chapter 7, these models will then be compared against one another and to signal models (i.e. DTI and DKI), with the main goal of determining whether multi-compartmental and biophysically based models are more sensitive to microstructural changes than signal models.

Chapter 8 covers the optimization of the multi-shell diffusion models (from Chapters 4-6) for clinical applicability. With an eye to deploy these sequences to the clinic, data reduction strategies, along with multiband excitation, will be implemented to shorten acquisition times and increase coverage of these methods.

Finally, Chapter 9 will summarize the major results of this work and include a discussion of broader impacts and future directions.

## CHAPTER 2

### Background

#### 2.1 Spinal Cord

The spinal cord is a vital organ of the central nervous system (CNS), serving as a conduit for motor and sensory information to the periphery. Essentially, the spinal cord is a long, cylindrical bundle of nerve fibers that sits in a bath of cerebrospinal fluid, enclosed and protected by vertebral bodies and intervertebral discs. It is split into four main regions, segmented by the location of the vertebrae, all with varying lengths: cervical (C1-C7), thoracic (T1-T12), lumbar (L1-L5) and sacral (S1-S5). Figure 1 shows an axial view of the spinal cord at the C3/C4 level.

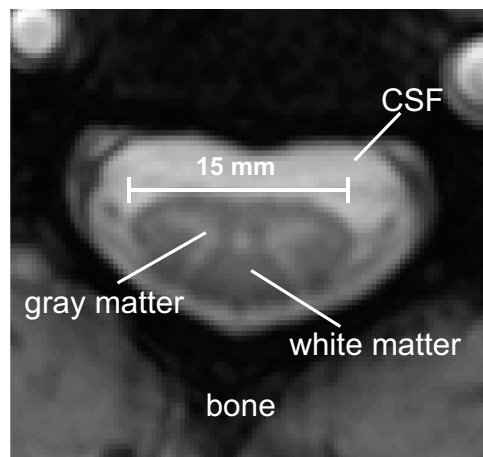


**Figure 1: Axial view of the spinal cord, highlighting major components.** A butterfly-shaped gray matter region can be found in the center of the cord, surrounded by densely packed white matter.

At the cervical level, the cord is only 1.5 cm in diameter and it is divided into two main regions. A butterfly-shaped gray matter region can be found in the center of the cord surrounded by densely packed white matter. The gray matter, comprised of interneurons and cell bodies, is split into three different columns (anterior, posterior, lateral). The white matter primarily consists of myelinated motor and sensory axons, which are bundled together to form tracts. Importantly, the spinal cord is somatotopically organized: sensory neuron cell bodies are found in the dorsal root ganglia and ascend the spinal cord for touch, vibration, and proprioception, while motor

function is passed to the extremities via descending tracts located primarily in the lateral column of the spinal cord.

## **2.2 Multiple Sclerosis**

### *2.2.1. Overview*

Multiple sclerosis (MS) is a chronic disease of the CNS that affects approximately 400,000 people in the United States alone and over 2.5 million worldwide (19). Though the exact cause of MS is unknown, what is known is that the disease is marked by a myriad of changes including demyelination, inflammation, gliosis and axonal loss (1). Concomitantly, the damage to the CNS from these mechanisms results in an accumulation of sensorimotor impairment (20). Patients often exhibit symptoms of poor coordination, tremor, bladder dysfunction and motor impairment (21), and these symptoms are summarized by a clinical score of disability known as the Expanded Disability Status Scale (EDSS) (22).

A complicating factor of MS is that the disease course and symptomatology is heterogeneous, temporally varying and constantly evolving. The first episode when a patient exhibits neurological symptoms is known as clinical isolated syndrome (CIS), which is suggestive of demyelination and/or inflammation. A patient exhibiting CIS does not necessarily meet the criteria for diagnosis of MS, and many patients with CIS may not develop MS later on. The most common form of MS is relapsing-remitting MS (RRMS), which is characterized by recurring bouts of relapse and remission. Primary progressive MS (PPMS) is characterized by more gradual decline in disability without any remissions. Patients who are initially diagnosed with RRMS and eventually transition into more progressively accumulating disability are referred to as secondary progressive MS (SPMS). The patient subtypes are summarized in Figure 2.

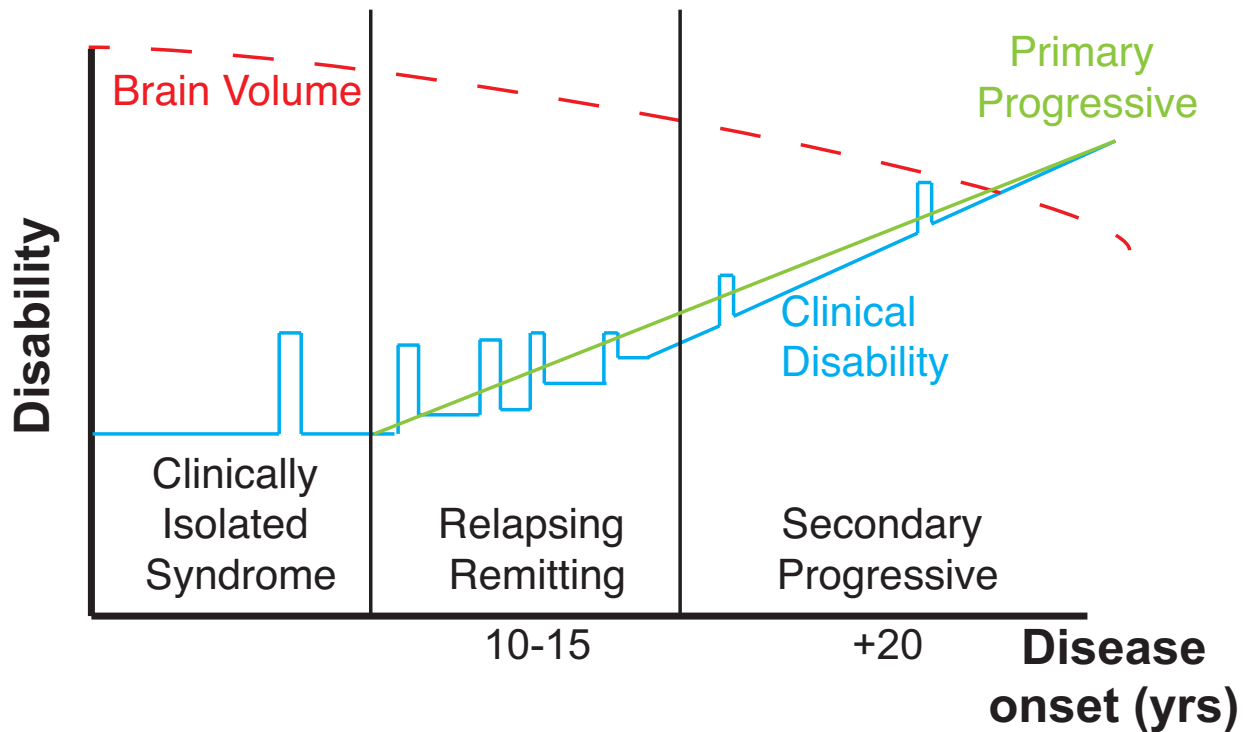


**Figure 2: Heterogeneity of MS.** Clinical disability plotted against disease onset highlights the patterns of different MS subtypes. The most common type of MS is relapsing remitting MS (RRMS), where patients experience recurring bouts of relapse and remission; eventually some patients gradually transition into secondary progressive MS (SPMS), where remission wanes and clinical disability increases. Primary progressive MS (PPMS) is another subtype of MS, where patients experience progressive decline from the onset of disease and do not experience episodes of relapse and remission. Adapted from (1).

### 2.2.2 Immunopathology

MS is a result of an immune-mediated process. A trigger is provoked, causing a disruption of the blood brain barrier (BBB) and consequently, an activation of peripheral T cells to enter into the CNS. This initiates a cascade of inflammatory events, involving activation of B cells and innate immune cells (monocytes, macrophages, microglia). These immune-mediated responses are known to result in demyelination and axonal injury (23). Histological findings of MS lesions indicate that axonal damage occurs at all stages of the disease (24), with studies involving  $\beta$ -amyloid precursor protein ( $\beta$ -APP) immunoreactivity reporting axonal damage in acute plaques (25) in addition to damaged axons at the borders of chronic active plaques (26).



### 2.2.3 Role of MRI in MS

MRI has become a powerful tool in diagnosing and evaluating MS, with the McDonald MS diagnostic criteria requiring demonstration of dissemination of lesions in space and in time (27). For the spinal cord specifically, up to 90% of MS patients exhibit spinal cord lesions (28). There exists, however, a clinical-radiological paradox (29), which refers to the poor association between radiologically-detected lesion load and clinical physical disability. This paradox can primarily be attributed to the fact that conventional MRI techniques, such as T<sub>1</sub>-weighted, T<sub>2</sub>-weighted, and Short T<sub>1</sub> Inversion Recovery (STIR) imaging are sensitive to a combination of several pathological conditions and lack the ability to provide pathology-specific information. Therefore, quantitative MRI techniques, such as diffusion, that are sensitive to specific pathologies may address this paradox.

## 2.3 Diffusion Imaging

The first credited observation of diffusion dates back to 1827, when botanist Robert Brown observed the jostling of pollen grains in water, but at the time, the underlying mechanisms of this motion were not well understood. In 1905, Albert Einstein introduced the concept of diffusion (also termed Brownian motion) (30), describing the phenomena as the random motion of the molecules due to thermal agitation following the equation:

$$RMSD = \sqrt{2Dt} \quad (1)$$

where *RMSD* is the one-dimensional root mean squared displacement and *D* is the diffusion coefficient over a period of time *t*. Interestingly, however, though often unaccredited, Lucretius had accurately described Brownian motion almost 1900 years prior in 60 BC in his poem “On the Nature of Things”, and in 1785, Jan Ingenhousz also observed diffusion through the motion of coal in alcohol.

The diffusion coefficient of a molecule is affected by the molecular weight, viscosity, and temperature. As highlighted in Figure 3, in an unhindered or “free” medium, the RMSD will follow a Gaussian distribution; in a restricted medium or a closed space, however, the displacement is no longer Gaussian and the actual RMSD will be reduced. For a hindered space,

the actual RMSD will be reduced in comparison to a free medium, but does not reach a maximum displacement as with restricted diffusion. In biological tissue, where water molecules can still diffuse freely at very short times, but will encounter more and more microscopic restrictions as time increases (due to the presence of cell walls or membranes, fibers, axonal myelin sheaths, macromolecules, etc.), the motion of the water molecules can be impeded (Figure 3b) (31). As a result, diffusion becomes time and direction dependent, or anisotropic, in biological tissue. These basic concepts serve as the theoretical framework for diffusion MRI, which provides the ability to probe the microstructural integrity of tissue by assessing the geometrical barriers to water displacement.

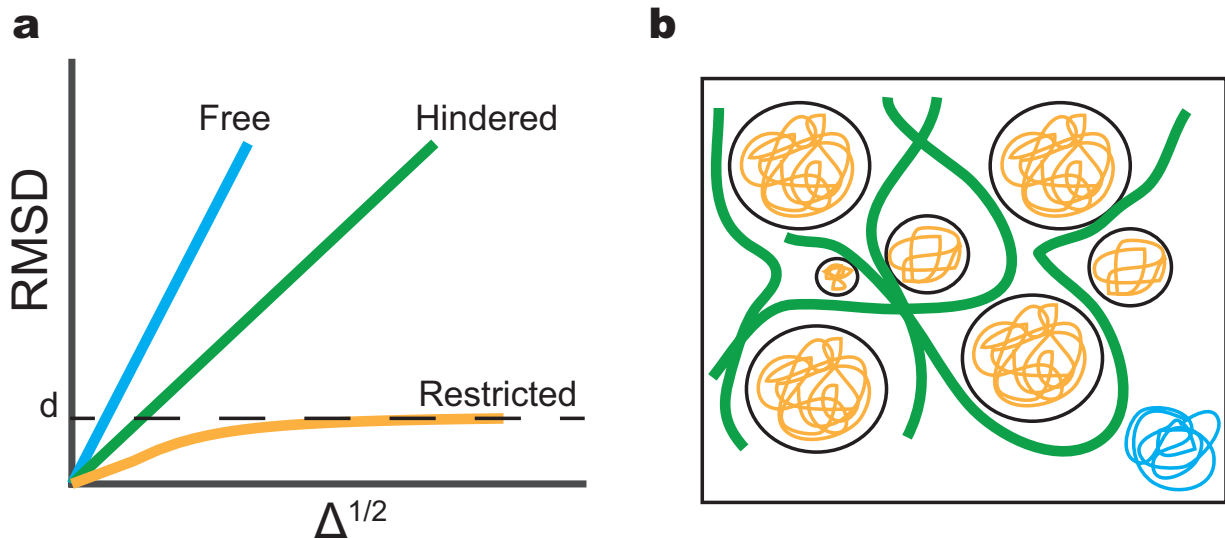


**Figure 3: Free, hindered, and restricted diffusion.** (a) For free diffusion, the 1D RMSD displaces linearly with the diffusion time  $\Delta$ . With hindered diffusion, the RMSD increases less than free diffusion, since there are barriers to diffusion. When diffusion is restricted (such as by cell walls or membranes), the RMSD plateaus at the size of the restriction  $d$ . (b) Free, hindered, and restricted diffusion are depicted in blue, green, and yellow respectively. Adapted from (32).

### 2.3.1 Measuring Diffusion in MRI

Given the time scales of MRI (on the order of milliseconds), diffusion MRI is well suited to measure the displacement of water molecules on the scale of microns. Diffusion is captured in

MRI using the Stejskal-Tanner pulsed gradient spin echo (PGSE) sequence (33), where a pair of bipolar diffusion gradients is placed around a 180° refocusing pulse, as shown in Figure 4. The diffusion gradients are characterized by direction, strength  $G$ , duration  $\delta$  and separation  $\Delta$ . The first gradient is used to spatially encode spins, while the second gradient pulse reverses this. If the spins remain stationary, the phase accrued after the first gradient would be reversed and magnetization would be restored. When diffusion is present, however, the spins move, and the second gradient reverses the phases incompletely, producing a phase dispersion and loss of signal proportional to the net displacement of spins. Since diffusion of water molecules in vivo is affected by the microstructure of neural tissues, diffusion MRI can assess structural changes due to pathology.

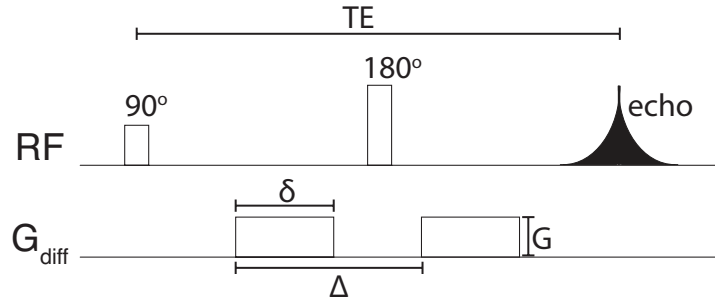


**Figure 4: Schematic of pulsed gradient spin echo (PGSE) diffusion sequence.** A pair of bipolar gradients is placed around the refocusing pulse to encode diffusion, with strength  $G$ , duration  $\delta$  and separation  $\Delta$ . For demonstration purposes, diffusion gradients are only applied in one direction.

To account for the relaxation due to diffusion, the Bloch equations (34) were extended to the Bloch-Torrey equations (35), which describes the evolution of the total magnetization with diffusing water molecules:

$$\frac{\partial \mathbf{M}}{\partial t} = \gamma \mathbf{M} \times \mathbf{B} - \frac{M_x \vec{i} + M_y \vec{j}}{T_2} + \frac{(M_0 - M_z) \vec{k}}{T_1} + \nabla \cdot \mathbf{D} \nabla \mathbf{M} \quad (2)$$

where  $M$  is the magnetization vector  $M = (M_x, M_y, M_z)$  in the laboratory frame of reference,  $\gamma$  is the gyromagnetic ratio,  $T_1$  is the longitudinal relaxation time,  $T_2$  is the transverse relaxation time, and  $D$  is the diffusion tensor, which is introduced in the following section (Section 2.3.3).

### 2.3.2 Diffusion Weighted Imaging (DWI)

In 1985, Le Bihan presented the first diffusion MRI studies of the brain in vivo (36,37), introducing the concept of the apparent diffusion coefficient (ADC). For the isotropic diffusion case, the Bloch-Torrey equations can be simplified with respect to the rotating frame, such that the observed signal attenuation can be characterized by:

$$M_{xy} = M_0 e^{-t/T_2} e^{-bD} \quad (3)$$

where  $M_{xy}$  is the transverse magnetization,  $M_0$  is the magnetization after excitation,  $D$  is the apparent diffusion coefficient and  $b$  is known as the  $b$ -value and determines the diffusion-weighted factor:

$$b = \gamma^2 \int_0^{TE} \left[ \int_0^t G(t') dt' \right]^2 dt \quad (4)$$

For the Stejskal-Tanner sequence, the  $b$ -value can be summarized in terms of gradient duration  $\delta$  and gradient spacing  $\Delta$ :

$$b = \gamma^2 \delta^2 G^2 (\Delta - \delta/3) \quad (5)$$

Thus, From Equation 3, it can be easily recognized that the orientation-dependent ADC can be recovered by simply acquiring one diffusion-weighted image, along with a non-diffusion-weighted image ( $b_0$  image or  $S_0$  image), and the diffusion-weighted signal can be characterized as:

$$S = S_0 e^{-bD} \quad (6)$$

where  $S_0$  is the non-diffusion-weighted baseline.

### 2.3.3 Diffusion Tensor Imaging

In 1994, Basser et al. introduced the tensor formalism (3), allowing quantification of

diffusion properties to be orientation independent. Anisotropic diffusion is sensitive to different directions and requires a diffusion tensor, a 3x3 covariance matrix that defines diffusion along each axis and relates the displacements along these axes:

$$D = \begin{bmatrix} D_{xx} & D_{yx} & D_{zx} \\ D_{xy} & D_{yy} & D_{zy} \\ D_{xz} & D_{yz} & D_{zz} \end{bmatrix} \quad (7)$$

where  $D_{ij}$  is the correlation of the molecular displacements along the given axes. Assuming symmetry ( $D_{ij} = D_{ji}$ ), the tensor can be reduced to only the diagonal terms and a pair of the off diagonal elements. To solve for the six unknowns in the diffusion tensor, Equation 6 can be modified as:

$$\ln\left(\frac{S}{S_0}\right) = - \sum_{i=1}^3 \sum_{j=1}^3 b_{ij} D_{ij} \quad (8)$$

where the diffusion coefficient is replaced with the diffusion tensor, and  $b_{ij}$  is the  $ij$ -th component of the b-matrix (38).

With at least six gradient directions and one non-diffusion-weighted image, the eigensystem can then be solved, where eigenvectors  $v_1, v_2, v_3$  represent the major and minor axes of the ellipsoid of the resulting fit and  $\lambda_1, \lambda_2, \lambda_3$  are the corresponding rotationally invariant eigenvalues indicating the apparent diffusivities. These eigenvalues are combined to yield four different indices:

$$\text{Fractional Anisotropy (FA)} = \sqrt{\frac{1}{2} \sqrt{\frac{(\lambda_1 - \lambda_2)^2 + (\lambda_1 - \lambda_3)^2 + (\lambda_2 - \lambda_3)^2}{\lambda_1^2 + \lambda_2^2 + \lambda_3^2}}} \quad (9)$$

$$\text{Mean Diffusivity (MD)} = \frac{\lambda_1 + \lambda_2 + \lambda_3}{3} \quad (10)$$

$$\text{Axial Diffusivity (AD)} = \lambda_{\parallel} = \lambda_1 \quad (11)$$

$$\text{Radial Diffusivity} = \lambda_{\perp} = \frac{\lambda_2 + \lambda_3}{2} \quad (12)$$

For a more intuitive description, FA is a measure of eccentricity of the diffusion tensor;

MD represents the average diffusion in a voxel irrespective of direction; AD is the diffusion parallel to the direction of the largest diffusion (generally parallel to the axon fibers); and RD is the diffusion perpendicular to the direction of largest diffusion.

DTI of the spinal cord has been of interest, especially in the study of MS. Ex vivo and animal studies of the spinal cord have demonstrated the feasibility in using these parameters to detect pathological hallmarks of MS including inflammation, demyelination, gliosis and axonal loss (39-41). FA and AD have been linked to axonal loss (6,42), RD to demyelination (4,40), and MD to inflammation and gliosis (43). Several studies have also explored the effect of DTI-derived indices in MS in the spinal cord in vivo. In initial studies, DTI was acquired in the sagittal plane, where a decrease in FA and a slight increase in MD were observed in PPMS patients in comparison to healthy controls (44). Another study later performed histogram analysis of the cervical cord in MS patients of different subtypes (SPMS, RRMS, healthy) (45), reporting a larger decrease in FA in the cord in patients with greater disability. This study was followed up with a longitudinal study of 42 patients of varying subtypes, and demonstrated that the baseline FA correlated with increased disability at a mean follow-up of 2.4 years (46).

More recent studies have performed DTI in the axial plane in order to evaluate tract-specific information. In a study of 24 RRMS patients, Hesseltine et al. demonstrated lower FA values in the lateral, posterior and central columns of the spinal cord, which were otherwise normal-appearing in anatomical imaging (47). Expanding on this, Oh et al. performed a large clinical study of 129 patients (5), where they underwent quantitative sensorimotor function testing along with spinal cord MRI at the C3/C4 level. Differences were observed between MS and healthy controls, in addition to differences between progressive and RRMS subtypes. Interestingly, the authors also report that MD, AD, and RD all showed strong correlation with hip flexion strength, and FA showed strong correlation to vibration sensation threshold.

#### *2.3.4 Other Signal Models*

The diffusion tensor model is only valid when assuming the water signal decay is mono-exponential; however, it has been well known that at sufficiently high  $b$ -values ( $b > 2500$  s/mm<sup>2</sup>), the water signal decay in vivo in diffusion sequences is non-mono-exponential (48).  $Q$ -space is an alternative approach for diffusion, where unlike conventional DTI, the underlying probability density function (PDF) of diffusion is not assumed to be Gaussian.  $\vec{q}$  is a reciprocal spatial vector

and is defined as:

$$\vec{q} = \frac{1}{2\pi} \gamma \delta \vec{G}_d [cm^{-1}] \quad (13)$$

Though  $\vec{q}$  is independent of  $\Delta$ , the gradient timing affects the actual displacement measured. In order to obtain the displacement profile, the short gradient pulse approximation, where  $\delta \ll \Delta$  ( $\delta \sim 0$ ) (49), must be met. This ensures that diffusion during the pulse is minimal and will not influence the PDF.

The displacement PDF is dependent on the diffusion gradient direction applied, and the displacement PDF elements can be solved by linearly combining the measured displacement PDFs acquired from different gradient diffusion directions. Therefore, the displacement PDF is influenced by the integrity of the microstructure in a particular direction. For a given diffusion, a tall, narrow PDF infers a low diffusion constant (restricted), whereas a low, broad PDF indicates a high diffusion constant (unrestricted) (50,51).  $Q$ -space offers four different contrasts. The shape of the PDF is characterized by the maximum height (zero displacement probability, ZDP) and full width at half maximum (FWHM). The ZDP is inversely related to the FWHM and identifies the number of molecules diffusing a short distance or not diffusing at all. FWHM is correlated to the spacing between diffusion barriers, and it has been demonstrated that the mean axon diameter can therefore be inferred from the FWHM (52,53). Additionally the PDF can be further characterized by the RMSD and kurtosis excess (KE).

Due to the sufficiently long diffusion times,  $q$ -space appears to be sensitive to the slow diffusing component (8), but the biophysical interpretation of the slow and rapid diffusing compartments still remains unclear (54). It is expected that demyelination can be observed with  $q$ -space and used as a biomarker for disease. Experiments using animal models with demyelinating tissue and a feasibility study including four MS patients have demonstrated a dramatic decrease in the magnitude of the slow diffusing component in the cervical spinal cord, resulting in a reduced weighting and a broadening of the narrow displacement component (50,55,56). Specifically, the diffusion measured perpendicular to the fiber direction demonstrated similar findings to histological staining in demyelinating models (56). Assaf et al. also used  $q$ -space imaging to measure the displacement of water molecules in the rat spinal cord in vitro, reporting measures of 2-3 microns for white matter (52). Similarly, Ong et al. used the FWHM to

infer axon diameters of ex vivo mouse spinal cord, which demonstrated high correlation to histology measures (57). While promising, the use of q-space on clinical scanners is challenging due to current hardware limitations. With q-space, high diffusion weighting is required which can reduce the signal-to-noise ratio (SNR) of the images, a tradeoff which must be considered when gradient strengths of only about 60 mT/m is available.

Diffusion kurtosis imaging (DKI) is another method that addresses the non-Gaussianity behavior of diffusion in white matter microstructure at higher b-values and may provide more specific insight on restricted diffusion in axons. With DKI, the degree of non-Gaussianity of the probability density function is quantified with the kurtosis (9), using the relationship:

$$\ln[S(b)] = \ln[S_0] - bD + \frac{1}{6}b^2D^2K \quad (14)$$

where  $b$  is the b-value,  $D$  is the apparent diffusion coefficient as described above, and  $K$  is the apparent kurtosis or the fourth-order tensor in 3D. The kurtosis can be used to calculate contrasts including the mean kurtosis (MK), axial kurtosis (AK), and radial kurtosis (RK). For clarity, the kurtosis estimates the non-Gaussian nature of a distribution, where MK indicates the average diffusion kurtosis over all directions; AK indicates the diffusion kurtosis along the primary axis of the kurtosis tensor and is typically low in healthy white matter tissue since the diffusion along axons is relatively unrestricted; RK indicates the diffusion kurtosis along the axis perpendicular to the primary axis of the spinal cord and is typically high in healthy tissue due to the more heterogeneous pattern in the presence of myelin sheaths (58).

Raz et al. demonstrated the feasibility and utility of DKI in the spinal cord of MS patients, where a significant decrease in MK was observed (59). A preliminary ex vivo study was conducted using the spinal cord of four experimental autoimmune encephalomyelitis (EAE) rats, reporting a significant difference in AK and RK between healthy tissue and lesions (60).

While q-space and DKI signal models have demonstrated utility over conventional DTI (61), these models still suffer from limitations of probing specific tissue compartments.

### 2.3.5 Biophysical Models

More advanced biophysical models have been developed to account for the non-monopexponential behavior of diffusion MRI observations in vivo and importantly, in pathology. These



biophysical models vary in complexity. Some of the earlier models that were introduced involved a bi-exponential fit of two compartments, but assigning slow and fast components to intra- and extracellular spaces have been met with difficulty (48,54,62). Pioneering the idea of decomposing the diffusion-weighted signal into various geometric components, Stanisz et al. (14) proposed a three-compartment model for the bovine optic nerve consisting of glial cells as spheres, axons as ellipsoids, and the extracellular space with apparent diffusivities calculated using a tortuosity model. While promising, the complexity of this model requires high quality data and long scan times, which can be challenging in patient populations in vivo. Another approach, which models the observed signal by diffusion physical processes, is used in the composite hindered and restricted model (CHARMED), consisting of an intracellular compartment of restricted diffusion and extracellular compartment of hindered diffusion (13) and yields estimates of the volume fractions for each compartment. Although other methods using different diffusion acquisitions have also been reported such as double-pulsed field gradient (d-PFG) (63) and oscillating gradient spin echo (OGSE) (17), the majority of advanced biophysical diffusion models are based on multi-compartment models, like CHARMED, but have been extended to provide information on other tissue features. Such examples include a free water (e.g., cerebrospinal fluid [CSF]) component in the minimal model of white matter diffusion (MMWMD) (64), the axon diameter distribution in AxCaliber (12), the characterization of both white and gray matter in a neurite model (65), inference of the axon orientation with diffusion kurtosis imaging in the white matter tract integrity (WMTI) (66), cellularity of glial and other cells in diffusion basis spectrum imaging (DBSI) (67) and neurite orientation dispersion and density using NODDI (10). Recently, the spherical mean technique (SMT) has been proposed to model the microscopic diffusion process (68,69), enabling the ability to map the neurite density and compartment diffusivities without the confounding influence of fiber orientation dispersion. Figure 5 provides an overview of the potential diffusion models, evolving from signal models to biophysical models. This is only a small reflection of the many possible combinations of biophysical models available, and the reader can refer to studies conducted by Panagiotaki et al. and Ferizi et al. for a larger description and taxonomy of such models in the rat and human brain (70-72).

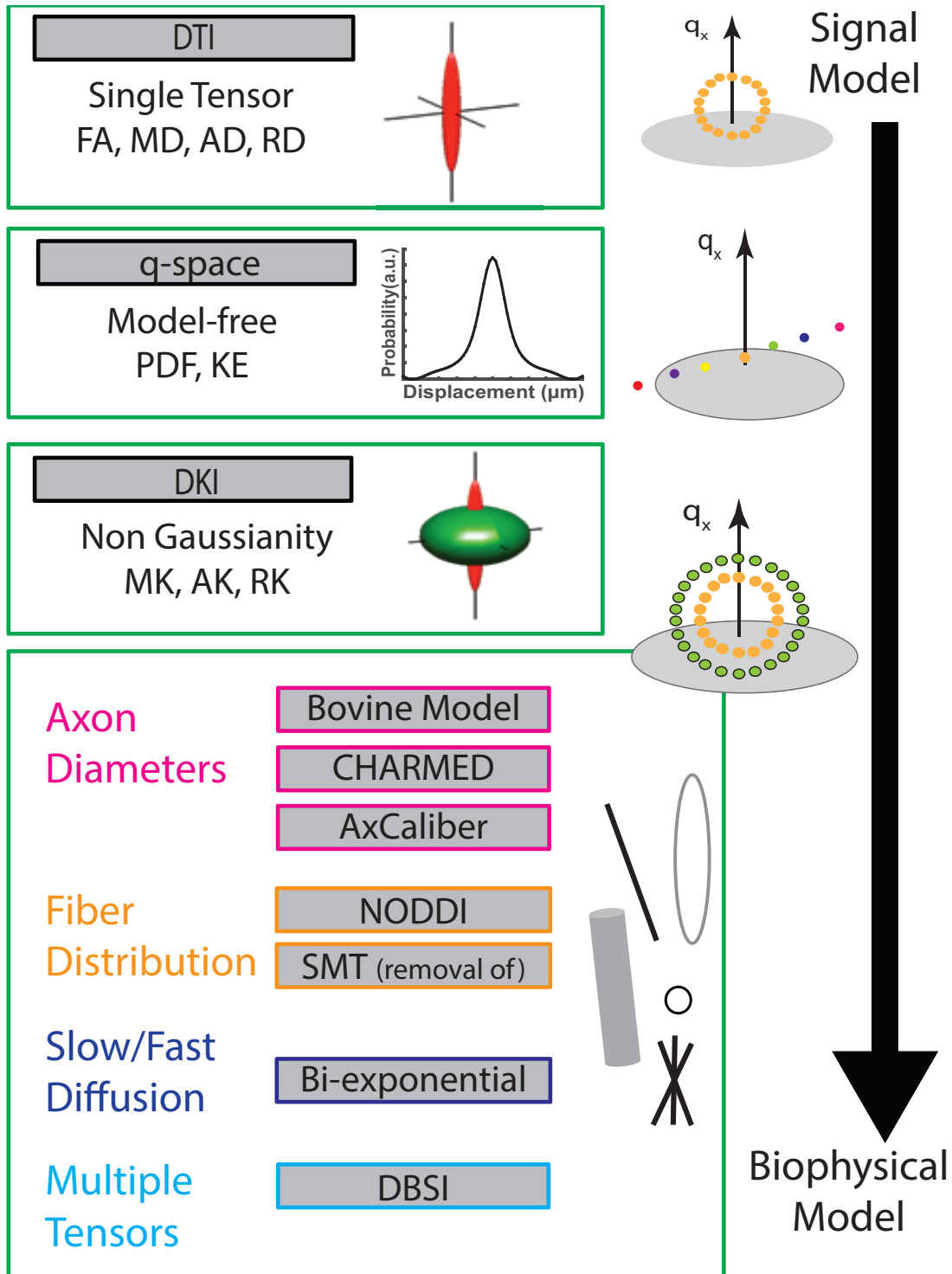


**Figure 5: Overview of diffusion models.** The most conventional model is the diffusion tensor model, which uses a single tensor to model diffusion. Other signal models have been proposed to characterize deviations from the tensor, such as q-space and DKI. Biophysical models have been proposed to obtain a more specific representation of the derived indices, such as axon diameters, fiber distribution, and compartmental volume fractions, and vary in complexity.

There has been increased interest in the application of biophysical diffusion models, ranging from histological validation in animals to human application in vivo. It is important to note that the derived indices of biophysical models are only estimates and not absolute values, and therefore interpretation of these indices should be taken with care and also rely on studies where histological validation of these techniques have been performed. Of importance, Jespersen et al. performed ex vivo multi-shell diffusion in a rodent model, comparing the validation of a biophysical neurite model to the conventional diffusion tensor model using histological measures (73). The axonal volume fraction derived by optical staining correlated very highly with the neurite density from the biophysical model ( $\rho=0.97$ ,  $p=0.0004$ ); furthermore, this correlation was stronger than correlations comparing DTI-derived FA ( $\rho=0.93$ ,  $p=0.002$ ) and DKI-derived MK ( $\rho=0.65$ ,  $p=0.1$ ). Grussu et al. investigated the correlation of histological indices with NODDI-derived indices for a human spinal cord with MS ex vivo, demonstrating decreased orientation dispersion index (ODI) and intra-axonal volume fractions in the white matter lesions when compared to normal appearing white matter (NAWM) (74). A high correlation was observed between intra-axonal volume fraction and myelin staining index ( $r=0.84$ ,  $p<0.005$ ), along with a high correlation between ODI and circular variance for silver staining ( $r=0.96$ ,  $p<10^{-3}$ ). Similarly, Grussu et al. demonstrated the feasibility and reproducibility of NODDI-derived metrics in the healthy cervical spinal cord, enabling the estimate of indices more specific to neurite morphology than DTI (75).

Several ex vivo and animal studies have been performed for DBSI, such as the optic nerve in an EAE model (11), ex vivo mouse spinal cord (76), the corpus callosum of mice in vivo and fixed trigeminal nerve of mice (67), and autopsied MS spinal cord specimens (77), however, human in vivo applications have been limited to the brains of MS patients (77) and the in vivo spinal cord of cervical spondylotic myelopathy (CSM) patients (78).

Assaf et al. have previously measured axon diameters using AxCaliber in a porcine spinal cord with good agreement to histology (12). While promising, estimation of axon diameters is limited by the gradient strength, and implementation of AxCaliber in the human spinal cord in vivo (79) has only been demonstrated on the Human Connectome gradients (80).

To date, the aforementioned studies are the only in vivo studies that have implemented biophysical diffusion models in the human spinal cord. These studies demonstrate the advantages of characterizing spinal cord microstructure using advanced multi-compartment diffusion

models, but also the need for more in vivo investigation of the sensitivity and feasibility of these models for the spinal cord specifically.

## 2.4 Challenges in Diffusion Imaging of the Spinal Cord

MRI of the spinal cord is faced with several inherent challenges that have made imaging of the spinal cord difficult, and have limited the translation of advanced diffusion models. First, the spinal cord is small: axially, at the cervical level it is only 1.5 cm in diameter. Second, the spinal cord is susceptible to motion artifacts arising from cardiac cycles, respiratory cycles, and pulsating cerebrospinal fluid, as well as field inhomogeneities from the surrounding bone (which makes shimming difficult). Lastly, relaxation times across gray and white matter are similar, resulting in poor contrast (81).

To address some of these concerns, higher spatial resolution can be attained with a reduced field-of-view (rFOV) sequence (82,83), as demonstrated in Figure 6.

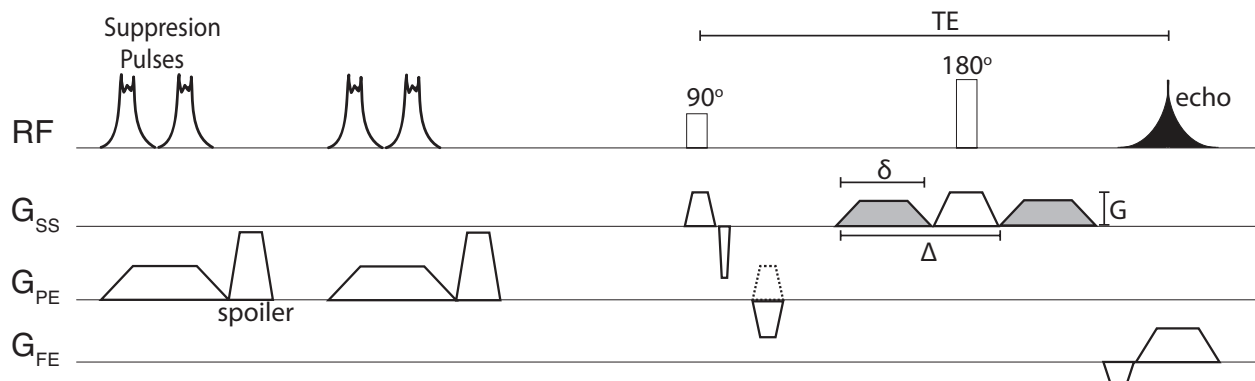


**Figure 6: Outer volume suppression with diffusion sequence.** Reduced FOV imaging is achieved through the use of 2D spatially selective RF excitation pulses, followed by dephasing gradients in the outer volume regions.

By reducing the FOV, the echo train length can be shortened, which can result in decreased sensitivity to susceptibility and motion artifacts. However, in order to avoid aliasing, rFOV techniques must be used to avoid a consequential increase in scan time. Outer volume suppression (OVS) is one rFOV method, and is implemented by placing 2D spatially selective radiofrequency (RF) excitation pulses, followed by dephasing gradients in the outer volume region, before the slice excitation pulse of the imaging sequence (82). OVS pulses are applied in

the phase encode direction on both sides of the outer volume regions of the FOV, and then spoiler gradients completely dephase the transverse magnetization, such that at the time of the excitation pulse, no longitudinal magnetization is present.

Motion artifacts are minimized through the use of single-shot echo planar imaging (EPI), which enables fast acquisition. The effect of the cardiac cycle must also be considered, as caudal displacement of the spinal cord will occur during arterial systole (84). Thus, a pulse oximeter or electrocardiogram is used to trigger the pulse sequence, such that excitation of a slice (for single-shot EPI) or k-space line occurs when the trigger signal is detected. Figure 7 highlights the main parameters required for cardiac triggering. Generally, the trigger signal will be the R-wave, which occurs at the beginning of ventricular systole. To stabilize the acquisition of the signal, a trigger delay, the time interval between the detected R-wave and the start of data acquisition is often defined. For the spinal cord in particular, the trigger delay is usually set around 150-250 ms in order to acquire the data during diastole (85). Lastly, an acquisition window is specified, which determines the time when during the R-R interval the signal is acquired. Drawbacks for cardiac triggering include a prolonged acquisition time, along with variable repetition times (TR).

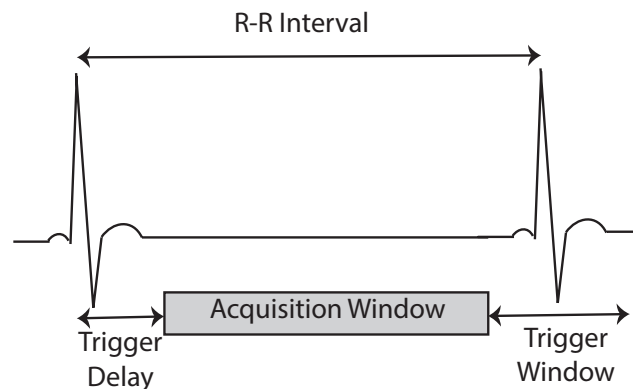


**Figure 7: Cardiac triggering parameters.** The trigger is identified at the R-wave, followed by a delay to stabilize the acquisition. The acquisition window is specified as the time during the R-R interval.

The work in this dissertation uses the OVS rFOV method, along with these other techniques for mitigating the effects of motion, as the foundation of various diffusion sequences to explore the microstructure of the spinal cord. We start with the simplest method, DTI, and work towards biophysical models such as NODDI, SMT and DBSI to assess the sensitivity of these methods in MS.

## CHAPTER 3

### Quantifying the Impact of Underlying Measurement Error on Cervical Spinal Cord Diffusion Tensor Imaging at 3T

#### Text adapted partially from:

By S, Smith AK, Dethrage LM, Lyttle BD, Landman BA, Creasy JL, Pawate S, Smith SA.

Quantifying the impact of underlying measurement error on cervical spinal cord diffusion tensor imaging at 3T. *J Magn Reson Imaging* 2016; 44(6): 1608:1618. doi: 10.1002/jmri.25308

#### 3.1 Introduction

Diffusion tensor imaging (DTI) offers an opportunity to probe tissue microstructure through estimating three eigenvalues from the diffusion tensor, where  $\lambda_1$  is the axial diffusivity (AD), and the mean of  $\lambda_2$  and  $\lambda_3$  is known as the radial diffusivity (RD). Other scalar quantities may be calculated from these eigenvalues such as the fractional anisotropy (FA), a measure of diffusion eccentricity, and the mean diffusivity (MD), the average diffusion in a voxel irrespective of direction (86,87). These quantitative measures have demonstrated promise in characterizing demyelination and axonal damage of white matter in the brain (4,88). There has been increased motivation to expand the application of DTI to study the spinal cord, which is a smaller, and arguably more challenging, tissue, and to evaluate its relationship to the biological and clinical manifestations of diseases. However, clinical implementation of human spinal cord DTI has been hindered by a lack of in vivo characterization of the impact of diffusion weighting choice and scan time.

The spinal cord is a small central nervous system structure that is somatotopically arranged, comprised of segmented tracts that directly communicate with the brain. The two major functions subtended by the spinal cord are motor and sensory function: sensory function is primarily conveyed from the dorsal columns, whereas motor pathways stem from the lateral and ventral columns (89). The integrity of the spinal cord microstructure is vital to neurological function, and damage by neurodegenerative diseases or trauma can have a devastating impact on day-to-day functions such as walking, bowel and bladder function, and sensation. Thus, there is a

need for improved quantitative magnetic resonance imaging (MRI) measurements as they may reveal deeper insight on the subtle pathological changes within the human spinal cord that precede neurological dysfunction.

Specifically for DTI in the human spinal cord in vivo, a detailed set of benchmarks for DTI acquisitions could improve our understanding and interpretation of DTI-derived indices through characterizing the impact of (and interaction of anatomy with) noise, DTI-derived index variation (both spatially and temporally) and diffusion weighting scheme. In the human spinal cord, the feasibility of such studies has been hindered by four considerable challenges which must be overcome to generate high quality data: 1) the small size of the spinal cord (~1.5cm) and its substructures (< 5mm), 2) constant physiological motion, 3) field inhomogeneity near bone/tissue interfaces, and 4) cerebrospinal fluid pulsation (90). Simulation studies have identified that estimation of diffusion tensors is heavily influenced by the noise inherent in a DTI acquisition, and consequently, the signal-to-noise ratio (SNR) and contrast-to-noise ratio (CNR) of the diffusion-weighted image can impact the accuracy and reproducibility of the derived indices (91-93). Similarly, in the brain, in vivo studies corroborate these findings (94-96). However, in the human spinal cord, the sources and distributions of noise vary compared to the brain, and are not well studied in vivo, even though, theoretically, a set of cylindrically oriented tensors may offer some improved insight. As with the brain, one has the choice of increasing the directional resolution of the gradient scheme or increasing the number of averages to increase the SNR for a given scan time (94); however, because of the spinal cord's unique anatomical and physiological differences due to motion, spatial field gradients, largely anisotropic tensors, and cylindrical geometry, selecting more gradients over longer scan time may not provide the expected increase in fidelity of the derived tensors as can be predicted by studies in the brain, or through simulation.

Lee et al. studied DTI acquisition schemes for the cervical cord in the sagittal orientation (97) and focused on FA, however with improved coil and sequence design, higher resolution in the axial orientation can be achieved, which allows a study of both high and low anisotropy tissues (white and gray matter, respectively) (98). A second study suggests no benefit in acquiring more than 15 directions for the estimation of FA (99). With considerable attention being paid to the study of the directional diffusivities for their relationship to axonal and myelin integrity (4,98), a more comprehensive study of all DTI-derived indices, rather than just FA, is



warranted. Moreover, for clinical studies when scan time is limited, we seek to quantify how choice of diffusion gradient scheme influence the accuracy and reproducibility of DTI-derived indices for both gray and white matter in the cervical spinal cord at 3T, a step that has not yet been investigated.

Therefore, the objective of this study is to characterize the source of measurement error in clinically feasible, well-balanced diffusion schemes for the cervical spinal cord.

## 3.2 Methods

### 3.2.1 Data Acquisition

Five healthy volunteers participated in this study (3 male/2 female, ages: 25-36 years). Local institutional review board approval and written informed consent were obtained prior to imaging. Imaging was acquired using a 3.0T whole body MR scanner (Philips Achieva, Best, Netherlands). A quadrature body coil was used for excitation and a 16-channel SENSE neurovascular coil was used for reception. Three DTI datasets were acquired in each scan session, and each volunteer was rescanned within ten days following the initial scan, yielding a total of 30 DTI scans.

Each DTI sequence was acquired with a single-shot echo planar imaging (EPI) using a reduced field-of-view outer volume suppression technique (82) in the axial plane at an effective  $b$ -value of  $750 \text{ s/mm}^2$ . The protocol included a cardiac-triggered spin-echo acquisition with the following relevant parameters: SENSE factor=1.5, flip angle=90°, TR=5 beats (~5000 ms), TE=50 ms, resolution=1x1 mm<sup>2</sup> slice thickness=5mm, number of slices=14, coverage=C2-C5, FOV=64 mm x 48 mm, and diffusion gradient times of  $\Delta=24.4 \text{ ms}$ ,  $\delta=12.8 \text{ ms}$ . Three scan time equivalent (STE) scans were acquired in each session with a minimally weighted image ( $b=0$ ) acquired in each dynamic: 6 non-collinear diffusion-weighted directions acquired 9 times (18:15 min), 15 directions with 4 acquisitions (17:15 min), and 32 directions with 2 acquisitions (17:15 min). The direction schemes were chosen from the default orientation scheme from the scanner, such that directions were sampled uniformly around a sphere. Repeats of a diffusion-weighted scheme for each scan time equivalent acquisition were acquired using multiple dynamics to avoid scanner calibration, re-shimming, and power optimization changes. Consequently, each volume of the dynamic independently contributed to the tensor calculation, and no averaging of

repeated volumes was applied prior. Schemes consisting of 6, 15, and 32 directions were chosen, as these are standard default values on most clinical scanners and are therefore most readily available for clinical implementation. These schemes are highlighted in Table 1. Additionally, a high-resolution ( $0.6 \times 0.6 \times 5 \text{ mm}^3$ ) multi-slice, multi-echo gradient echo (mFFE) (100) anatomical image was acquired ( $TR/TE/\Delta TE = 700/7.2/8.8 \text{ ms}$ ,  $\alpha = 28^\circ$ , number of slices=14, 6:10 min) over the same volume to improve co-registration and to serve as a template for segmentation. The total scan time for one session was 1 hour: 2 minutes: 19 seconds, including the mFFE and other survey planning and calibration scans.

Table 1: Overview of diffusion sequences.

	Directions	Number of Repetitions	Added b0s	Scan Time
Processing Breakdown	6	9		18:15
	Acquired	15	4	17:15
		32	2	17:15
	Full STE	6	9	0
	(~18 min)	15	4	5
		32	2	7
	Half STE	6	5	0
	(~9 min)	15	2	3
		32	1	4
	Shortest	6	3	0
	STE	15	1	3
	(~4.5 min)	32	-	-

### 3.2.2 Data Processing

To provide a benchmark for comparison, all diffusion-weighted (DW) images within each session were combined to compute a so-called gold standard (94). Therefore, for each

acquisition a total of 193 DW acquisitions entered into the tensor calculation. Within each session, the three acquired scan time equivalent scans (6, 15, and 32 gradient directions) were broken down into two additional comparisons. Each protocol included the same number of  $b = 0$  images (Table 1). For each DTI set, each diffusion weighted acquisition was registered to the mFFE (Figure 8a) using the FLIRT package from FSL v5.0.2.1 (FMRIB, Oxford, UK) (101). The  $b=0$  was directly registered to the mFFE, whereas all diffusion-weighted images were registered to the prior diffusion-weighted volume, and this transformation was concatenated with the  $b=0$  and mFFE transformation. Registration was limited to translation (in  $x$  and  $y$ ) and rotation ( $\pm 5$  degrees about the  $z$ -axis) in plane. The rotational component of the correction from the registration procedure was applied to the DTI gradient table (102). As shown in Figure 8b, regions of interest (ROIs) of white matter (WM) and gray matter (GM) were automatically segmented from the co-registered mFFE image using a slice-based groupwise multi-atlas procedure designed specifically for the spinal cord (103). The segmented ROIs were then transferred to the registered/calculated diffusion index maps (FA, MD, AD, RD) for each scan time equivalent scan and gold standard (Figure 8c).

### 3.2.3 Data Analysis

Following registration, the diffusion tensor calculation was estimated using Camino using a nonlinear fit (104). Fractional anisotropy (FA), mean (MD), axial (AD) and radial diffusivity (RD) maps were calculated from the eigenvalues of the diffusion tensor. Contrast-to-noise ratio (CNR) of each map was calculated as:

$$CNR = \frac{\bar{x}_{GM} - \bar{x}_{WM}}{\sqrt{\sigma_{GM}^2 + \sigma_{WM}^2}} \quad (15)$$

where  $\bar{x}_{ROI}$  is the mean value of the ROI and  $\sigma_{ROI}^2$  is the variance of the ROI. A subjective image assessment was performed to qualitatively evaluate the effects of gradient direction scheme on DTI-derived maps.

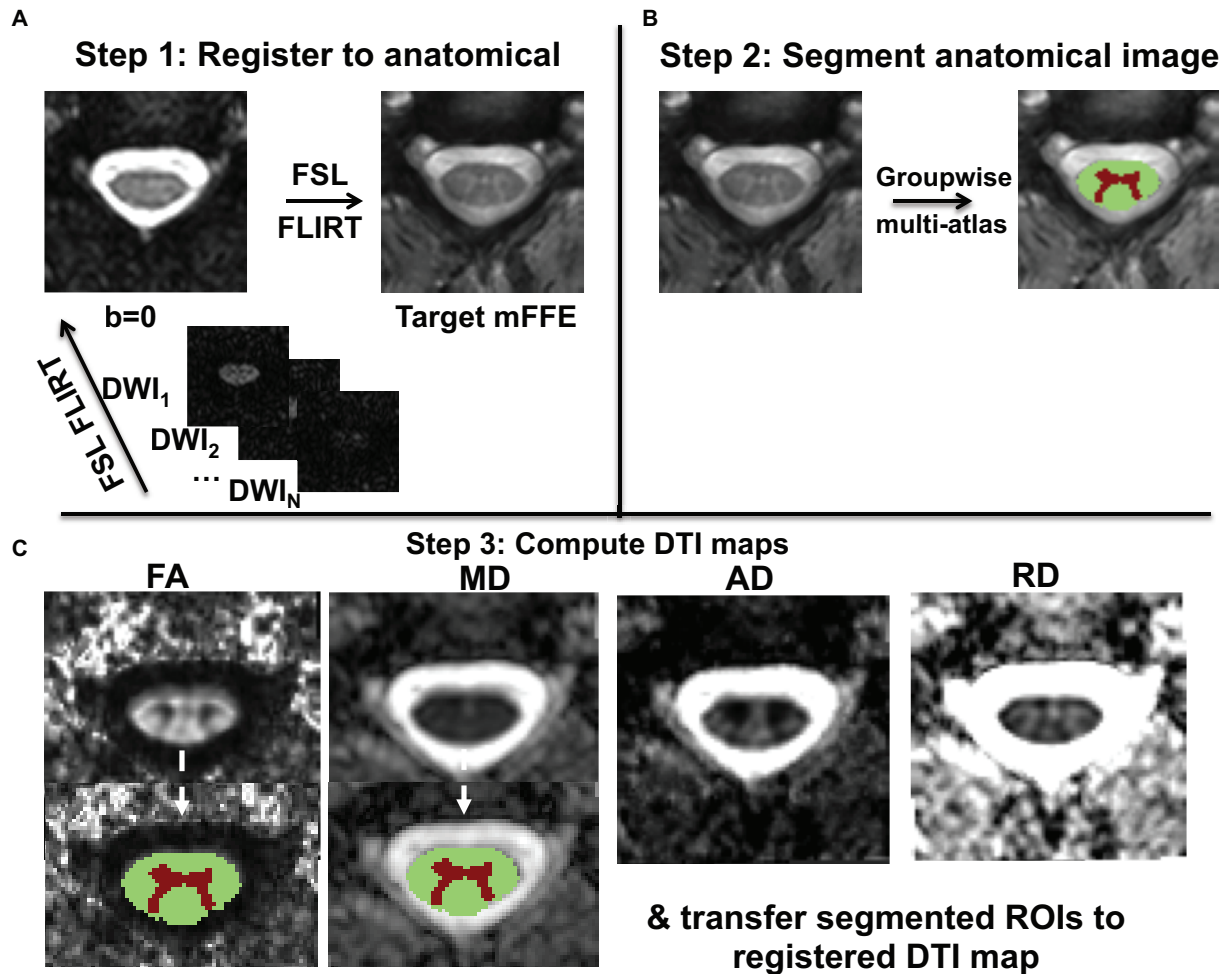


**Figure 8: Flowchart describing image processing scheme.** A) Each scan session acquired an anatomical image, which was used for registration and segmentation of white and gray matter. A 2D affine registration was performed from DTI to mFFE space. These segmented ROIs (B) were then transferred to the registered DTI set (C).

### 3.2.4 Test-Retest Reproducibility

Test-retest reproducibility of each index map from each DW direction scheme was assessed using Bland-Altman (105). With Bland-Altman, each subject from each time point contributes one data point in the analysis per index; the goal is to ascertain whether the 95% confidence interval for the mean difference overlaps zero (no difference at the  $\alpha = 0.05$  level) and to provide an estimate of the variation over time. This was performed for both segmented

white and gray matter. The normalized Bland-Altman difference ( $D_{BA}$ ), 95% confidence interval for the difference, and the limits of agreement were used as reliability metrics.  $D_{BA}$  was defined as:

$$D_{BA} = \frac{D_{12}}{M} * 100\% \quad (16)$$

where  $D_{12}$  is the mean difference of the two sessions and  $M$  is the mean DTI value. Secondly, a non-parametric Wilcoxon signed rank was performed on each mean DTI index in white matter and gray matter at the full scan time equivalent to test whether a difference between the two time points was observed at the  $\alpha = 0.05$  level.

### 3.2.5 Voxel-Wise Analysis

To identify the spatial dependency of the underlying error in DTI measurements, a voxel-wise analysis was also performed. The calculated maps from each control from the first scan were registered to one another using the mFFE anatomical images, and each DTI-derived index map was averaged over all controls, resulting in a single FA, MD, AD, and RD map representing the mean over all five controls. In order to analyze the effect of diffusion scheme for each acquisition against the gold standard to characterize the accuracy of the DTI indices, each DTI index from each sampling scheme was subtracted from the gold standard map. Accuracy was quantified as the bias, or the difference from the gold standard; precision was calculated as the standard deviation of the difference between the chosen scheme's derived maps and the gold standard (94,95). Root mean square error (RMSE) from the gold standard was chosen as the metric for quantifying the overall error, where the RMSE was calculated as the square root of the sum of the accuracy squared and the precision squared. Additional ROIs were manually drawn on the mean mFFE of all controls using MIPAV (Figure 9) to comprehensively assess the spatial dependencies of error in white matter and gray matter: dorsal column (DC), right lateral column (RLC), left lateral column (LLC) and gray matter (GM). The effect size ( $\Omega$ ) of these measurements is reported as the difference in mean RMSE values (78). To assess inter-rater variability, a second rater manually placed ROIs and Bland Altman was used to calculate whether the 95% confidence interval of the difference between the two raters was significantly different from 0. Additionally, the intraclass correlation coefficient (ICC) of rater 1 against rater 2 for each DTI-derived index was computed. The 95% confidence intervals (CI) for the ICC

were calculated using a bootstrap procedure.

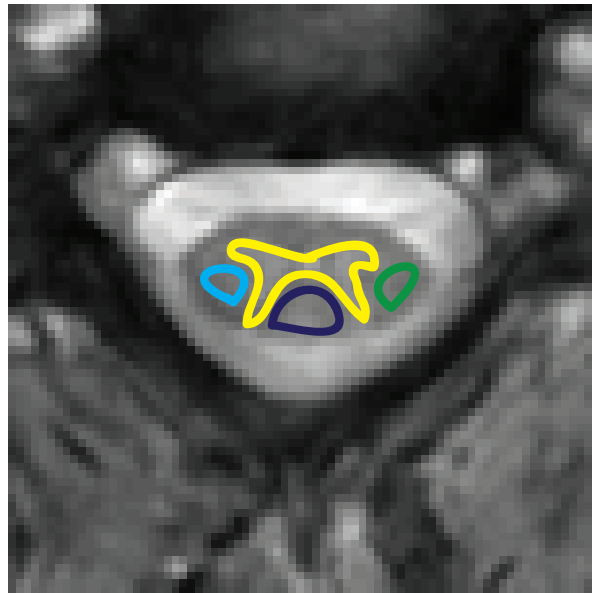


**Figure 9: Additional ROIs overlaid on mFFE for error map processing.** Yellow: gray matter, light blue: right lateral column, green: left lateral column, dark blue: dorsal column.

### *3.2.6 Cross-Sectional Analysis*

The goal of this analysis was to determine whether there was a statistically significant difference in measurement error (i) between gradient weighting schemes (6, 15, and 32), (ii) at different scan time equivalents (4.5, 9, and 18 min) and (iii) between ROIs (DC, RLC, LLC and GM). First, a non-parametric Wilcoxon signed rank test was performed on the mean RMSE for FA, MD, AD, and RD in four different ROIs between the different gradient schemes. This analysis was repeated for each scan time equivalent breakdown (4.5, 9, 18 minutes) to observe the effect of scan time on choice of sampling scheme. Second, a non-parametric Wilcoxon signed rank test was performed on the mean RMSE for the same diffusion scheme at different scan time equivalents to determine whether increased scan time would mitigate measurement error. Third, a non-parametric Wilcoxon signed rank test was performed on the mean RMSE for the same scheme in different tracts. For all comparisons, each subject contributed four RMSE values (across four slices) to the Wilcoxon analysis, and only the first visit (session) was studied.

To reduce the possibility of spurious significances, the significance threshold was chosen to be  $\alpha = 0.01$ .

### 3.3 Results

#### 3.3.1 Gradient Direction Scheme: Effects on DTI-derived maps

Representative DTI maps of a healthy volunteer at the C3/C4 level are displayed in Figure 10, demonstrating the impact of the number of gradient directions at different scan time equivalents. The SNR of the spinal cord of each  $b=0$  image was approximately 13. Qualitatively, the gray/white matter contrast within the spinal cord for FA, AD, and RD can be observed in all schemes, but there is noticeably poorer separation between each tissue type in the 6-direction scheme. This is particularly pronounced on the AD and RD images, where the central gray matter butterfly pattern is difficult to appreciate, specifically in the ventral horns, and there is less contrast between cerebrospinal fluid (CSF) and the spinal cord. However, as expected, the MD is not directionally sensitive and has less dependency on the number of directions (106).

Figure 10 also lists the CNR between the gray and white matter of the spinal cord for each DTI metric. In general, the CNR decreases as scan time decreases with the exception of MD. At the full scan time equivalent, the CNR of the different schemes are comparable. While the contrast between gray and white matter generally increases with more gradient directions, multiple averaging produces lower noise, and therefore, the CNR of the 6-direction scheme for FA and RD is high. As the scan time decreases, the CNR for the 6-direction scheme monotonically decreases, for FA, AD, and RD, while the CNR for the 15-direction and 32-direction schemes remains relatively consistent. At a scan time above 4.5 minutes, however, the effect of a reduced scan time on CNR is minimal for all maps sampled with the 15-direction scheme. The 32-direction scheme is more affected as there is less averaging to account for the variability in image quality.

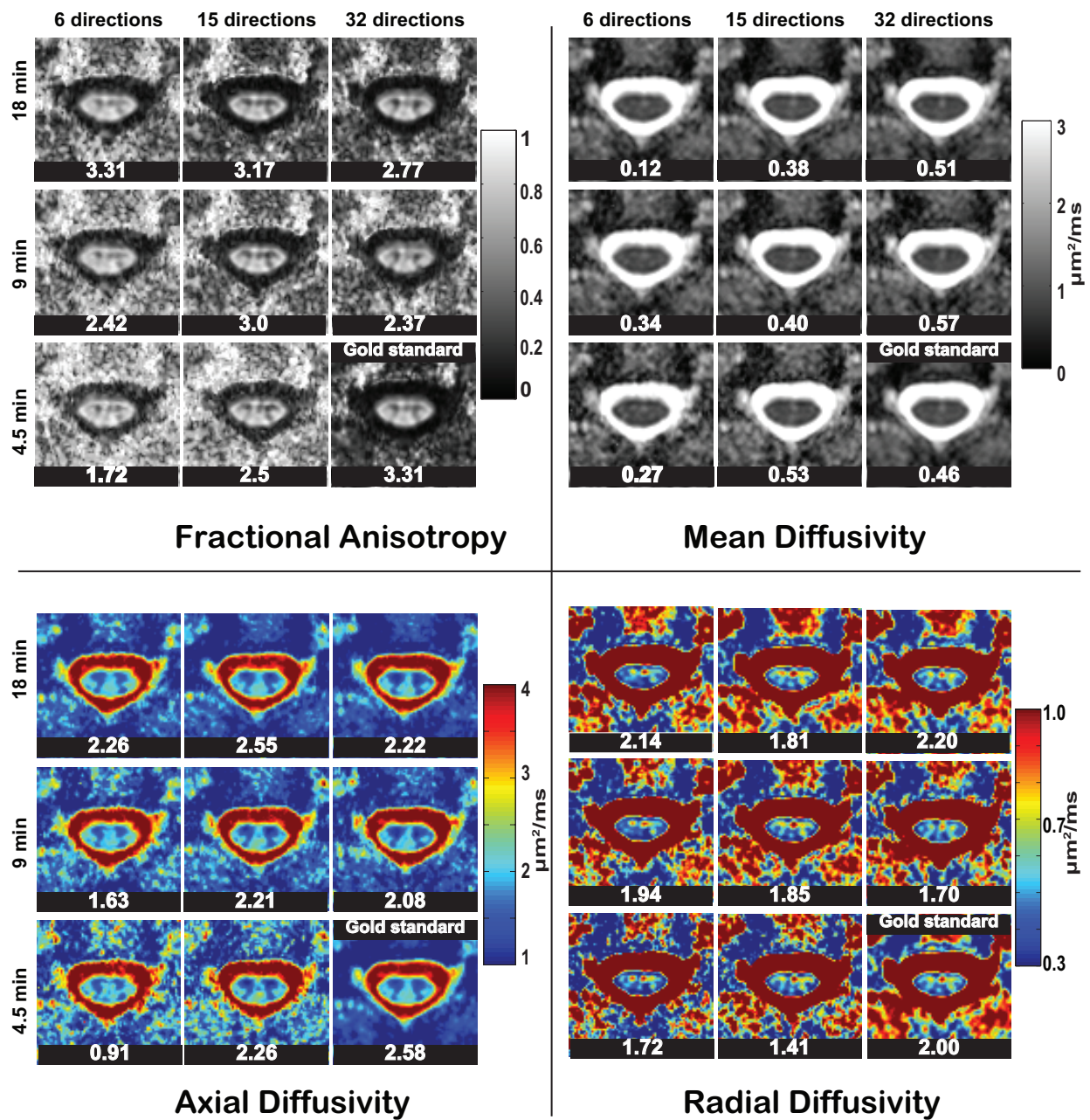


**Figure 10: DTI maps of a representative healthy volunteer acquired from different gradient schemes at different scan time equivalents.** Contrast-to-noise ratio (CNR) of each DTI map is listed below each map. At the full scan time equivalent, the CNR of the different schemes are comparable. However, as scan time decreases, in general, the CNR drops for the 6- and 32-direction scheme, while the 15-direction scheme with 2 averages remains relatively stable.

### 3.3.2 Reproducibility

The reproducibility of each gradient scheme across two time points, choosing the intermediate scan time of 9 minutes, using Bland Altman and Wilcoxon signed rank are



summarized in Table 2. The normalized mean differences of the two visits were small (below 14%) for all indices, with the largest  $D_{BA}$  being produced from the 32-direction scheme. In addition, no significant differences between the two visits were detected with Wilcoxon signed rank for any sampling scheme. The 15-direction scheme resulted in the lowest  $D_{BA}$  for the most comparisons (FA: WM  $D_{BA}$ =0.09%, GM  $D_{BA}$ =2.43%; MD: WM  $D_{BA}$ =2.28%, GM  $D_{BA}$ =0.07%; RD: WM  $D_{BA}$ =3.1%), indicating a smaller variability across different time points with the 15-direction scheme overall.

### 3.3.3 Spatial Dependency of Error

Figure 11 provides a group-wise analysis of the error using data from all five controls at C3/C4. The spatial dependency and artifact contribution of each gradient scheme in the spinal cord can be clearly highlighted in the bias maps (left columns) relative to the mean gold standard. The mean map points out any residual misalignment between multiple subjects. In addition, the RMSE (top) and bias (bottom) plots (right columns) demonstrate the spatial dependency from four different ROIs, with the error bars representing inter-subject variability. In the top panel, the difference in FA ( $\Delta FA$ ) from the gold standard is shown. It is clear that the difference map is most ordered in the 6-direction scheme, with the gray matter visually distinct from the other substructures. The 15-direction scheme and 32-direction scheme produce maps where the cord's general features cannot be easily identified until we reach a low SNR regime of 4.5 minutes. Additionally, it should be noted that there is an upward bias in the mean  $\Delta FA$  with 6-directions (95) as indicated by the uniformly positive  $\Delta FA$  values, but this bias diminishes and accuracy in  $\Delta FA$  estimation is improved with an increase in the number of gradient directions. These trends are also seen in the  $\Delta AD$  maps, but the effects are negligible for  $\Delta MD$ . The  $\Delta RD$  maps indicate that bias is attributed from partial volume effects at the boundaries of the cord and the CSF, rather than from the gray matter structure as seen in  $\Delta FA$  and  $\Delta AD$ .

Inter-rater difference  $\Delta RMSE$  was low:  $D_{BA}$  of 0.67% (FA), 3.08% (MD), 0.07% (AD), and 5.38% (RD). The ICC (95% CI ICC) between rater 1 and rater 2 was 0.94 (0.92, 0.95), 0.87 (0.84, 0.90), 0.95 (0.93, 0.96), and 0.80 (0.74, 0.84) for FA, MD, AD, and RD respectively.

Table 2: Mean ( $\pm$ standard deviation) of DTI-derived parameters over all participants for both scans at the 9-minute breakdown for white matter (WM) and gray matter (GM).

FA	Scan 1	Scan2	Bland Altman				WSR
	<i>mean<math>\pm</math>s.d.</i>	<i>mean<math>\pm</math>s.d.</i>	<i>difference (D)</i>	<i>95% CI</i>	<i>LOA</i>	<i>D<sub>BA</sub>(%)</i>	<i>p</i>
WM 6	0.73 $\pm$ 0.05	0.74 $\pm$ 0.07	-0.008	[-0.04, 0.02]	[-0.15, 0.13]	1.09	0.65
WM 15	0.68 $\pm$ 0.05	0.68 $\pm$ 0.07	-0.001	[-0.03, 0.03]	[-0.12, 0.12]	0.09	0.91
WM 32	0.69 $\pm$ 0.04	0.66 $\pm$ 0.10	0.036	[0.0, 0.07]	[-0.12, 0.19]	5.4	0.05
GM 6	0.61 $\pm$ 0.07	0.62 $\pm$ 0.06	-0.017	[-0.04, 0.01]	[-0.12, 0.09]	2.84	0.2
GM 15	0.55 $\pm$ 0.08	0.54 $\pm$ 0.08	0.013	[-0.01, 0.04]	[-0.10, 0.12]	2.43	0.41
GM 32	0.57 $\pm$ 0.09	0.56 $\pm$ 0.10	0.014	[-0.01, 0.04]	[-0.10, 0.13]	2.53	0.26
<b>MD</b>							
<b>(<math>\mu\text{m}^2/\text{ms}</math>)</b>							
WM 6	1.03 $\pm$ 0.12	1.00 $\pm$ 0.08	0.032	[-0.02, 0.08]	[-0.18, 0.24]	3.15	0.22
WM 15	1.00 $\pm$ 0.07	0.97 $\pm$ 0.06	0.022	[-0.01, 0.05]	[-0.11, 0.15]	2.28	0.28
WM 32	0.96 $\pm$ 0.06	1.02 $\pm$ 0.13	-0.053	[-0.11, 0.01]	[-0.31, 0.20]	5.3	0.11
GM 6	0.99 $\pm$ 0.12	0.99 $\pm$ 0.09	0.004	[-0.03, 0.04]	[-0.16, 0.17]	0.42	0.91
GM 15	0.94 $\pm$ 0.06	0.94 $\pm$ 0.07	0.001	[-0.04, 0.04]	[-0.16, 0.16]	0.07	0.94
GM 32	0.92 $\pm$ 0.07	0.94 $\pm$ 0.11	-0.022	[-0.08, 0.03]	[-0.26, 0.22]	2.34	0.55
<b>AD</b>							
<b>(<math>\mu\text{m}^2/\text{ms}</math>)</b>							
WM 6	2.11 $\pm$ 0.27	2.06 $\pm$ 0.17	0.052	[-0.02, 0.13]	[-0.27, 0.37]	2.48	0.39
WM 15	1.92 $\pm$ 0.13	1.89 $\pm$ 0.13	0.035	[-0.02, 0.09]	[-0.19, 0.26]	1.82	0.23
WM 32	1.89 $\pm$ 0.12	1.91 $\pm$ 0.10	-0.014	[-0.07, 0.04]	[-0.26, 0.23]	0.75	0.65
GM 6	1.79 $\pm$ 0.23	1.79 $\pm$ 0.20	-0.009	[-0.07, 0.05]	[-0.27, 0.25]	0.48	0.55
GM 15	1.62 $\pm$ 0.13	1.59 $\pm$ 0.12	0.029	[-0.05, 0.11]	[-0.30, 0.35]	1.83	0.53
GM 32	1.60 $\pm$ 0.19	1.59 $\pm$ 0.13	0.013	[-0.09, 0.11]	[-0.43, 0.45]	0.8	0.88
<b>RD</b>							
<b>(<math>\mu\text{m}^2/\text{ms}</math>)</b>							
WM 6	0.49 $\pm$ 0.08	0.47 $\pm$ 0.10	0.022	[-0.03, 0.08]	[-0.21, 0.26]	4.63	0.46
WM 15	0.53 $\pm$ 0.08	0.52 $\pm$ 0.10	0.016	[-0.03, 0.06]	[-0.17, 0.20]	3.1	0.41
WM 32	0.50 $\pm$ 0.07	0.57 $\pm$ 0.18	-0.07	[-0.14, 0.00]	[-0.38, 0.24]	13.36	0.09
GM 6	0.59 $\pm$ 0.11	0.58 $\pm$ 0.08	0.01	[-0.03, 0.05]	[-0.15, 0.18]	1.78	0.5
GM 15	0.61 $\pm$ 0.10	0.62 $\pm$ 0.10	-0.016	[-0.05, 0.2]	[-0.16, 0.12]	2.54	0.37
GM 32	0.57 $\pm$ 0.08	0.61 $\pm$ 0.15	-0.039	[-0.09, 0.01]	[-0.24, 0.17]	6.57	0.16

Notably, we find that increased scan time from 4.5 to 18 minutes leads to reduced RMSE (e.g., for 15 directions  $p=0.0004$ ,  $0.0004$ ,  $0.001$ ,  $0.0001$  for DC, RLC, LLC, GM respectively) with moderate effect size for  $\Delta FA$  (e.g., for 15 directions,  $\Omega$  [effect size]= $0.02$ ,  $0.03$ ,  $0.03$ ,  $0.05$  or  $3\%$ ,  $4.4\%$ ,  $4.4\%$ ,  $9\%$  for DC, RLC, LLC, GM).  $\Delta MD$  was generally stable at a scan time greater than 4.5 minutes ( $\Omega < 0.05$ ,  $0.03$ ,  $0.08$  or  $5\%$ ,  $3\%$ ,  $8\%$  for 6, 15, 32 directions) while AD and RD mirrored the effects seen in FA. Bias contributed to approximately half of the total error  $\Delta FA$  and  $\Delta AD$ , approximately 1/4 of the error to  $\Delta RD$ , and nominally to  $\Delta MD$  (Figure 11).

For all indices, however, the reduction in RMSE from 9 minutes to 18 minutes is minimal for the 15-direction scheme (for FA,  $|\Omega| < 3.4\%$  and  $\Omega = -3.7\%$ ; for MD,  $|\Omega| < 3\%$  and  $\Omega = -2.4\%$ ; for AD,  $|\Omega| < 3.7\%$  and  $\Omega = -3.1\%$ ; for RD,  $|\Omega| < 5.9\%$  and  $\Omega = -3.6\%$  for WM and GM respectively), and remains lower than the inter-subject variability. Scan time equivalent (STE) sequences with 15 and 32 directions exhibited small differences in error (e.g., for 9 minutes,  $\Omega < 1\%$  and  $\Omega = 1.8\%$  for WM and GM at a  $p > 0.39$  and  $p = 0.82$  in  $\Delta FA$  with similar relative differences seen in  $\Delta AD$ ,  $\Delta RD$  and  $\Delta MD$ ). However, the 6-direction scheme was substantively different than 15 directions. For  $\Delta FA$  at 9 minutes,  $\Omega < 4.4\%$  and  $\Omega = 5.5\%$  for WM and GM ( $p < 0.01$ ), and the difference in error was seen to increase with increased scan time; at 18 minutes,  $\Omega < 4.4\%$  and  $\Omega = 7.2\%$  WM and GM ( $p < 0.01$ ).

For FA, the error between GM and DC was significantly different ( $p=0.001$ ,  $0.01$ ,  $0.02$  and  $\Omega=0.02$ ,  $0.03$ ,  $0.01$  or  $3.3\%$ ,  $4.9\%$ ,  $1.6\%$  for 6, 15, and 32 directions). It should also be noted that at 9 minutes, the difference in RMSE between the RLC and LLC is lowest for all DTI metrics with the 15-directions (e.g. for  $\Delta FA$ ,  $\Omega=0.08$ ,  $0.007$ ,  $0.03$  or  $11.8\%$ ,  $1.0\%$  or  $4.4\%$  for 6, 15, and 32 directions); no difference is detected between the two columns (e.g. for  $\Delta FA$ ,  $p=0.94$ ,  $0.37$ ,  $0.23$  for 6, 15, and 32 directions).

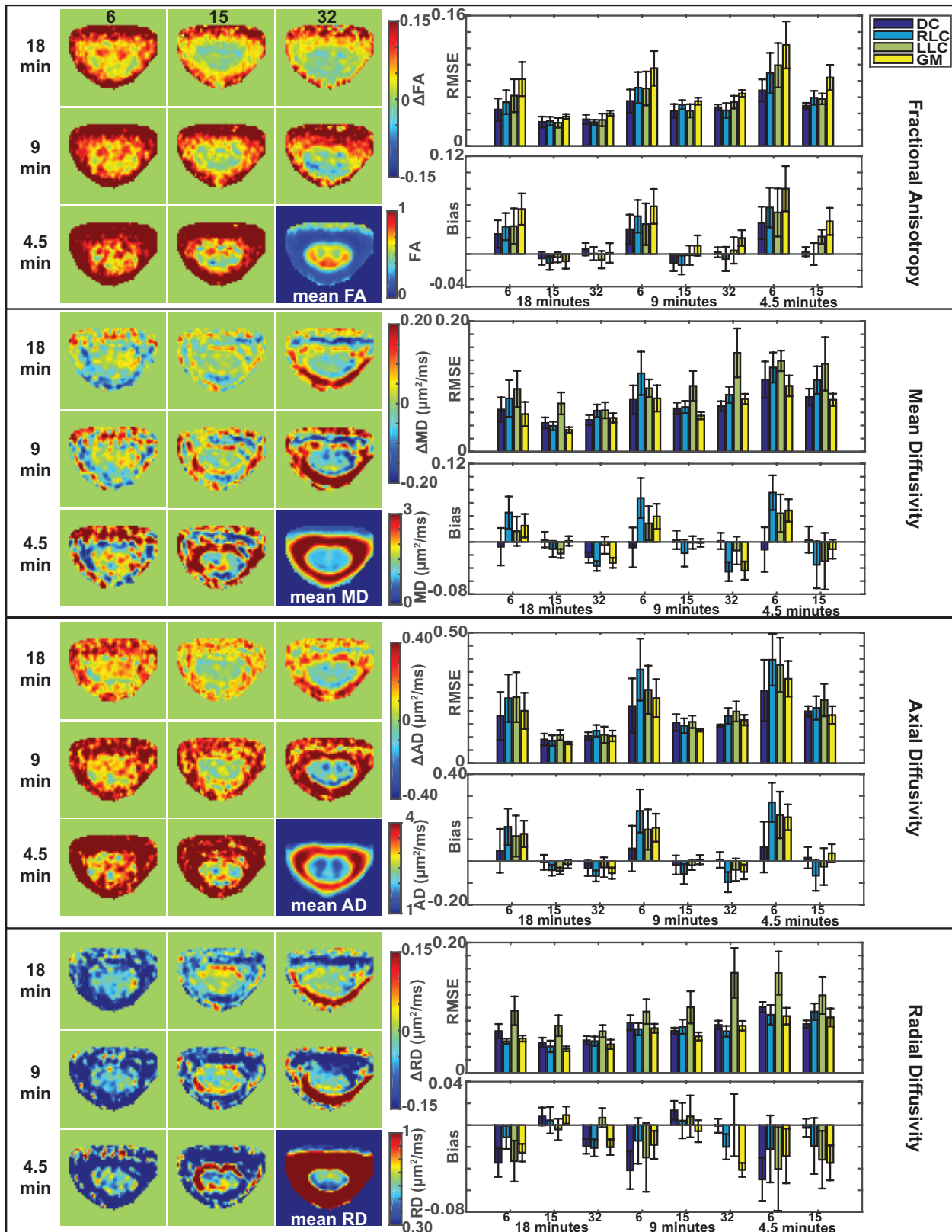


**Figure 11: Error bias maps, calculated as the difference from the gold standard, using all control data for gradient schemes of 6, 15 and 32 directions at 4.5, 9, and 18 minutes.** Increased scan time leads to reduced RMSE.  $\Delta$ MD was relatively stable, while the effect size for  $\Delta$ FA,  $\Delta$ AD and  $\Delta$ RD was moderate. Scan time equivalent sequences of 15 and 32 exhibited small differences in error, but the 6-direction scheme was significantly different from the 15-direction scheme.

### 3.4 Discussion

In this work, we investigated the accuracy and precision of FA, MD, AD, and RD in scan time equivalent acquisitions for the cervical spinal cord. The goal was to provide an estimate of the benefits and consequences when designing pulse sequences to be deployed in the clinic for evaluation of various disease states, highlighting the magnitude of error for the most commonly used gradient schemes. From our findings, we observe that at a clinically relevant scan time of 9 minutes, a 15-direction gradient scheme produces the lowest error in diffusion measurements of all gradient schemes tested and provides DTI maps with high and reproducible contrast. Furthermore, we find that there is no benefit in using scan times over 9 minutes with the 15-direction scheme, as the reduction in RMSE from 9 to 18 minutes is lower than the inter-subject variability and any benefits in doubling scan time are negligible. Therefore, we conclude that a 15-direction gradient scheme of 9 minutes can accurately quantify tissue microstructure of the cervical spinal cord at 3T.

Recent studies of the spinal cord indicate the large disagreement in the applied number of directions (107-110). When establishing a DTI protocol for clinical implementation, it is critical to consider the number of gradient directions of the DTI scheme in terms of the overall goal of the study. Consistent with other studies, we observed that a scan time equivalent gradient scheme of 6-directions is significantly worse than a gradient scheme of 15- or 32- directions in estimation for  $\Delta$ FA (99), but we further reveal that these trends are also observed for  $\Delta$ AD and  $\Delta$ RD. Therefore, when referencing the literature and performing future studies, comparisons of protocols using different gradient schemes should be cautiously analyzed. Simulations of the brain have identified a scheme of 20 directions is optimal for robust anisotropy estimation, and at least 30 are required for estimation of mean diffusivity (111). Our choice to compare 6-, 15- and 32-direction schemes enabled us to test whether these findings could be easily translatable to the cervical spinal cord on most clinical MRI scanners. Furthermore, we investigated the error in gradient schemes at three different scan time equivalents. The 18-minute scan time equivalent demonstrates the most extreme case we are capable of performing, providing differences in gradient schemes at a high SNR regime while minimizing variability (94). While increased scan time led to reduced RMSE, the trends observed at the full scan time equivalent were mirrored at the other scan time equivalents, albeit with reduced effect. We use this finding to guide the user

to implement the maximum available scan time equivalent when possible to minimize spurious conclusions.

In terms of contrast, a balance between acquisition time and gradient scheme was observed. With 32-directions, the CNR was lowest for FA and RD. This can be attributed to the fact that in the 32-direction gradient scheme there is an increased sampling along the longitudinal (and primary diffusion) axis, yielding increased diffusion and an attenuation of signal resulting in increased noise. The CNR for the 6-direction schemes should not be overanalyzed, as the known upward bias in FA in lower SNR regimes may incorrectly detect contrast (95). Furthermore, it was observed that multiple averages minimize variability caused by image corruption due to patient movement and inherent inconsistencies in hardware of the MR system. It should also be noted that choice of  $b$ -value will influence CNR, and in this study, we chose a  $b$ -value of  $750 \text{ s/mm}^2$  to provide high gray and white matter contrast while maintaining sufficient SNR, as suggested by Summers et al. (84).

Assessment of reproducibility of DTI measurements is vital when evaluating the clinical utility of DTI in the spinal cord. In order to perform longitudinal or multisite studies, the variation of the measurement error of different tracts must be known in order to determine whether observed differences are normal or abnormal. We found that the mean difference between two scans was small, but the 32-direction scheme produced the largest  $D_{BA}$  values due to the increased variability when no averaging was applied for this scheme at the 9-minute scan time equivalent. Cardiac triggering was applied in this study to reduce signal intensity variations (84), and may have strengthened the reproducibility of these measurements.

Given these combined results, we conclude that in clinical studies where the goal is a general characterization of quantitative indices in each spinal cord tissue type, a 15-direction scheme is sufficient for reliable tensor estimation and the time saved from sampling fewer gradient directions can be leveraged for greater SNR and sensitivity. In general, for clinically relevant applications (acquisition time  $< 10$  min), we recommend the use of a 15-direction gradient scheme with two averages (9 minutes) for accurate estimation of FA, AD, and RD. When investigating the intricacies of the spinal cord microstructure in greater detail, however, a higher sampling rate (32 directions over 15) may be beneficial to resolve boundaries of the spinal cord, as fewer directions may lead to greater variability in the principal eigenvector (PEV) orientation, which is an important consideration for tractography. This may be important for

tissues that are damaged or when following the longitudinal evolution of diseases. For example, when it is desired to observe features such as crossing fibers, schemes with higher angular resolution such as HARDI and DBSI have been implemented, as an increase in the number of gradient directions is necessary to distinguish partial volume effects (76,112,113).

While others have reported optimization of DTI protocols in the spinal cord (97,99), this study provides two main distinctions. First, this study provides a comprehensive analysis using all DTI-derived indices in the spinal cord, where it is not transparent which direction scheme is optimal for minimizing variance in the derived indices while maximizing contrast. This type of experiment provides important findings, as acquisition time can be used more effectively to provide higher sensitivity, resolution, or SNR rather than to acquire unnecessary gradient directions (redundant data) for relatively oriented tensors such as in the spinal cord. Furthermore, the consideration of diffusivities other than FA is integral to comprehensively assessing pathological processes. Oh et al. (5) observed RD to be the most distinguishable index in their study of MS patients versus healthy controls, but current studies on optimization of DTI in the spinal cord have only considered the effect of acquisition parameters on FA. We demonstrated that accurate estimation of RD is directionally sensitive, and therefore, findings from this study can offer new opportunities for comprehensively studying the role of the spinal cord in diseased states. Second, this type of study not only provides an optimal protocol for spinal cord DTI, but additionally, it quantifies the impact of the sacrifices (i.e. lower number of gradient directions or fewer excitations) that must be made for clinical implementation of spinal cord DTI on DTI-derived indices. Given the RMSE and bias of each gradient scheme, the results of this study can also be used to build the foundation to perform power tests to calculate sample sizes for future diffusion studies. In addition, this study implements more recent findings of DTI that have not been thoroughly investigated for protocol optimization such as imaging the spinal cord axially (98), the use of cardiac triggering (84), reduced field-of-view imaging (82,83,114), and voxel-wise analysis of individual tracts (115). The voxel-wise analysis of multiple tracts highlights where the measurement is specifically failing, and the spatial dependencies of error. It should be noted that the ventral column could not be reliably determined due to partial volume effects.

This study had several limitations. First, we did not perform any fiber tractography. While an increase in angular resolution may be necessary for improved tractography of the cord, since the spinal cord primarily runs in the rostral-caudal direction, we have chosen to focus on

the scalar indices under the assumption that tractography may be able to be performed with probabilistic methods, or even fewer directions than in the brain (116). This study could also be improved by using a larger sample size of healthy controls and including abnormal patients. Patients with neurological disorders may have movement impairments, which may additionally affect the spatial dependency of error in our DTI-derived measurements. However, it is noted that larger studies in patient populations would provide improved insight into the direct clinical impact that these optimization strategies may have. Technological advancements, such as simultaneous multi-slice (SMS) imaging, may help expedite diffusion scans and further minimize errors (117). Finally, it should be noted that the reduced field-of-view excitation scheme chosen for this work is currently not product on all clinical scanners, however it can easily be implemented using 2D excitation, outer volume suppression methods or saturation bands, which are currently available features on most clinical scanners without further software modification.

Looking forward, though these guidelines were optimized for the cervical spine, they can easily be adapted for the thoracic and lumbar spine or any anatomy where their fibers align along a single, largely coherent direction (peripheral nervous system, optic nerve). When considering smaller structures, the SNR is significantly reduced due to a need for higher resolution. In the condition where the SNR is not as high as it is in the cervical cord, the directional dependencies and need for more averages may play a role in choosing the best sequence to obtain quality indices. Moreover, it may be advantageous to develop an optimized gradient direction scheme, rather than using the basic schemes available on the scanner, for more precise and accurate tensor estimation (118).

In conclusion, the results of this study provide the underlying error and variation of different gradient schemes on estimation of FA, MD, AD, and RD. Taken together, the observed results demonstrate the efficiency of the 15-direction scheme in minimizing error when characterizing the spinal cord's tracts overall.



## CHAPTER 4

### Neurite Orientation Dispersion and Density Imaging: Application to MS

#### Text adapted partially from:

By S, Xu J, Box BA, Bagnato FR, Smith SA. Application and evaluation of NODDI in the cervical spinal cord of multiple sclerosis patients. *NeuroImage: Clinical* 2017. doi: 10.1016/j.nicl.2017.05.010.

#### 4.1 Introduction

Though diffusion tensor imaging (DTI) has demonstrated promise in assessing tissue microstructure, several pathological factors, such as the presence of inflammation, tissue loss, crossing fibers and cerebrospinal fluid (CSF) contamination, can confound the interpretation of these findings. Multi-compartmental and multi-tensor biophysical models have been developed to address this concern. The first multi-compartmental model that this work will investigate is called neurite orientation dispersion and density imaging (NODDI). NODDI may provide a more specific analysis of diffusion. In particular, the changes in microstructure can be assessed in terms of neurite density and orientation dispersion, elucidating the contributions to DTI-derived fractional anisotropy (FA) and therefore ameliorating the issue of DTI-derived parameters being non-specific. Characterizing axonal fractions of the spinal cord could potentially be useful in disease tracking of multiple sclerosis (MS).

NODDI has been demonstrated in brain tumors (119), neurofibromatosis (120), focal cortical dysplasia (121) and the brain in multiple sclerosis (122). To date, most applications using NODDI focus on the brain, but recently, the feasibility of performing NODDI in the healthy human spinal cord in vivo was reported (75). There are, however, no studies evaluating NODDI in the spinal cord with pathology such as MS. Therefore, our main objectives were (i) to study the reproducibility of NODDI in the spinal cord of healthy controls and (ii) to study the feasibility and sensitivity of NODDI in patients with MS. We hypothesize that NODDI may provide the unique ability to offer sensitive and more model-specific information about the pathological changes known to occur in the spinal cord of MS patients, potentially improving

upon DKI and conventional DTI.

#### 4.1.1 Model Theory

NODDI is a multi-compartmental model that distinguishes intracellular, extracellular and CSF compartments. The normalized signal  $A$  is written as:

$$A = (1 - v_{iso})(v_{in}A_{in} + (1 - v_{in})A_{ec}) + v_{iso}A_{iso} \quad (17)$$

$A_{in}$ ,  $A_{ec}$ ,  $A_{iso}$ , are the normalized signal of the intracellular, extracellular and CSF compartments respectively;  $v_{in}$  and  $v_{iso}$  are the volume fractions of the intracellular and CSF compartments, respectively. Note that in describing white matter, the intracellular and extracellular compartments may also be referred to as intra-axonal and extra-axonal respectively. Each of these compartments has different signal models.

The intracellular component is the space containing neurites (dendrites and axons). Due to the highly restricted nature of diffusion in this space, the intracellular component is modeled as sticks, or cylinders with zero radius. The normalized signal is given as:

$$A_{ic} = \int_{S^2} f(n)e^{-b\lambda_{\parallel}(q \cdot n)^2} dn \quad (18)$$

where  $q$  is the gradient direction and  $b$  is the  $b$ -value;  $f(n)dn$  is the volume fraction of sticks along the orientation  $n$ ;  $e^{-b\lambda_{\parallel}(q \cdot n)^2}$  is the signal attenuation due to unhindered diffusion along a stick with diffusivity  $\lambda_{\parallel}$  and orientation  $n$ . The orientation distribution function is modeled as a Watson distribution, a cylindrically and antipodally symmetric distribution over a unit sphere, representing nonparallel axons dispersing about some central orientation (123,124):

$$f(n) = M\left(\frac{1}{2}, \frac{3}{2}, \kappa\right)^{-1} e^{\kappa(\mu \cdot n)^2} \quad (19)$$

where  $M$  is a confluent hypergeometric function and  $\kappa$  represents the extent of orientation dispersion around  $\mu$ , the mean orientation for the distribution. When  $\kappa$  is positive, the distribution

is bipolar with a maximum at  $\pm\mu$ . Larger  $\kappa$  corresponds to lower dispersion about  $\mu$ .

The extracellular component is the space around the neurites, occupied by glial cells and neuronal cell bodies. Diffusion is hindered, and is modeled as a Gaussian anisotropic distribution. The diffusivities of the extracellular compartment are coupled via the orientation dispersion of the intracellular space, with the normalized signal expressed as:

$$\log(A_{ec}) = -bq^T \left( \int_{\mathbb{S}^2} f(n) D_{ec}(n) dn \right) q \quad (20)$$

$D_{ec}(n)$  is a cylindrically symmetric tensor with an axial diffusivity  $\lambda_{\parallel}$  that is parallel to  $n$  and equal to the free diffusivity of the intracellular compartment. Its radial diffusivity is perpendicular to  $n$  and described by the tortuosity model (125):

$$\lambda_{\perp} = \lambda_{\parallel}(1 - v_{in}) \quad (21)$$

Using the Watson model,  $D_{ec}$  from Equation 20 can be analytically written as:

$$D_{ec} = (\lambda'_{\parallel} - \lambda'_{\perp}) \vec{\mu} \vec{\mu}^T + \lambda'_{\perp} I \quad (22)$$

where  $I$  is the identity matrix and

$$\lambda'_{\parallel} = \lambda_{\parallel} - \lambda_{\parallel} v_{in} \left( 1 - \left( -\frac{1}{2\kappa} + \frac{1}{2F(\sqrt{\kappa})\sqrt{\kappa}} \right) \right) \quad (23)$$

$$\lambda'_{\perp} = \lambda_{\parallel} - \lambda_{\parallel} v_{in} \frac{1 + \left( -\frac{1}{2\kappa} + \frac{1}{2F(\sqrt{\kappa})\sqrt{\kappa}} \right)}{2} \quad (24)$$

where  $F(\sqrt{\kappa}) = \frac{1}{2} \sqrt{\pi} e^{-\sqrt{\kappa}^2} \operatorname{erfi}(\sqrt{\kappa})$ .

CSF is modeled as isotropic Gaussian diffusion, with diffusivity  $d_{iso}$ . Given the isotropic volume fraction, a relationship solving for the intracellular restricted volume fraction  $v_r$  has been adapted (75):

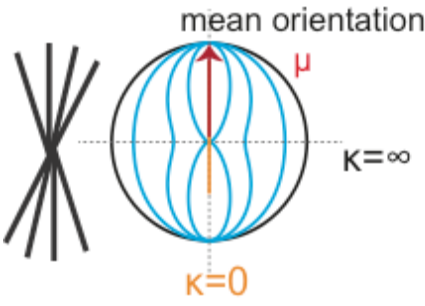


$$v_r = (1 - v_{iso}) * v_{ic} \quad (25)$$

In addition to the intracellular volume fraction, intracellular restricted volume fraction and isotropic volume fraction, the orientation dispersion index can be computed:

$$ODI = \frac{2}{\pi} \arctan (1/\kappa) \quad (26)$$

The NODDI model is summarized in Table 3.

Table 3: Summary of NODDI model.

Compartment	Model	DOF	Assumptions	Resulting DOF
Intracellular	<p>Sticks</p> 	$v_{in}$ $d_{  }$  $f(n, \mu, \kappa)$ , $\mu(\theta, \psi)$	$d_{  } = 1.7 \mu\text{m}^2/\text{ms}$	$v_{in}$  $\kappa, \theta, \psi$
Extracellular	<p>Hindered, Anisotropic Tensor</p> 	$v_{ex}$  $d_{\perp}, d_{  }$	$v_{ex} = (1 - v_{in})$  $d_{\perp} = (1 - v_{in}) * d_{  }$	
Other (CSF)	<p>Isotropic Restricted</p> 	$d_{iso}, v_{iso}$	$d_{iso} = 3 \mu\text{m}^2/\text{ms}$	$v_{iso}$

## 4.2 Methods

### 4.2.1 MRI Experiments

Eight healthy controls (mean age  $\pm$  standard deviation = 29.0 $\pm$ 5.0 years, 5 male/3 female) participated in this study, four of whom had a rescan within a month to assess reproducibility. Six relapsing-remitting MS (RRMS) patients (6 female, 39.3 $\pm$ 6.1 years) were recruited for this study. Patients' disability was rated using the Expanded Disability Status Scale (EDSS) score (22) in the Vanderbilt University Multiple Sclerosis Clinic (patient EDSS range=0-6). Table 4 lists specific clinical demographics of the patients. Local institutional review board approval and written informed consent were obtained prior to imaging.

Table 4: Clinical and demographic characteristics of patients.

Patient	Age (years)	Sex	MS Type	MS Duration (years)	EDSS	Lesion (in diffusion volume)*
MS 1	46	F	RRMS	17	2	Y (LLC)
MS 2	36	F	RRMS	8	2.5	Y (LLC, DC)
MS 3	45	F	RRMS	4	3.5	Y (RLC, LLC, DC)
MS 4	34	F	RRMS	10	6	Y (diffuse)
MS 5	32	F	RRMS	1	0	Y (LLC)
MS 6	43	F	RRMS	2	1	Y (RLC, LLC)

Y=yes, N=no, RLC=right lateral column, LLC=left lateral column, DC=dorsal column

All experiments were performed on a 3.0T whole body MR scanner (Philips Achieva, Best, Netherlands). A quadrature body coil was used for excitation and a 16-channel SENSE neurovascular coil was used for reception. The maximum gradient strength of the system was 80 mT/m at a slew rate of 100 mT/m/s.

For each subject, a high-resolution (0.65x0.65x5 mm<sup>3</sup>) multi-slice, multi-echo gradient

echo (mFFE) anatomical image (100) was acquired (TR/TE/ $\Delta$ TE = 753/7.1/8.8 ms,  $\alpha = 28^\circ$ , number of slices=14, 6:12 min) for co-registration and to serve as a reference image for segmentation.

The diffusion sequence consisted of a cardiac-triggered, spin echo sequence with single-shot echo planar imaging (EPI) readout with the following parameters: TR/TE=3 beats ( $\sim 3000$  ms)/65 ms, resolution=1.25 x 1.25 mm<sup>2</sup>, slice thickness=10 mm, slices=1, FOV=68 x 52 mm, SENSE (AP)=1.5 and NSA=3. Reduced field-of-view was applied using an outer volume suppression technique (82) and fat suppression was achieved using Spectral Presaturation with Inversion Recovery (SPIR). A multi-shell acquisition, similar to the previously published NODDI protocol in the brain (10) and the one implemented in the spinal cord (75) was used with uniform sampling: (i)  $b=711$  s/mm<sup>2</sup> with 32 directions and (ii)  $b=2855$  s/mm<sup>2</sup> with 64 directions, with constant gradient times of  $\Delta$  (separation between gradients)=31.8 ms and  $\delta$  (gradient duration)=21.0 ms. A non-diffusion-weighted scan ( $b=0$  s/mm<sup>2</sup> or  $b_0$ ) was acquired with each shell. Total scan time was 18:11 min. All images were centered at the C3/C4 level, except for one MS patient that was centered at the C4/C5 level where more lesions were detected. Images were acquired in the axial plane for both the anatomical and diffusion images.

#### *4.2.2 Image Analysis and Processing*

All diffusion-weighted volumes were co-registered to the anatomical (mFFE). First, the  $b_0$  images from each shell was diffeomorphically registered to the anatomical using ANTS (126). All other diffusion-weighted volumes were then registered to its  $b_0$  image using an affine transformation to correct for eddy current distortions (127). Finally, regions of interest (ROIs) of white matter (WM) and gray matter (GM) were automatically segmented from the co-registered anatomical image using a slice-based groupwise multi-atlas procedure designed specifically for the spinal cord (103). The ROIs were eroded by a disk-shaped structuring element with a radius of four voxels in the white matter and one voxel in the gray matter to avoid inaccurate voxels at the boundaries, potentially arising from misregistration or partial volume effects. For patients, the same groupwise multi-atlas segmentation procedure was performed for white and gray matter. Additionally, we refined the segmentation by manually delineating lesions on the anatomical image, and then normal appearing white matter (NAWM) was any of the segmented white matter not containing manually drawn lesion voxels. It is possible that some gray matter

voxels either contain gray matter lesions themselves, or are partial volumed with white matter lesions. For the latter, this is somewhat unavoidable due to the reliance on automatic gray matter segmentation, which cannot differentiate lesions from gray matter (similar contrast) when they are in close proximity to one another; for the former, we expect that gray matter is damaged in some participants and thus the gray matter values we report are a combination of both normal appearing gray matter and gray matter with lesions. Examples of ROI identification for a representative control (WM, GM) and two MS patients (lesion, NAWM) are shown in Figure 12. Note that all images are displayed on the radiological coordinate system.

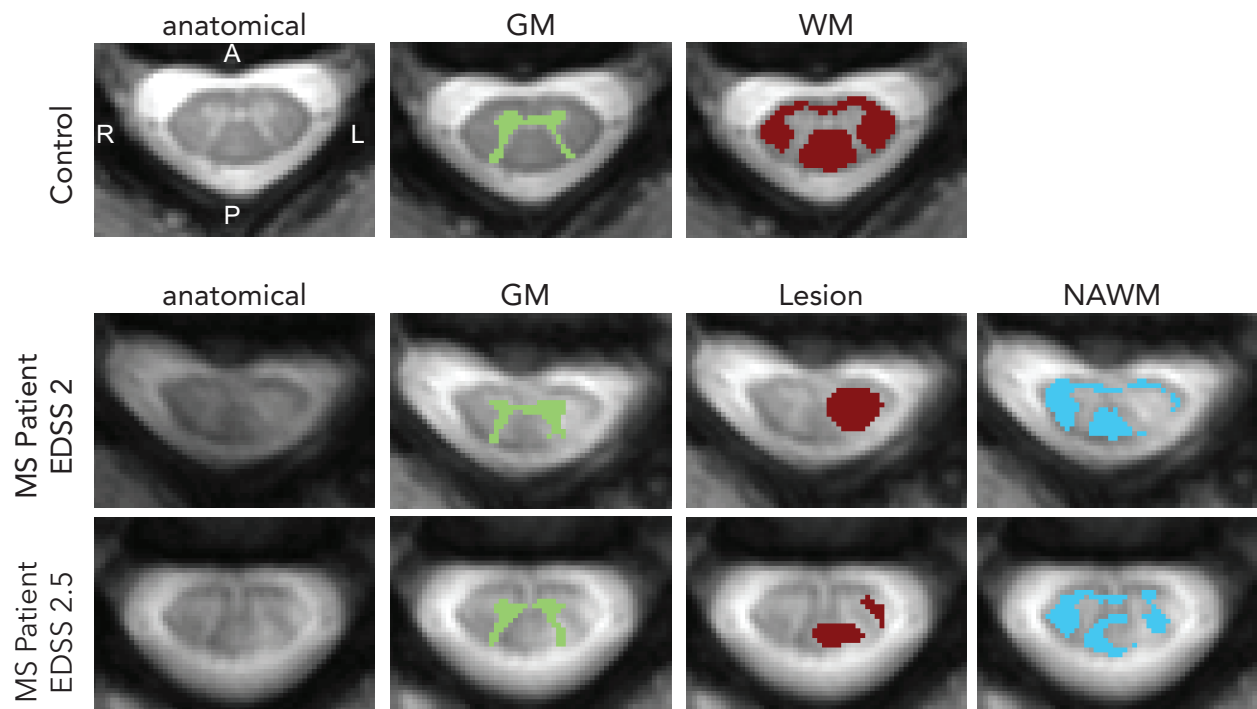


**Figure 12: Examples of ROI identification.** Representative control (top row) includes the anatomical (left) from which the GM (second column) and WM (third column) were automatically segmented. For MS patients (middle and bottom row), the GM (second column) and WM are automatically segmented the same way as controls. WM, however, is separated into manually delineated lesions (third column) and any WM voxels containing no lesion was considered NAWM (fourth column). Note for all images the radiological coordinate system is used.

NODDI fitting was performed using the NODDI MATLAB Toolbox ([http://nitrc.org/projects/noddi\\_tolbox](http://nitrc.org/projects/noddi_tolbox), version: 0.9). Diffusion coefficients for the intra-axonal

and isotropic compartments were fixed with values of  $d_{\parallel}=1.7 \mu\text{m}^2/\text{ms}$  and  $d_{\text{iso}}=3.0 \mu\text{m}^2/\text{ms}$  respectively as in (10) and (75). From this fitting, the derived NODDI indices included: the apparent intra-axonal volume fraction  $v_{\text{in}}$ , representing the fraction of dendrites and axons; the isotropic volume fraction  $v_{\text{iso}}$ , representing the fraction of free water such as CSF; and the orientation dispersion  $ODI$ , a measure of how nonparallel axons disperse about a central orientation by assuming a cylindrically symmetric Watson distribution (10).

#### 4.2.3 Repeatability

The reproducibility of the NODDI-derived indices were assessed using Bland-Altman (105) for white matter. In the Bland Altman analysis, each subject's mean index within the automatically segmented ROI (white matter) entered reproducibility analysis as a single data point. The 95% confidence interval (CI) for the mean difference was calculated and if the 95% CI overlaps zero, the indication is that there is no significant difference between scan 1 and scan 2 at  $\alpha=0.05$ . The normalized Bland Altman ( $D_{BA}$ ) was also used as an estimate of reliability to be used for comparison across derived indices, calculated as:

$$D_{BA} = \frac{D_{12}}{M} * 100\% \quad (27)$$

where  $D_{12}$  is the mean difference between the two sessions and  $M$  is the mean diffusion-derived index of interest. A nonparametric Wilcoxon signed rank was performed, in addition to the Bland Altman analysis, to determine whether a significant difference exists between the mean of each diffusion-derived index for each of the two scans at  $\alpha=0.05$ .

Histograms of the NODDI-fitted parameters were created over all of the healthy control white matter voxels in the scan and rescan to visualize whether any deviations from one another were noticeable. For  $v_{\text{in}}$ , a bin width of 2% over a range of 25 to 95% was used; for  $v_{\text{iso}}$  a bin width of 2% with a range of 0 to 80% was used; for  $ODI$ , a bin width of 0.008 with a range of 0 to 0.15 was used.

#### 4.2.4 Group Comparison

A cross-sectional analysis was conducted to determine white matter differences in NODDI-derived indices between the healthy and MS cohorts. A nonparametric Wilcoxon rank



sum test was performed on the mean  $v_{in}$ ,  $v_{iso}$ , and ODI values in healthy white matter (within healthy controls), NAWM, and lesions for patients at a significant threshold of  $\alpha=0.05$ . The same comparison was performed for DKI and DTI. Statistical differences between healthy gray matter (within healthy controls) and normal appearing gray matter (MS patients) were also assessed using a nonparametric Wilcoxon rank sum test.

#### 4.2.5 Analysis of Maps

Image quality in the NODDI-derived maps was assessed by the image contrast between white matter and gray matter in healthy controls. Contrast was defined as:

$$C = \frac{|\mu_{WM} - \mu_{GM}|}{\frac{1}{2}(\mu_{WM} + \mu_{GM})} \quad (28)$$

where  $\mu_x$  represents the mean over the specified region of interest.

### 4.3 Results

#### 4.3.1 Feasibility and Reproducibility of NODDI in Controls

Figure 13 shows the NODDI-derived maps co-registered and averaged over all healthy controls, along with the averaged anatomical image (mFFE). The  $v_{in}$  maps show high contrast between gray and white matter, with lower  $v_{in}$  values in the gray matter compared to white matter, as expected. The averaged image's (from Figure 13) contrast between white matter and gray matter is 0.23; the image contrast from the maps of individual controls is smaller (mean over all controls  $\pm$  standard deviation =  $0.13 \pm 0.07$ ). The  $v_{iso}$  map highlights the central sulcus and central canal, along with some gray and white matter contrast (averaged image's contrast: 0.53, mean contrast over all controls =  $0.42 \pm 0.36$ ). Lastly, the ODI maps provide the most significant contrast between gray and white matter (averaged image's contrast: 1.19, mean contrast over all controls =  $1.08 \pm 0.19$ ), which is expected since the orientations of gray matter dendrites are much more non-uniformly distributed compared to close-to-uniformly oriented axons in the white matter tracts. It is important to point out that the high value voxels at the rim of the spinal cord in both the  $v_{in}$  and ODI maps are presumably due to registration errors, and are

exaggerated when taking the average over all healthy control subjects. For  $v_{iso}$ , high  $v_{iso}$  levels at the boundary of the spinal cord and cerebrospinal fluid (CSF) can be attributed to higher partial volume effects, in addition to the registration errors.

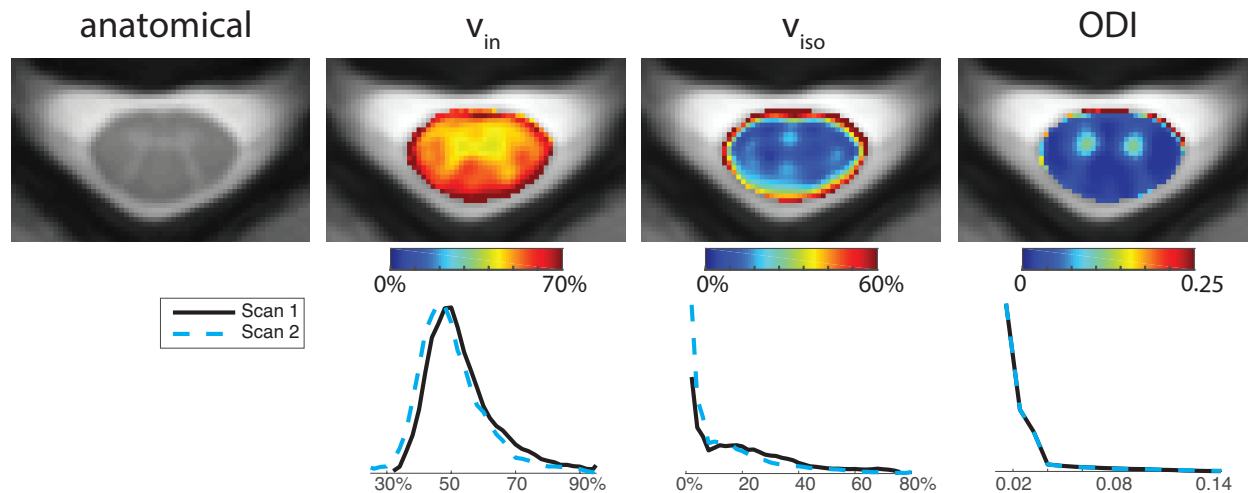


**Figure 13: Maps and histograms of fitted parameters using NODDI in controls.** *Top row:* Mean maps over all of the controls were calculated for the anatomical (left),  $v_{in}$ ,  $v_{iso}$ , and ODI (right). *Bottom row:* Histograms over all white matter voxels for scan 1 and scan 2 for  $v_{in}$ ,  $v_{iso}$ , and ODI (right).

To highlight any outliers and demonstrate the overlap between scan and rescan, the bottom row of Figure 13 includes the histograms over all white matter voxels for all of the controls in scan 1 and scan 2. For  $v_{in}$ , both histograms overlap one another significantly. For  $v_{iso}$ , although both of the histograms largely overlap, there is a higher frequency of voxels with low  $v_{iso}$  (<10%) in scan 2 than scan 1. For ODI, the histograms overlay onto each other directly, indicating high reproducibility. Reproducibility histograms for individual controls (data not shown) demonstrated the same trends as the group histograms (Figure 13), and were consistent across subjects, yielding mean percent differences between scan and rescan over all controls of 8.22%, 45.5% and 5.09% for  $v_{in}$ ,  $v_{iso}$ , and ODI respectively. Table 5 lists the reproducibility metrics for each NODDI-derived index. It is important to note that the 95% confidence intervals for the mean difference of all of the derived indices overlap 0 and the Wilcoxon sign rank p-value is greater than 0.05, indicating that the metrics are not significantly different from one another in the two different time points. Both  $v_{in}$  and ODI yield  $D_{BA}$  under 10%, however  $v_{iso}$

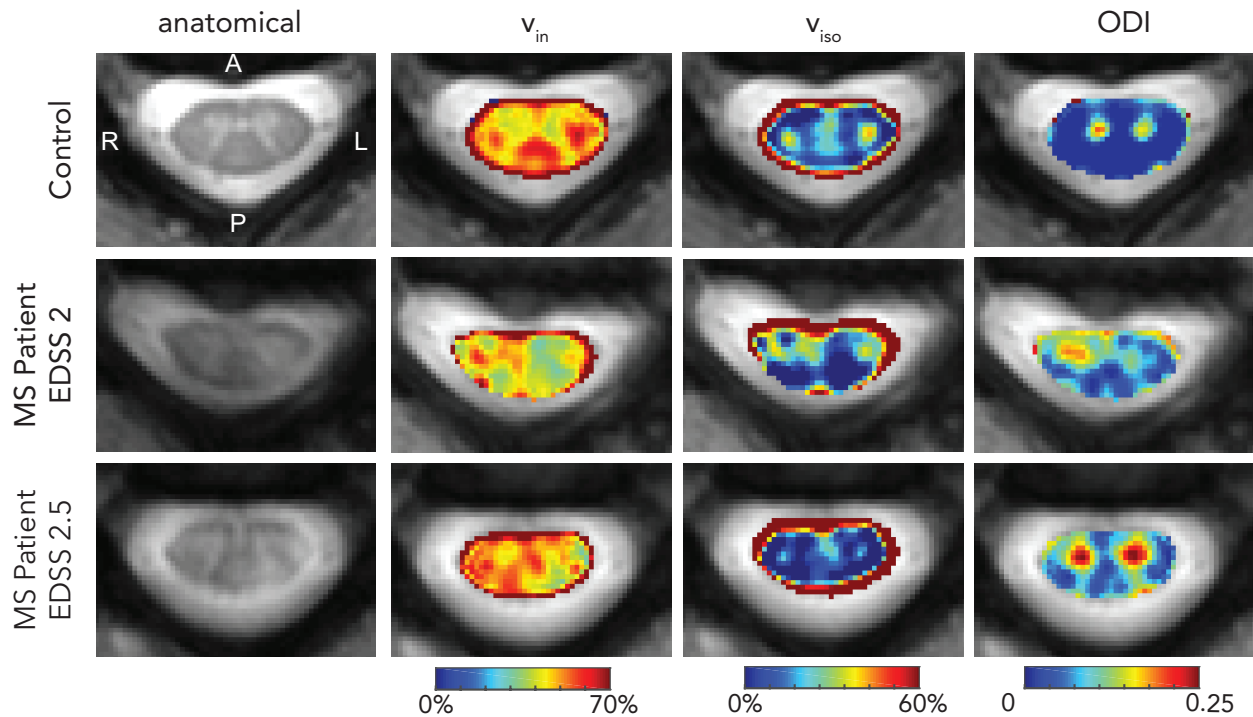
yields a high  $D_{BA}$  of 35.5%, indicating that the variability between the two scans is large for  $v_{iso}$ .

Table 5: Reproducibility metrics for NODDI.

<b>NODDI</b>	<b>Scan 1</b>	<b>Scan 2</b>	<b>Bland-Altman</b>		<b>WSR</b>
	<i>mean±s.d.</i>	<i>mean±s.d.</i>	<i>Difference</i>	<i>95% CI</i>	<i><math>D_{BA}</math> (%)</i>
$v_{in}$	54.3±3.53%	50.4±8.19%	3.88	[-4.52, 12.3]	7.47
$v_{iso}$	21.8±4.84%	15.2±8.30%	6.59	[-3.07, 16.2]	35.5
$ODI$	0.021±0.007	0.021±0.003	-0.0005	[-0.013,0.012]	2.27

#### 4.3.2 Application in MS Cohort

Figure 14 shows examples of the anatomical and NODDI-derived maps in a healthy volunteer and two MS patients (patient 1: EDSS=2, duration of disease=17 years, patient 2: EDSS=2.5, duration of disease=8 years). For patient 1, a lesion in the left lateral column (as shown in Figure 12) can be observed in the anatomical and corresponds to areas of decreased intra-axonal fractions in the  $v_{in}$  maps. Additionally, this patient shows decreased  $v_{in}$  in areas where the anatomical looks otherwise normal, such as the right dorsal column. In patient 2, smaller lesions are seen in the left dorsal and left lateral column on the anatomical (as shown in Figure 12), and similarly, a decreased  $v_{in}$  is observed. No similar trends in the  $v_{iso}$  maps can be extracted from these examples. Lastly, the  $ODI$  maps in both MS participants demonstrate changes not localized at the site of the lesion, but rather, diffuse increases throughout the cord's white matter and in MS patient 2, a large increase in the gray matter signal. This indicates that  $ODI$  may have the ability to probe the subtle microstructural changes in NAWM before they can be detected by conventional MRI such as the mFFE.



**Figure 14: Example images from NODDI.** Representative control is shown in the first row, followed by examples from two different MS patients (same as Figure 12). From left to right, the anatomical,  $v_{in}$ ,  $v_{iso}$ , and ODI are shown.

In Figure 15, boxplots summarize the observed trends for  $v_{in}$ ,  $v_{iso}$ , and ODI over healthy white matter for controls (white) and, in the MS patients, lesions (identified from the anatomical) and NAWM in light and dark gray boxes respectively. The median (red line) and interquartile range (whiskers) over each cohort is displayed, along with the mean value for each individual as it enters the boxplot. Note, only five points are plotted for the NAWM in the MS cohort, as one MS patient had a diffuse lesion over the entire cord at the C3/C4 level. For  $v_{in}$  (Figure 15a), lesions show a significant decrease ( $p=0.001$ ) compared to healthy control white matter. There is no detectable difference between NAWM and control white matter ( $p=0.171$ ) or between NAWM and lesions ( $p=0.247$ ), but a trend is observed where NAWM values fall between lesions and control white matter tissue. No significant differences were observed in  $v_{iso}$  across cohorts in either tissue type (Figure 15b). Importantly, Figure 15c shows a global increase in ODI in lesions ( $p<0.001$ ) and NAWM ( $p=0.002$ ) compared to healthy volunteer white matter. When comparing gray matter of healthy controls to MS patients (data not shown), a significant decrease in  $v_{in}$  was

observed ( $p=0.04$ ) along with a significant increase in ODI ( $p=0.003$ ), but no change was observed in  $v_{iso}$  ( $p=0.22$ ).

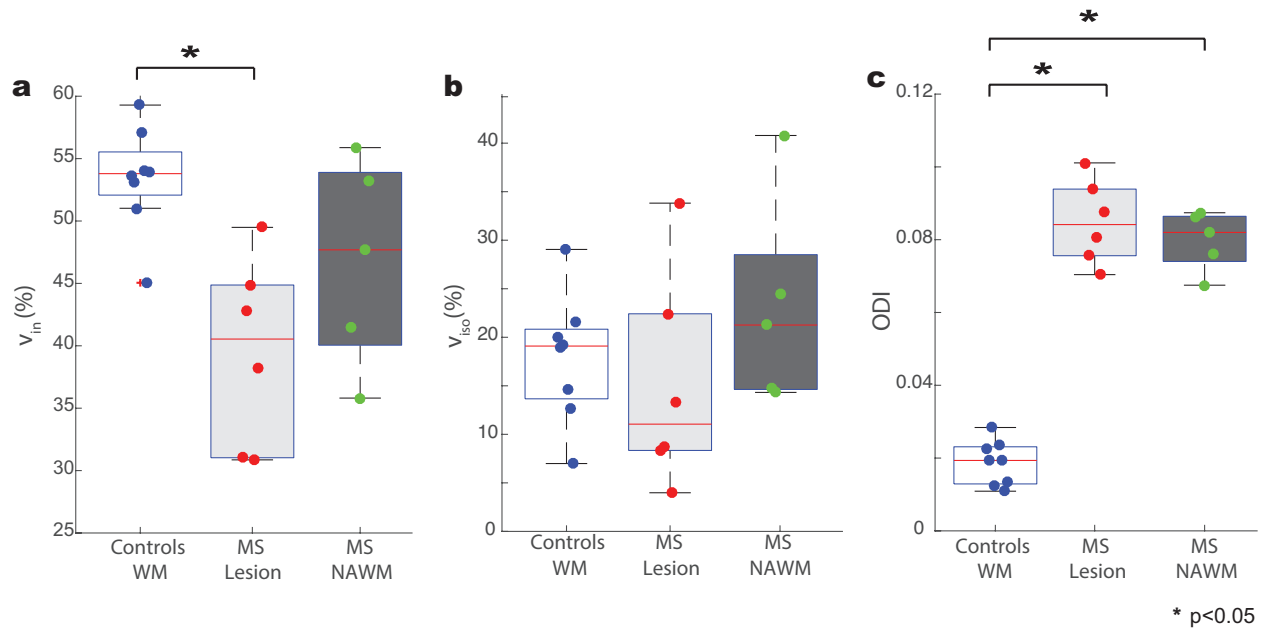


**Figure 15: Comparison of  $v_{in}$ ,  $v_{iso}$ , and ODI.** Boxplots highlighting the median, 25<sup>th</sup> and 75<sup>th</sup> percentiles over controls (WM) and MS patients (lesions and NAWM) for (a)  $v_{in}$ , (b)  $v_{iso}$  and (c) ODI. Mean values from each subject plotted and asterisks indicate significant differences between the groups.

#### 4.4 Discussion

This work demonstrates (i) the feasibility of deriving high-quality NODDI indices in the spinal cord of healthy controls and patients with MS and (ii) the sensitivity of NODDI in detecting pathological changes in the spinal cord of MS. Specifically, we show that  $v_{in}$  and ODI provide high intra-cord contrast in patients with MS, which allows for unique characterization of damage that the spinal cord undergoes along the evolution of MS. With NODDI, the ability to separate different compartments provides a clearer understanding of the derived indices. For example, it has been demonstrated that a decrease in FA could be due to a decrease in  $v_{in}$  or increase in ODI (10,75). Parameters such as  $v_{in}$  and ODI, however, offer assessment of specific

pathological changes with minimized confounding influence (i.e. from CSF), which may be advantageous in longitudinal tracking of the disease more accurately.

Recently, the first application and feasibility of NODDI in the cervical spinal cord was reported with healthy volunteers only (75). In this current study, we observed that our NODDI-derived indices fall within the range of those observed by Grussu et al., who report a  $v_{in}$  of  $57\pm 9\%$  (our study:  $54\pm 4\%$ ),  $v_{iso}$  of  $12\pm 11\%$  ( $18\pm 7\%$ ), and ODI of  $0.027\pm 0.003$  ( $0.018\pm 0.006$ ). Additionally, our reproducibility measurements are in good agreement to those previously reported, where  $v_{in}$  and ODI show reliable measurements but the reproducibility of  $v_{iso}$  is poor. As a result,  $v_{iso}$  did not provide a reliable contrast when applied to the MS cohort, and would be more difficult to follow in longitudinal studies. However, we observed a statistically significant decrease in  $v_{in}$  in lesions, a finding that is consistent with the expected pathology in chronic MS lesions with known axonal injury and loss. This also corresponds well with findings from an ex vivo spinal cord of MS study (74), where decreased  $v_{in}$  was observed in lesions in comparison to the NAWM and correlated well with histological metrics. Interestingly, in some patients in our study, a decreased  $v_{in}$  was also observed in surrounding NAWM, which may indicate the potential of the index to detect microstructural changes of white matter without obvious inflammation, which is not detectable using conventional MRI. An increased ODI throughout the white matter was observed, suggesting pervasive changes in the spinal cord in the presence of MS. These findings also align well with the ex vivo study, where ODI was higher in NAWM than in lesions (74), and may indicate that ODI has the potential to be used as a prognostic indicator even before new lesions appear. Finally, significant differences in gray matter of healthy controls and normal appearing gray matter in MS patients were observed for  $v_{in}$  and ODI, which may be indicative of pathological changes known to occur in gray matter lesions, such as axonal transection, in addition to neuronal, glial and synaptic loss (128). One limitation of this study, however, is that fixed diffusivities of  $d_{||}=1.7 \mu\text{m}^2/\text{ms}$  and  $d_{iso}=3.0 \mu\text{m}^2/\text{ms}$  for the intra-axonal and isotropic compartments respectively, as implemented in the NODDI toolbox (10) and in the previous study of NODDI in the healthy spinal cord (75). While the DTI-derived indices from this study indicated that these estimates were reasonable and similar to literature values (5) for the spinal cord in both healthy and MS cohorts, future studies should investigate the effect of fixing the diffusivities to known values for a specific cohort.

There has recently been an increased interest of applying advanced diffusion models in

the human cervical spinal cord in vivo (50,75,78,79) and to our knowledge, no multi-compartmental diffusion models have been used to measure specific microstructural information of spinal cord of patients with MS. A main technical concern that has hampered this application is the difficulty in registering diffusion-weighted volumes well. With the high b-values ( $b > 1000$  s/mm<sup>2</sup>) needed in many of these protocols, the signal is often too low for registration. Previous studies have interleaved non-diffusion-weighted volumes throughout the acquisition, and relied on applying the transformation of the nearest interleaved volume to the diffusion-weighted volumes (75,129). This method, however, assumes that negligible motion has occurred in between non-diffusion-weighted volumes, which is impractical in the presence of patient movement such as swallowing. With sufficient signal-to-noise ratio (SNR), we were able to achieve reliable affine registration of the individual diffusion-weighted volumes, which also enabled eddy current correction (130).

Only one slice of the cervical spinal cord was acquired in the current study, because the main goal was to investigate the feasibility and sensitivity of NODDI in MS patients, and therefore, rather than optimizing for acquisition time, we chose to implement a sequence that minimized any dependencies of SNR and focused only on one level of the cord. In future studies, simultaneous multi-slice excitation imaging will help improve slice coverage without the expense of additional acquisition time (131). Optimal direction schemes may also be investigated for the spinal cord specifically to allow for additional decreases in acquisition time.

Future studies involving a larger cohort and investigating the correlation of the NODDI-derived parameters with clinical disability are warranted. While no effect on age was observed on the NODDI-derived metrics in this study, Taso et al. have previously reported an association with age and decreased DTI-derived metrics (132); however, their results indicate that an effect on age is only significant when comparing groups younger than 50 to groups older than 50 years old, which was not the case for this current study. However, future studies involving age-matched controls are worthwhile. Lastly, a longitudinal study utilizing multi-parametric MRI may help gain confidence of the NODDI-derived indices, in addition to further disentangling the pathological processes occurring in MS (113).

In conclusion, we demonstrated the feasibility and initial results of NODDI in the cervical spinal cord of MS patients. NODDI maps provide distinguishable contrast, which may reflect underlying microstructural changes known to occur in MS.

## CHAPTER 5

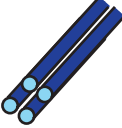
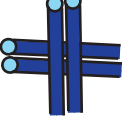


### Spherical Mean Technique: Application to MS

#### 5.1 Introduction

While promising, NODDI makes two primary assumptions that may hinder application to various diseases (133). First, NODDI assumes fixed intrinsic diffusivities, which is known to vary across white matter tissues. Secondly, the NODDI model underestimates the complicated white matter fiber orientations, as the orientation dispersion is modeled by a single, cylindrically symmetric Watson distribution. These approximations, while helpful for rapid application in vivo, may limit the accuracy of the NODDI-derived metrics, especially in pathology. Recently, the spherical mean technique (SMT) has been proposed to model the microscopic diffusion process (68,69), enabling the ability to map the neurite density and compartment diffusivities. SMT takes the spherical mean of the diffusion signals over various gradient directions for a given b-value, and provides orientation invariant indices, such as the apparent axonal volume fraction  $v_{ax}$  and axonal diffusivity  $D_{ax}$ . Figure 16 demonstrates the confounding effects of orientation dispersion when estimating FA with DTI and how orientation invariant indices can resolve these issues. With an orientationally organized anisotropic structure (left), the microdomain FA ( $\mu$ FA) and DTI-derived FA are equal to 1. As the tissue geometry's orientational order decreases, the FA decreases, however the  $\mu$ FA is unaffected. In an isotropic situation, both  $\mu$ FA and FA are equal to 0.

Additionally, by estimating the axonal diffusivity, SMT does not assume fast exchange in the extra-axonal space (i.e. a uniform diffusion coefficient) as it does in NODDI. Thus, the SMT model may provide an alternative, straightforward and potentially reliable method to characterize neural tissue without the confounding influence from complicated axon fiber orientation distribution. This may be useful in studying MS, as the fiber orientation dispersion may increase as a result of demyelination and axonal loss. By removing the effect of fiber orientation distribution and modeling the true axonal diffusivity, SMT may provide a more sensitive measure of axonal volume fraction than NODDI.



Tissue Geometry				
$\mu\text{FA}$	1	1	1	0
FA	1	0.7	0	0

**Figure 16: Varying tissue geometries and effect on  $\mu\text{FA}$  and FA.** When the orientational order decreases, the FA decreases, however the  $\mu\text{FA}$  remains constant.

### 5.1.2 Model Theory

Details on the SMT model and derivations can be found in (68,69). Briefly, the diffusion signal  $h_b$  is independent of its location within a voxel (since it is not spatially encoded this way in our MRI acquisition) and can be, therefore, the microscopic diffusion signal can be written as a function of the spherical distance  $\langle g, \omega \rangle$  between two normalized gradient directions  $g$ :

$$h_b(g, \omega) = h_b(\langle g, \omega \rangle) \quad (29)$$

where  $\omega$  is the rotation axis or orientation of the microscopic axonal segment and is defined on a two-dimensional unit sphere,  $\omega \in S^2$ . The spherical distance  $\langle g, \omega \rangle$  falls between  $[-1, 1]$ . Furthermore,  $h_b$  is antipodally symmetric, such that  $h_b(g, \omega) = h_b(-g, \omega)$ . The observed MRI signal can therefore be written as:

$$\frac{E_b(g)}{E_0} = \int_{S^2} h_b(g, \omega) \rho(\omega) d\omega \quad (30)$$

where  $E_b(g)$  is the diffusion-weighted signal,  $E_0$  is the non-diffusion-weighted signal and  $\rho(\omega)$  describes the frequency of the microscopic fiber population.

Without knowing the distribution of the axons, the spherical mean of the diffusion signal over all gradient directions  $e_b$  can be expressed as:

$$e_b = \frac{1}{4\pi} \int_{S^2} e_b(g) dg \quad (31)$$

Conversely, the microscopic fiber diffusion signal  $h_b$  can be written as:

$$h_b = \frac{1}{4\pi} \int_{S^2} h_b(g, \omega) dg \quad (32)$$

Using Fubini's theorem and shifting the order of integration, the mean signal is independent of orientation distribution and is only a function of diffusion signal of the microscopic diffusion signal:

$$e_b = \int_{S^2} \left( \frac{1}{4\pi} \int_{S^2} h_b(g, \omega) dg \right) \rho(\omega) d\omega = h_b \int_{S^2} \rho(\omega) d\omega \quad (33)$$

While fixing the b-value, the spherical mean of the diffusion signal over all gradient directions  $e_b$  in the spherical coordinate system yields:

$$e_b = \int_0^{\pi/2} h_b * \cos\theta * \sin\theta \quad (34)$$



where  $\theta$  is the angle between the gradient direction and microdomain orientation.

The diffusion signal is represented using a two-compartment model, separated into an intra- and extra-axonal compartment. The apparent intra-axonal compartment represents dendrites and axons, and is modeled as sticks with a transverse diffusivity set to zero. The extra-axonal compartment comprises of the glial cells and neurons in the extracellular space and is modeled as an anisotropic tensor. The transverse extra-axonal diffusivity coefficient  $D_{\perp,ex}$  is described using a tortuosity approximation (125) where  $D_{\perp,ex} = (1 - v_{ax})D_{ax}$ . The mean diffusion signal using SMT is therefore represented as:

$$S = v_{ax}S_{ax} + (1 - v_{ax})S_{ex} \quad (35)$$

where  $S_{ax} = \frac{\sqrt{\pi} \operatorname{erf}(\sqrt{bD_{ax}})}{2\sqrt{bD_{ax}}}$  and  $S_{ex} = \exp(-bD_{\perp,ex}) \frac{\sqrt{\pi} \operatorname{erf}(\sqrt{b(D_{ax}-D_{\perp,ex})})}{2\sqrt{b(D_{ax}-D_{\perp,ex})}}$ . Furthermore, the intra- and extra- axonal diffusion signals are the spherical means over all gradient directions in each b-value shell. Table 6 below summarizes the SMT model.

Table 6: Summary of SMT model.

Compartment	Model	DOF	Assumptions	Resulting DOF
Intra-axonal	Sticks 	$V_{ic}$  $d_{  }$		$V_{ic}$  $d_{  }$
Extra-axonal	Hindered, Anisotropic Tensor 	$V_{ex}$  $d_{\perp}, d_{  }$	$v_{ex}=(1-v_{ic})$  $d_{\perp}=(1-v_{ic})*d_{  }$	

To date, there are only a few studies that have implemented multi-compartment diffusion imaging in spinal cord (75,79), but none have implemented the SMT technique in either healthy subjects or patients with MS. The goals of this study were (i) to evaluate the feasibility and reproducibility of SMT in the human spinal cord in vivo and (ii) to determine the sensitivity of SMT in a cohort of MS patients.

## 5.2 Methods

### 5.2.1 Human Subjects

Local institutional review board approval and written informed consent were obtained prior to imaging. The same controls and patients in the NODDI study (Chapter 4, Table 4) were enrolled. Eight healthy controls (29.0±5.0 years, 5M/3F) participated in this study; to assess reproducibility, four healthy controls were rescanned within a month. Six relapsing-remitting MS patients (39.3±6.1 years, 6F) were recruited for this study. Patients' disability was rated using the Expanded Disability Status Scale (EDSS) score (22), and ranged from 0 to 6 for the patients enrolled in this study. Although some of the patients were known to have spinal cord disease from previous clinical scans, none of them was experiencing an acute exacerbation. All patients had been free from steroid administration for at least 6 months.

### 5.2.2 In Vivo Imaging

Scans were performed on a 3.0T whole body MR scanner (Philips Achieva, Best, Netherlands), using a dual channel body coil for excitation and a 16-channel SENSE neurovascular coil for reception. Again, the same exact dataset used for the NODDI study was used for this study, but for reference, the main parameters will be summarized here. All imaging was centered at the C3/C4 level, except for one MS patient centered at C4/C5 where more lesions were known to be present. In each scan session, an anatomical image was acquired consisting of a high-resolution, multi-echo gradient echo (mFFE) (100) with the following relevant parameters: resolution=0.65x0.65x5 mm<sup>3</sup>, TR/TE/ΔTE=753/7.1/8.8 ms, α=28°, number of slices=14 and acquisition time=6:12 min. The spin-echo diffusion sequence was cardiac triggered and utilized a single-shot echo planar imaging (EPI) readout. Reduced field-of-view was implemented using an outer volume suppression technique (82). One slice was acquired with the following parameters: TR/TE=3 beats (~3000 ms)/65 ms, resolution=1.25 x 1.25 mm<sup>2</sup>, slice thickness=10 mm, FOV=68 x 52 mm, SENSE (AP)=1.5, fat suppression was performed using Spectral Presaturation with Inversion Recovery (SPIR), NSA=3. Two b-shells were acquired, including a b=711 s/mm<sup>2</sup> shell uniformly sampling 32 non-coplanar directions and a b=2855 s/mm<sup>2</sup> shell sampling 64 non-coplanar directions. A total of two non-diffusion-weighted scans (b=0 s/mm<sup>2</sup> or b<sub>0</sub>) were acquired, one at the beginning of each b-value shell acquisition. Total

acquisition time was 18:11 min.

### *5.2.3 Image Pre-Processing*

In each scan, the anatomical image (mFFE) was used as a reference template for registration and segmentation. Registration was performed using ANTS (126). The two  $b_0$  images from the diffusion-weighted scan were diffeomorphically registered to the anatomical, and all other diffusion-weighted volumes were subsequently registered to the closest  $b_0$  image using an affine transformation to correct for eddy current distortions (127).

A groupwise multi-atlas method was used to automatically segment the anatomical image into regions of interest (ROIs) of white matter and gray matter (103). To avoid inaccurate voxels at tissue boundaries (cord and cerebrospinal fluid or white matter/gray matter) that may have been a result of misregistration or partial volume effects, the ROIs were eroded by a disk-shaped structuring element with a radius of four voxels in the white matter and one voxel in the gray matter.

### *5.2.4 Image Analysis*

Signal-to-noise ratio (SNR) was found to be approximately 30 across all tracts ( $30.8 \pm 7.44$ ), and hence a homogenous Rician noise throughout the entire spinal cord ( $\sigma=0.05$ ) was assumed in all subsequent analyses. Using the two acquired  $b_0$  images, a single  $b_0$  image was estimated using a maximum likelihood approach, where the single  $b_0$  signal was predicted by minimizing the objective function using a Rician noise model (16).

SMT fitting to the diffusion-weighted data was performed using in-house MATLAB code, and yielded maps of the apparent intra-axonal volume fractions ( $v_{ax}$ ) and the intra-axonal diffusivity ( $D_{ax}$ ).

### *5.2.5 Statistical Analysis*

Reproducibility of the SMT-derived indices in white matter of healthy controls were assessed using Bland Altman (105). The mean index within a given ROI (white matter) for each subject was calculated and was entered as a single data point for the Bland Altman analysis. The 95% confidence interval (CI) for the mean difference was calculated to determine whether the interval overlapped zero at  $\alpha=0.05$ , which would indicate that the differences between scan and rescan were non-significant at the  $\alpha = 0.05$  level. The normalized Bland Altman ( $D_{BA}$ ) was also

used as an estimate of reliability to be used for comparison across derived indices, calculated as:

$$D_{BA} = \frac{D_{12}}{M} * 100\% \quad (36)$$

where  $D_{12}$  is the mean difference between the two sessions and  $M$  is the mean diffusion-derived index of interest. Additionally, a nonparametric Wilcoxon signed rank was performed, in addition to the Bland Altman analysis, to determine whether a significant difference exists between the median of each diffusion-derived index for each of the two scans at  $\alpha=0.05$ .

Group comparisons between healthy controls and MS patients were performed to assess differences in SMT-derived indices. For controls, the mean value was calculated over all white matter, which was defined using the automatically segmented ROIs as previously described; for MS patients, white matter was further manually delineated into lesion and normal appearing white matter (NAWM) from the mFFE images. For each SMT-derived index ( $v_{ax}$  and  $D_{ax}$ ), three non-parametric Wilcoxon rank sum tests were performed to compare (i) healthy white matter vs. lesions, (ii) healthy white matter vs. NAWM and (iii) lesions vs. NAWM at a significant threshold of  $\alpha=0.05$ .

## 5.3 Results

### 5.3.1 *In Vivo Results and Reproducibility*

Figure 17a shows the averaged anatomical and SMT-derived maps over all healthy controls, with the anatomical mFFE image on the left, the  $v_{ax}$  map in the middle, and the  $D_{ax}$  map on the right. In the anatomical image, there is contrast between white and gray matter. The averaged  $v_{ax}$  map indicates heterogeneity in the microenvironments of the spinal cord, with lower values in the gray matter relative to the white matter. This contrast is expected because  $v_{ax}$  represents the apparent intra-neurite volume fraction in gray matter, which is lower than the intra-axonal volume fraction in the white matter. The  $D_{ax}$  map shows higher diffusivities in the white matter, where the organization of fibers within a fiber population primarily align with one axis and therefore do not present many barriers to diffusion. It should be noted that there are some unrealistic fitted values only at the boundaries of the cord, which we ascribe to misregistration, which would also be observed in conventional DTI-derived parametric maps.

Figure 17b displays the histograms of all the white matter voxels over all of the controls for scan 1 (black) and scan 2 (dashed blue). The histograms of the scan and rescan largely overlap one another, indicating high reproducibility for both  $v_{ax}$  and  $D_{ax}$ . There is a spike around  $3 \mu\text{m}^2/\text{ms}$  in the  $D_{ax}$  histogram, which demonstrates the close-to-unrestricted diffusion present along the main spinal cord axis.

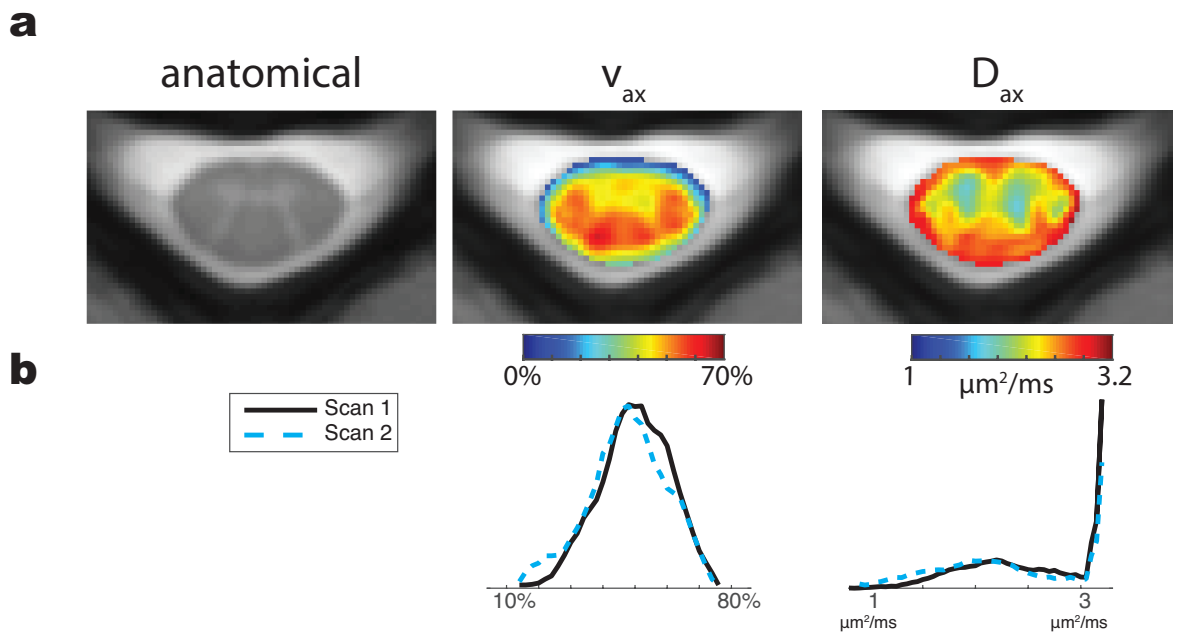


**Figure 17: Mean SMT-derived maps and reproducibility in controls.** (a) From left to right, mean anatomical (mFFE) image, mean  $v_{ax}$  and mean  $D_{ax}$  over all controls. (b) Histograms of all white matter voxels over all controls for scan 1 and scan 2. The overlap between the two histograms signifies high inter-scan reproducibility of the derived indices.

Table 7 lists the reproducibility statistics from Bland Altman and the Wilcoxon rank sum test. The 95% CIs for the mean differences of both indices overlap 0 and yield a  $D_{BA}$  of less than 10%, indicating that the differences between scan and rescan are small and that SMT is capable of providing reliable indices over time.

Table 7: Reproducibility of SMT-derived indices.

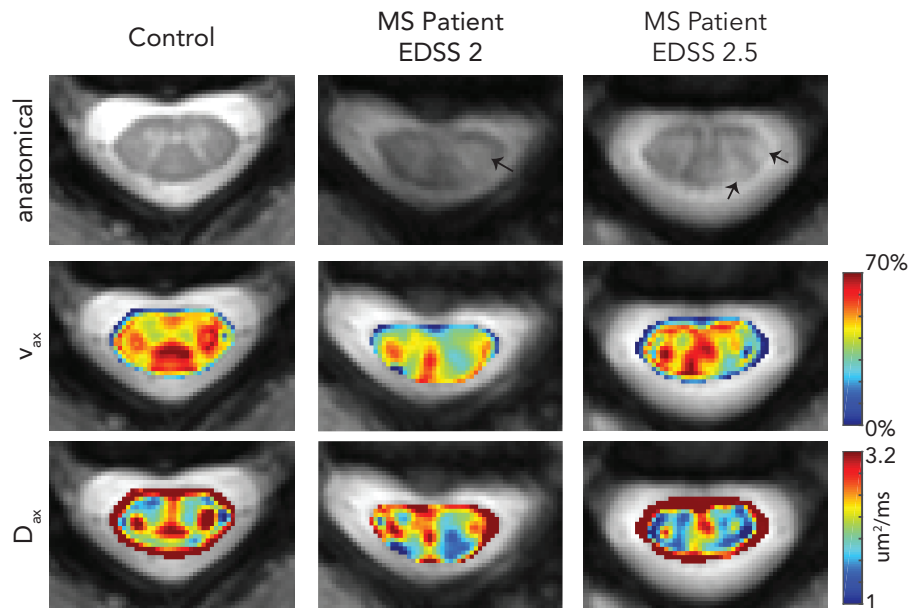
<b>SMT</b>	<b>Scan 1</b>	<b>Scan 2</b>	<b>Bland-Altman</b>			<b>WSR</b>
	<i>mean±s.d.</i>	<i>mean±s.d.</i>	<i>Difference</i>	<i>95% CI</i>	<i>D<sub>BA</sub> (%)</i>	<i>p-value</i>
$V_{ax}$	49.3±4.43%	47.1±9.20%	2.29	[-6.60, 1.12]	4.75	0.88
$D_{ax}$	2.46±0.21	2.23±0.44	0.23	[-0.222, 0.682]	9.81	0.13

### 5.3.2 Application to MS Cohort

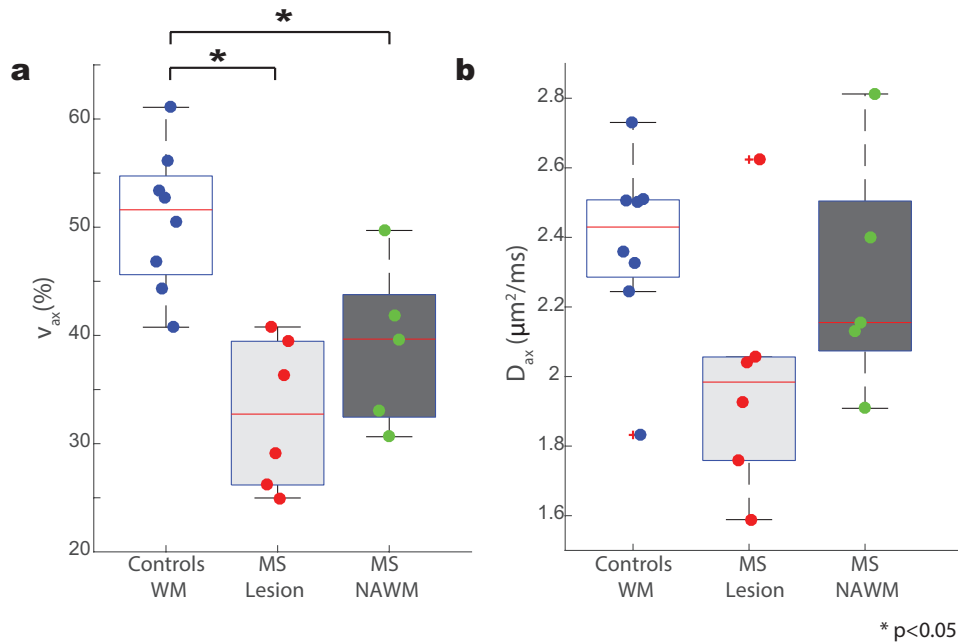
Figure 18 displays the SMT-derived maps for a representative control and two MS patients. The MS patient in the middle column (patient 1) has an EDSS of 2 with a disease duration of 17 years; the MS patient in the right column (patient 2) has an EDSS of 2.5 with a disease duration of 8 years. For patient 1, a lesion can be seen in the left lateral column (black arrow), and corresponds to a decreased  $v_{ax}$  and  $D_{ax}$ . For patient 2, smaller lesions are observed in the left dorsal column and left lateral column, and the same trends of decreased  $v_{ax}$  and  $D_{ax}$  are seen in the SMT-derived maps.

Figure 19 displays the box-and-whisker plots for  $v_{ax}$  (Figure 19a) and  $D_{ax}$  (Figure 19b) comparing healthy white matter (white), MS lesions (light gray) and MS NAWM (dark gray). In comparison to white matter in healthy controls, a significant decrease in  $v_{ax}$  is observed in the lesions ( $p=0.001$ ) and NAWM ( $p=0.019$ ). No significant trends exist for  $D_{ax}$ , however a trend towards decreased  $D_{ax}$  is observed at the site of the lesion.





**Figure 18: Anatomical images (top), SMT-derived maps  $v_{ax}$  (middle) and  $D_{ax}$  (bottom) are displayed for control (left) and two patients. MS patient 1 (middle), EDSS 2 and duration of disease of 17 years, highlights a decreased  $v_{ax}$  at the site of the lesion (black arrow) in the left lateral column. MS patient 2 (right), EDSS 2.5 and duration of disease 8 years, demonstrates similar trends in  $v_{ax}$  to the MS patient 1.**



**Figure 19: Application of SMT in MS cohort.** Boxplots highlighting the median, 25<sup>th</sup> and 75<sup>th</sup> percentiles over controls (WM) and MS patients (lesions and NAWM) for (a)  $v_{ax}$  and (b)  $D_{ax}$ . Mean values from each subject plotted and asterisks indicate significant differences between the groups.

## 5.4 Discussion

Our results demonstrate (i) the feasibility of SMT in the human spinal cord *in vivo* and (ii) the sensitivity of SMT-derived indices in the spinal cord of MS. Recently, there has been a push towards the implementation of advanced diffusion models beyond conventional DTI to study human healthy and diseased spinal cord *in vivo*. Farrell et al. demonstrated the feasibility of q-space imaging in healthy controls, and showed the potential of displacement and probability maps in providing useful contrasts for characterizing microstructural damage in MS (50). Grussu et al. demonstrated the reproducibility of NODDI-derived indices in the healthy cervical spinal cord, enabling the estimation of indices more specific to neurite morphology than DTI (75). Duval et al. implemented q-space AxCaliber using Human Connectome gradients (80) to estimate axon diameters of the spinal cord (79). These studies demonstrate the advantages of characterizing spinal cord microstructure using advanced multi-compartment diffusion models. Compared with these methods, SMT is an attractive biophysical model to characterize specific tissue properties. SMT makes no assumptions about the orientation of fibers or the fast exchange in the extra-neurite space. Therefore, SMT is insensitive to the confounding influence on estimation accuracy caused by pathology, such as inflammation-induced changes in fiber orientation distribution, which may in turn enable SMT to provide valuable information on the apparent axonal volume fraction or intra-axonal diffusivity. Furthermore, the protocol used in the current study is clinically feasible on standard MRI scanners and does not rely on extremely powerful gradient systems, which is of high interest when translating SMT to characterize specific neural tissue properties in a clinical setting.

To evaluate the utility of SMT in the spinal cord, we applied SMT on a cohort of MS patients. This feasibility study shows that SMT is sensitive in identifying abnormal changes in MS lesions when compared to healthy white matter. The decreased apparent axonal volume fraction  $v_{ax}$  in MS lesions is consistent with histopathological studies (134) as well as other previous *in vivo* reports using NODDI (122). With MS, an immune response is triggered followed by blood brain barrier leakage, ultimately resulting in axonal damage, which can cause disability in patients and potentially, consequential death at end stage pathology in MS. The ability to detect changes in axonal loss may have clinical potential such as modified treatment plans, especially in those patients who have yet to demonstrate clinical disability or those without significant atrophy or irreparable axonal loss. A longitudinal study involving a larger

cohort of patients is warranted. Furthermore, to derive meaningful clinical consideration from this newly developed method, work on the association between SMT-derived indices and patients' disability, as well as on longitudinal changes of these indices over time, should be investigated.

Due to the difficulty in registering spinal cord diffusion-weighted volumes, misfittings at the boundaries of the spinal cord and CSF are evident, but it is important to note that this affects all diffusion MR images. Interleaving more  $b_0$  images throughout the acquisition may provide more accurate registration transformations (75). Misfittings at the boundaries may also be minimized by increasing the spatial resolution of the protocol, and should be further investigated in future studies to potentially distinguish different spinal cord tracts. The main goal of this study, however, was to test the feasibility of SMT in the spinal cord, and consequently, the protocol was optimized in terms of SNR in order to minimize any potential biases in the SMT fitting. To this end, a large slice thickness (slice thickness = 10 mm) was also employed in order to maximize SNR, which is not problematic since this covered approximately one cervical level rostral-caudally. Furthermore, given the rostral-caudal symmetry of the spinal cord at each cervical level, there is no concern for partial voluming effects between CSF and spinal cord tissue. For the MS patients, lesions were evaluated slice-by-slice on the anatomical image (slice thickness = 5 mm) and after inspection, the lesion ROI was delineated on the averaged anatomical image to ensure that normal appearing white matter voxels were not averaged into the region of interest.

In summary, this study delivers a multi-shell diffusion characterization of the cervical spinal cord with SMT. This method carries a high degree of reproducibility and shows the clinical potential of SMT in characterizing axonal pathology in MS.

## CHAPTER 6

### Diffusion Basis Spectrum Imaging: Application to MS

#### 6.1 Introduction

While NODDI and SMT are able to resolve axonal fractions, they do not consider the restricted water diffusion outside fiber tracts (restricted isotropic component). The restricted water diffusion outside of the fiber tracts may be a measure of cellularity (11), which would be valuable in the study of MS to possibly track disease evolution. Furthermore, by separating this component from the anisotropic tensor, a more accurate measure of axial diffusivity (AD or  $\lambda_{\parallel}$ ) and radial diffusivity (RD or  $\lambda_{\perp}$ ) may be obtained.

Diffusion basis spectrum imaging (DBSI) is a recently developed technique that models white matter diffusion as a linear combination of multiple discrete anisotropic tensors and a spectrum of isotropic diffusion tensors. The discrete anisotropic tensors represent intra-axonal tracts. The isotropic tensors are divided into two compartments: 1) the summation of the isotropic spectrum from  $0 \leq \text{ADC} \leq 0.3 \mu\text{m}^2/\text{ms}$  infer restricted diffusion, reflecting cellularity and 2) the summation of the isotropic spectrum at  $0.3 < \text{ADC} < 3 \mu\text{m}^2/\text{ms}$  is considered non-restricted diffusion outside of axonal tracts, reflecting vasogenic edema and CSF.

DBSI has been demonstrated in tissue phantoms and mice (trigeminal nerves, optic nerve, spinal cord) to resolve crossing fiber tracts, remove CSF partial volume effects and quantify axonal injury, demyelination and inflammation (11,67,76,77). There is significant value that DBSI can offer to the study of MS. For example, DTI can estimate axonal injury and demyelination in a voxel whose signal is largely from coherent axonal fibers (42). During inflammation, however, voxel signals are conflicted with infiltrated cells undergoing axon and myelin injury; in this scenario, DTI generally underestimates the demyelination and overestimates the effect of axonal injury (4,135). During axonal loss, there is an increased isotropic diffusion component, but the DTI model exaggerates  $\lambda_{\perp}$  and  $\lambda_{\parallel}$  (136). Because the DBSI model separates the diffusion signal into different components, DBSI may be able to discern these pathologies and provide higher sensitivity and specificity than conventional DTI.

### 6.1.2 Model Theory

The DBSI signal is modeled as:

$$S_k = \sum_{i=1}^{N_{aniso}} f_i e^{-|\overline{b}_k| \lambda_{\perp i}} e^{-|\overline{b}_k| (\lambda_{\parallel i} - \lambda_{\perp i}) \cos^2 \psi_{ik}} + \int_a^b f(D) e^{-|\overline{b}_k| D} dD \quad (37)$$

In Equation 37,  $S_k$  is the measured signal intensity acquired at the  $k$ -th diffusion gradient normalized (to  $b=0$  s/mm<sup>2</sup>);  $|\overline{b}_k|$  is the  $b$ -value of the  $k$ -th diffusion gradient. The unknown variables to be solved in the anisotropic term include  $N_{aniso}$ , the number of anisotropic tensors;  $f_i$ , the signal intensity fraction for the  $i$ -th anisotropic tensor;  $\psi_{ik}$ , the angle between the  $k$ -th diffusion gradient and the principal direction of the  $i$ -th anisotropic tensor;  $\lambda_{\parallel i}$  and  $\lambda_{\perp i}$ , the respective axial and radial diffusivities for the  $i$ -th anisotropic tensor under the assumption of cylindrical symmetric tensors. For the isotropic component, the isotropic diffusion spectrum  $f(D)$  must be solved over chosen diffusivity limits  $a$  to  $b$ . (For clarification, the isotropic diffusion spectrum may also be referred herein as  $f_{iso}$ .) To solve this model, a two-step approach is taken to simplify the number of free variables needed.

First,  $N_{aniso}$  and  $\psi_{ik}$  are determined by employing a diffusion basis decomposition approach (137). A diffusion basis function (DBF) is created from a set of basis tensors uniformly distributed in a 3D space. In DBSI, a DBF is created for each anisotropic term and is given as:

$$\phi_{ik} = c_i e^{-|\overline{b}_k| \lambda_{\perp i}} e^{-|\overline{b}_k| (\lambda_{\parallel i} - \lambda_{\perp i}) \cos^2 \theta_{ik}} \quad (38)$$

where  $\phi_{ik}$  is a discrete, anisotropic DBF for the  $i$ -th diffusion basis tensor and  $k$ -th diffusion gradient direction; our algorithm uses  $N=129$  diffusion basis tensors. Isotropic diffusion is modeled as a single DBF:

$$\phi_{i,N+1} = c_{N+1} e^{-|\overline{b}_k| d_{iso}} \quad (39)$$

Thus, the diffusion basis decomposition approach computes the best linear combination of DBFs that are able to reproduce the signal  $S_k$ :

$$S_k = \sum_{i=1}^N c_i e^{-|\bar{b}_k| \lambda_{\perp i}} e^{-|\bar{b}_k| (\lambda_{\parallel i} - \lambda_{\perp i}) \cos^2 \theta_{ik}} + c_{N+1} e^{-|\bar{b}_k| d_{iso}} \quad (40)$$

To solve Equation 40, the DBFs must have a known set of diffusivities,  $\lambda_{\perp}$  and  $\lambda_{\parallel}$ . An optimization procedure is initialized with a set of diffusivities,  $\lambda_{\perp}$ ,  $\lambda_{\parallel}$ , and  $d_{iso}$ , derived from the tensor. Given a set of diffusivities,  $\lambda_{\perp}$ ,  $\lambda_{\parallel}$ , and  $d_{iso}$ , a non-linear regularized least-squares analysis of  $S_k$  is performed to solve for the weighted coefficients  $c_i$  for a discrete set of DBFs. The fitting procedure for  $\lambda_{\perp}$ ,  $\lambda_{\parallel}$ , and  $d_{iso}$  was analyzed by the minimum sum of squares and once converged at the global minimum, a continuous DBF solution is solved for, providing  $N_{aniso}$  and the corresponding principal directions  $\psi_{ik}$  based on the nonzero  $c_i$ .

The second step to solving Equation 37 optimizes  $\lambda_{\perp i}$ ,  $\lambda_{\parallel i}$ , and  $f_i$  for each anisotropic tensor. Again, the nonlinear optimization problem is solved by initialization of a selected  $\lambda_{\perp i}$  and  $\lambda_{\parallel i}$  to compute corresponding  $f_i$  and  $f(D)$ .  $f(D)$  is uniformly discretized by L points from [a, b], where [a, b] = [0,3  $\mu\text{m}^2/\text{ms}$ ] as defined by (11), to simplify the problem into a linear least-square analysis. Knowing that the signal intensities cannot be negative, the problem is solved using a regularized non-negative least-squares analysis with incorporated finite signal energy to avoid over-fitting noisy data. Once the solution converges to a global minimum, all of the variables in Equation 37 are accounted for. Table 8 summarizes the DBSI model.




## 6.2 Methods

### 6.2.1 Human Subjects

Local institutional review board approval and written informed consent were obtained prior to imaging. Five healthy controls (29.2 $\pm$ 5.36 years, 2M/3F) participated in this study to assess reproducibility, all of which were rescanned within a month. Six relapsing-remitting MS patients (38.2 $\pm$ 5.93 years, 6F) were recruited for this study. While some of the patients from the NODDI and SMT study also participated in this study, the cohort was slightly different from the NODDI and SMT dataset. Patients' disability was rated using the Expanded Disability Status Scale (EDSS) score (22), and ranged from 0 to 6 for the patients enrolled in this study. Although some of the patients were known to have spinal cord disease from previous clinical scans, none of them were experiencing an acute exacerbation. All patients had been free from steroid

administration for at least 6 months.

Table 8: Summary of DBSI model.

Compartment	Model	DOF	Assumptions	Resulting DOF
Intra-axonal + water molecules outside but adjacent to axon fibers	Hindered, Anisotropic Tensor 	$N_{\text{aniso}}$ $f_{\text{aniso}}$ $\psi_{ik}$ (principal directions) $AD_i$ $RD_i$	$N_{\text{aniso}}=1$  Use set of DBF	$f_{\text{aniso}}$ $\psi_{ik}$ AD  RD
Cells	Isotropic Restricted 	$f(D)$	$0 < \text{ADC} \leq 0.3 \mu\text{m}^2/\text{ms}$	$f_{\text{iso, restricted}}$
Free water (CSF), Vasogenic Edema	Isotropic Non-Restricted 	$f(D)$	$0.3 < \text{ADC} \leq 3 \mu\text{m}^2/\text{ms}$	$f_{\text{iso, non-restricted}}$

### 6.2.2 In Vivo Imaging

Scans were performed on a 3.0T whole body MR scanner (Philips Achieva, Best, Netherlands), using a dual channel body coil for excitation and a 16-channel SENSE neurovascular coil for reception. All imaging was centered at the C3/C4 level, except for one MS patient centered at C4/C5 where more lesions were known to be present. In each scan session, an anatomical image was acquired consisting of a high-resolution, multi-echo gradient echo (mFFE) (100) with the following relevant parameters: resolution=0.65x0.65x5 mm<sup>3</sup>,

TR/TE/ $\Delta$ TE=753/7.1/8.8 ms,  $\alpha=28^\circ$ , number of slices=14 and acquisition time=6:12 min. The spin-echo diffusion sequence was cardiac triggered and utilized a single-shot echo planar imaging (EPI) readout. Reduced field-of-view was implemented using an outer volume suppression technique (82). One slice was acquired with the following parameters: TR/TE=3 beats ( $\sim 3000$  ms)/65 ms, resolution=1.25 x 1.25 mm<sup>2</sup>, slice thickness=10 mm, FOV=68 x 52 mm, SENSE (AP)=1.5, fat suppression was performed using Spectral Saturation with Inversion Recovery (SPIR), NSA=4. The diffusion gradient encoding scheme consisted of 99 directions, where the vectors are defined as ( $q_x, q_y, q_z$ ) and are prescribed in the three-dimension q-space satisfying  $q_x^2 + q_y^2 + q_z^2 = r^2$  directions, with a maximum b-value of 2000 s/mm<sup>2</sup>. A total of eight non-diffusion-weighted scans ( $b=0$  s/mm<sup>2</sup> or  $b_0$ ) were acquired, interleaved evenly throughout the acquisition. Total acquisition time was 21:18 min.

### 6.2.3 Image Pre-Processing

In each scan, the anatomical image (mFFE) was used as a reference template for registration and segmentation. Registration was performed using ANTS (126). The eight interleaved  $b_0$  images from the diffusion-weighted scan were diffeomorphically registered to the anatomical, and all other diffusion-weighted volumes were subsequently registered to the closest  $b_0$  image using an affine transformation to correct for eddy current distortions (127).

Segmentation was performed using the same procedure that was used for NODDI and SMT, where a groupwise multi-atlas method was used to automatically segment the anatomical image into regions of interest (ROIs) of white matter and gray matter (103). To avoid inaccurate voxels at tissue boundaries (cord and cerebrospinal fluid or white matter/gray matter) that may have been a result of misregistration or partial volume effects, the ROIs were eroded by a disk-shaped structuring element with a radius of four voxels in the white matter and one voxel in the gray matter.

### 6.2.4 Image Analysis

DBSI fitting was performed using in-house MATLAB code, and yielded maps of the anisotropic fraction ( $f_{\text{anisotropic}}$ ), the isotropic restricted fraction ( $f_{\text{isotropic, restricted}}$ ), the isotropic non-restricted fraction ( $f_{\text{isotropic, non-restricted}}$ ), the axial diffusivity for the anisotropic tensor (AD), and the radial diffusivity for the anisotropic tensor (RD). For this study, since white matter tracts are



primarily coherent in the spinal cord, the number of anisotropic tensors was restricted to  $N_{\text{aniso}}=1$  (11).

The nonlinear least squares problem was minimized by the residuals of the fit and data using the `lsqnonlin` function in MATLAB. For both healthy controls and MS patients, the fit of the model was assessed using a Chi-square goodness-of-fit, where the number of degrees of freedom was set to 94. Resulting p-values from the test were mapped voxel-by-voxel where  $p < 0.05$  indicated a significant difference from the fit and data.

### 6.2.5 Statistical Analysis

Statistical analysis was performed similar to the NODDI and SMT. For convenience, the analysis is recapped here. Reproducibility of the DBSI-derived indices in white matter of healthy controls were assessed using Bland-Altman (105). The mean index within a given ROI (white matter) for each subject was calculated and was entered as a single data point for the Bland Altman analysis. The 95% confidence interval (CI) for the mean difference was calculated to determine whether the interval overlapped zero at  $\alpha=0.05$ , which would indicate that the differences between scan and rescan were non-significant at the  $\alpha = 0.05$  level. The normalized Bland Altman ( $D_{BA}$ ) was also used as an estimate of reliability to be used for comparison across derived indices, calculated as:

$$D_{BA} = \frac{D_{12}}{M} * 100\% \quad (41)$$

where  $D_{12}$  is the mean difference between the two sessions and  $M$  is the mean diffusion-derived index of interest. Additionally, a nonparametric Wilcoxon signed rank was performed, in addition to the Bland Altman analysis, to determine whether a significant difference exists between the median of each diffusion-derived index for each of the two scans at  $\alpha=0.05$ .

Group comparisons between healthy controls and MS patients were performed to assess differences in DBSI-derived indices. For controls, the mean value was calculated over all white matter, which was defined using the automatically segmented ROIs as previously described; for MS patients, white matter was further manually delineated into lesion and normal appearing white matter (NAWM) from the mFFE images. For each DBSI-derived index ( $f_{\text{anisotropic}}$ ,  $f_{\text{isotropic}}$ ,  $f_{\text{restricted}}$ ,  $f_{\text{isotropic, non-restricted}}$ , AD, RD), three non-parametric Wilcoxon rank sum tests were

performed to compare (i) healthy white matter vs. lesions, (ii) healthy white matter vs. NAWM and (iii) lesions vs. NAWM at a significant threshold of  $\alpha=0.05$ .

## 6.3 Results

### 6.3.1 In Vivo Results and Reproducibility

Figure 20a shows the averaged anatomical and DBSI-derived maps over all healthy controls, with the anatomical mFFE image on the top row, followed by the  $f_{\text{anisotropic}}$ ,  $f_{\text{isotropic, restricted}}$ ,  $f_{\text{isotropic, non-restricted}}$ , AD and RD maps. In the anatomical image, there is high white matter/gray matter contrast. The averaged  $f_{\text{anisotropic}}$  map indicates heterogeneity in the different tissues of the spinal cord, with lower fractional values in the gray matter relative to the white matter. This contrast is expected, as the  $f_{\text{anisotropic}}$  is a representation of the intra-axonal water molecules and those outside, but adjacent to the axon fibers, and therefore highlights the coherently organized white matter tracts. The isotropic restricted fraction map represents the restricted diffusion inside cells, and therefore is intended to be a measure of cellularity. In the isotropic restricted fraction map below, there is a higher concentration of isotropic restricted diffusion in gray matter as a result of the presence of glial cells, cell bodies and neutrophils; the white matter consists of very low values for isotropic restricted diffusion, since the white matter is expected to contain primarily coherent, organized tracts. The isotropic non-restricted fraction is a measure of hindered and/or free diffusion ( $0.3 < \text{ADC} < 3 \mu\text{m}^2/\text{ms}$ ), representing CSF in healthy controls, or in diseased tissue, hindered diffusion in the presence of vasogenic edema or free diffusion when tissue is loss. As expected, only the boundaries of the spinal cord and CSF are highlighted, where partial voluming effects may be present. The AD and RD maps represent the diffusion for the anisotropic tensor only, and therefore are unconfounded by vasogenic edema and cellularity. For the healthy controls, the AD and RD are similar to the DTI-derived AD and RD maps, which is expected in healthy controls since there is no presence of vasogenic edema or cellularity confounding these measurements. With AD, higher AD is present in the white matter in comparison to gray matter, and with RD, there is higher transverse diffusivity in the gray matter than white matter. Finally, it should be noted that in all maps, there are some unrealistic fitted values only at the boundaries of the cord, which we ascribe to misregistration, which would also be observed in conventional DTI-derived parametric maps.

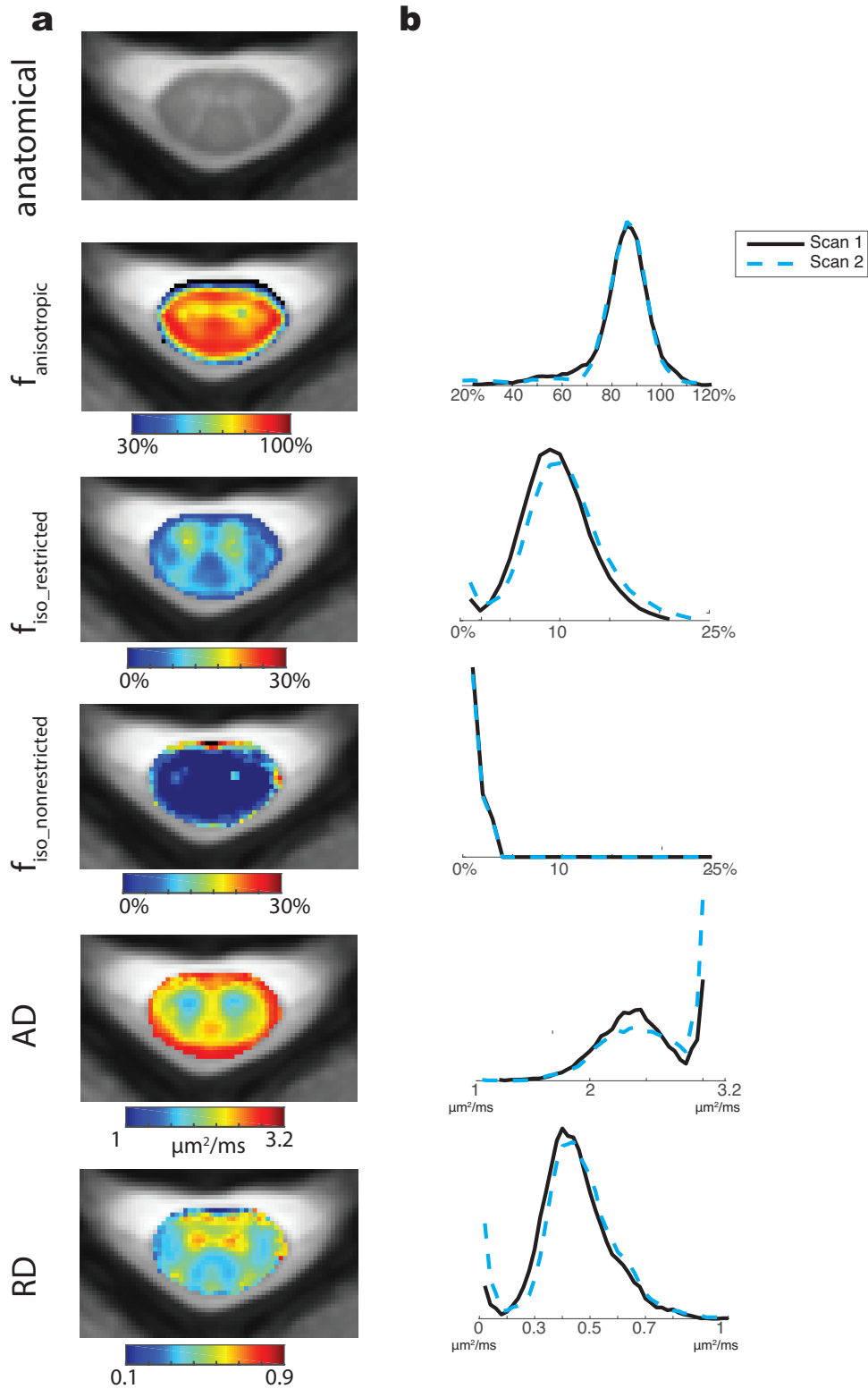


**Figure 20: DBSI-derived maps and histograms.** (a) Mean anatomical image and DBSI-derived maps over all healthy controls. (b) Histograms of all white matter voxels over all controls for scan and rescan.

Figure 20b displays the histograms of all the white matter voxels over all of the controls for scan 1 (black) and scan 2 (dashed blue) to provide a measure of reproducibility. The histograms of the scan and rescan largely overlap one another, indicating high reproducibility for all of the indices. Table 9 lists the reproducibility statistics from Bland Altman and the Wilcoxon rank sum test. With the exception of  $f_{\text{isotropic, non-restricted}}$ , the 95% CIs for the mean differences of both indices overlap 0 and yield a  $D_{\text{BA}}$  of less than 10%, indicating that the differences between scan and rescan are small. Since the non-restricted isotropic fractions are expected to be close to 0 in healthy controls, the  $D_{\text{BA}}$  will reflect an exaggerated difference in the two scans when normalized by a small mean value. The histograms as shown in Figure 20b, however, largely overlap one another, which indicates the  $f_{\text{isotropic, non-restricted}}$  may still be a useful, reliable measure.

Table 9: Reproducibility of DBSI-derived indices.

<b>DBSI</b>	<b>Scan 1</b>	<b>Scan 2</b>	<b>Bland-Altman</b>		<b>WSR</b>
	<i>mean±s.d.</i>	<i>mean±s.d.</i>	<i>Difference</i>	<i>95% CI</i>	<i>D<sub>BA</sub> (%)</i> <i>p-value</i>
$f_{\text{aniso}}$	82.8±2.33%	82.0±7.31%	6.96	[-7.81, 9.49]	1.02 0.81
$f_{\text{iso\_restricted}}$	9.01±1.13%	9.95±1.32%	-0.94	[-2.82, 0.94]	9.89 0.19
$f_{\text{iso\_nonrestricted}}$	1.25±0.99%	2.80±2.71%	-1.55	[-5.19, 2.08]	76.5 0.81
$AD^*$	2.39±0.11	2.48±0.10	-0.09	[-0.22, 0.04]	3.62 0.25
$RD^*$	0.44±0.05	0.45±0.02	-0.01	[-0.08, 0.06]	2.74 0.63

\*units of  $\mu\text{m}^2/\text{ms}$

### 6.3.2 Application to MS

Figure 21 shows three example cases, with a healthy representative control on the left, an MS patient (MS patient 1) with an EDSS of 2 and disease duration of 17 years in the middle, and another MS patient (MS patient 2) with an EDSS of 2.5 and disease duration of 8 years on the right. In the representative control, the same trends, as described earlier for the mean control maps, are observed. The anisotropic fraction is high in white matter, while the isotropic restricted fraction mainly highlights the gray matter. The isotropic non-restricted fraction is low throughout

all of the spinal cord, and is only evident at the boundaries of the cord, where partial volume effects may be present.

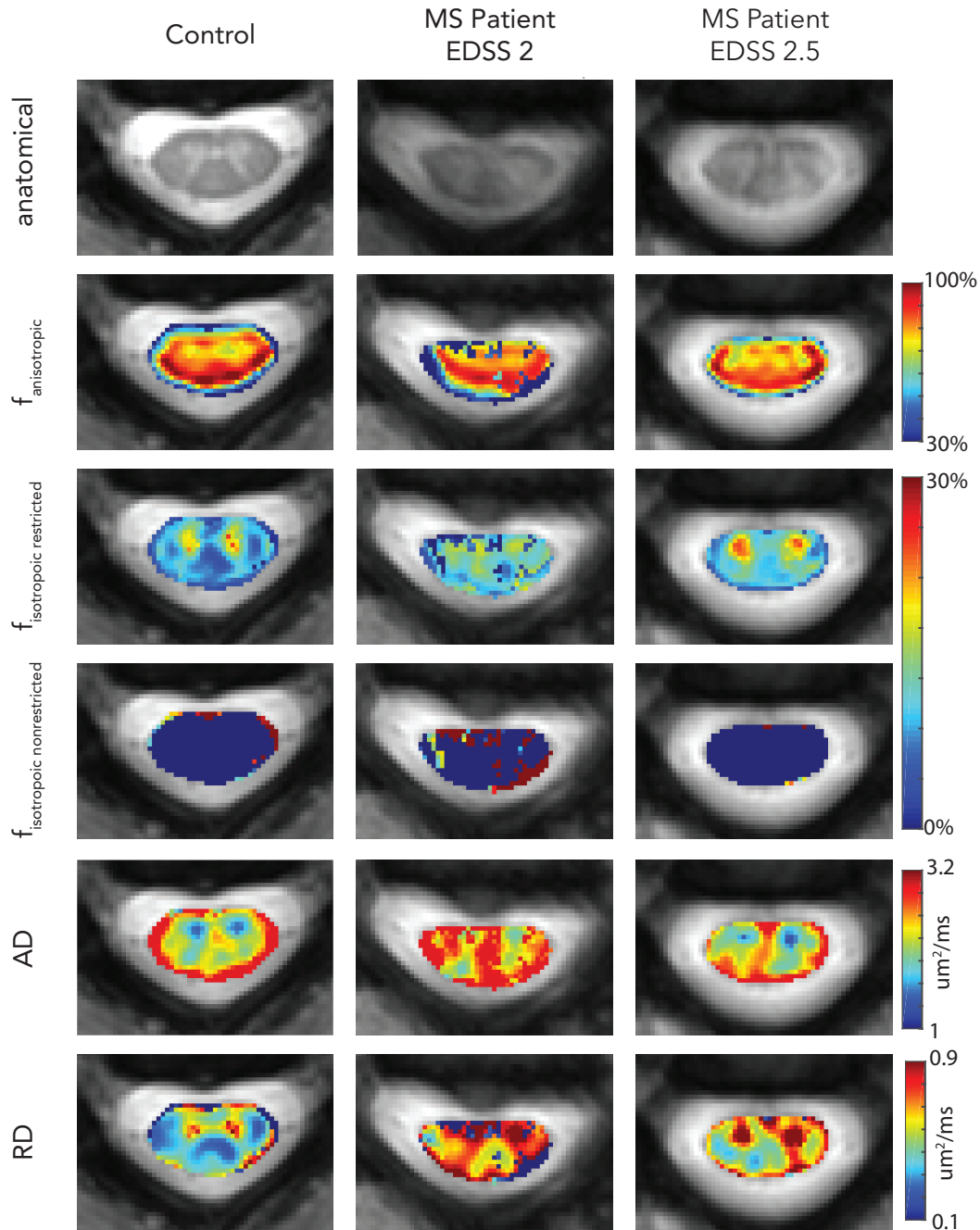


**Figure 21: Anatomical images (top), with DBSI-derived maps following, are displayed for control (left) and two patients (right). MS patient 1 (middle), EDSS 2 and duration of disease of 17 years; MS patient 2 (right), EDSS 2.5 and duration of disease 8 years.**

In MS patient 1, the anisotropic fraction is decreased in the white matter ( $f_{\text{anisotropic}}=72.3\%$ ) relative to the healthy control ( $f_{\text{anisotropic}}=81.1\%$ ), however the change is not localized to the lesions or NAWM; rather, the decrease appears to be attributed to misfit voxels throughout the cord. There is an increase in the isotropic non-restricted fraction, which could indicate an increase in vasogenic edema in an MS patient, however these increases are speckled throughout the cord and appear noisy. With RD, again the map is noisier than the control, but an increase is observed throughout the cord (lesion= $0.66 \mu\text{m}^2/\text{ms}$ , NAWM= $0.63 \mu\text{m}^2/\text{ms}$ ). No notable changes are observed in the isotropic restricted fraction or AD maps.

For MS patient 2, the maps do not appear as noisy as MS patient 1, however the changes are subtle. The isotropic restricted fraction (third row) is slightly higher in the white matter in the MS patient ( $f_{\text{isotropic, restricted}}=11.9\%$ ) in comparison to the healthy control ( $f_{\text{isotropic, restricted}}=8.76\%$ ). The AD is slightly lower at the site of the lesion (MS lesion= $2.28 \mu\text{m}^2/\text{ms}$ , healthy control WM= $2.39 \mu\text{m}^2/\text{ms}$ ); for RD, there is an increase at the site of the lesion (MS lesion= $0.61 \mu\text{m}^2/\text{ms}$ , control= $0.38 \mu\text{m}^2/\text{ms}$ ).

Figure 22 summarizes the group trends between healthy control white matter (white), and MS white matter tissue in terms of lesions (gray) and NAWM (dark gray) for the DBSI-derived indices. There are several trends to highlight, however, it is important to note that only significant differences exist for RD. With the anisotropic fraction, in comparison to healthy controls, a trend towards decreased anisotropic diffusion fraction (Figure 22a) is observed at the site of the lesion (healthy: 82.8%, MS lesions: 81.3%,  $p=0.75$ ) and in NAWM (healthy: 82.8%, MS NAWM: 76.8%,  $p=0.28$ ). In the MS patients, there appears to be an increase in cellularity, as indicated by the trend (healthy vs. lesions:  $p=0.43$ , healthy vs. NAWM:  $p=0.31$ ) towards increased isotropic restricted fraction (Figure 22b). Additionally, the increase in the isotropic non-restricted fraction (Figure 22c) in the MS cohort (healthy: 1.25%, lesions: 5.17%, NAWM: 5.12%) would be interpreted as vasogenic edema being present or tissue loss in patients with more severe disease, however no significant comparisons exist (healthy vs. lesion:  $p=0.50$ , healthy vs. NAWM:  $p=0.31$ ). A slight decrease in AD is observed at the site of the lesion (healthy:  $2.39 \mu\text{m}^2/\text{ms}$ , lesion:  $2.36 \mu\text{m}^2/\text{ms}$ ,  $p=0.93$ ), along with a significant difference in RD at both the site of the lesion ( $p=0.004$ ) and NAWM ( $p=0.008$ ).

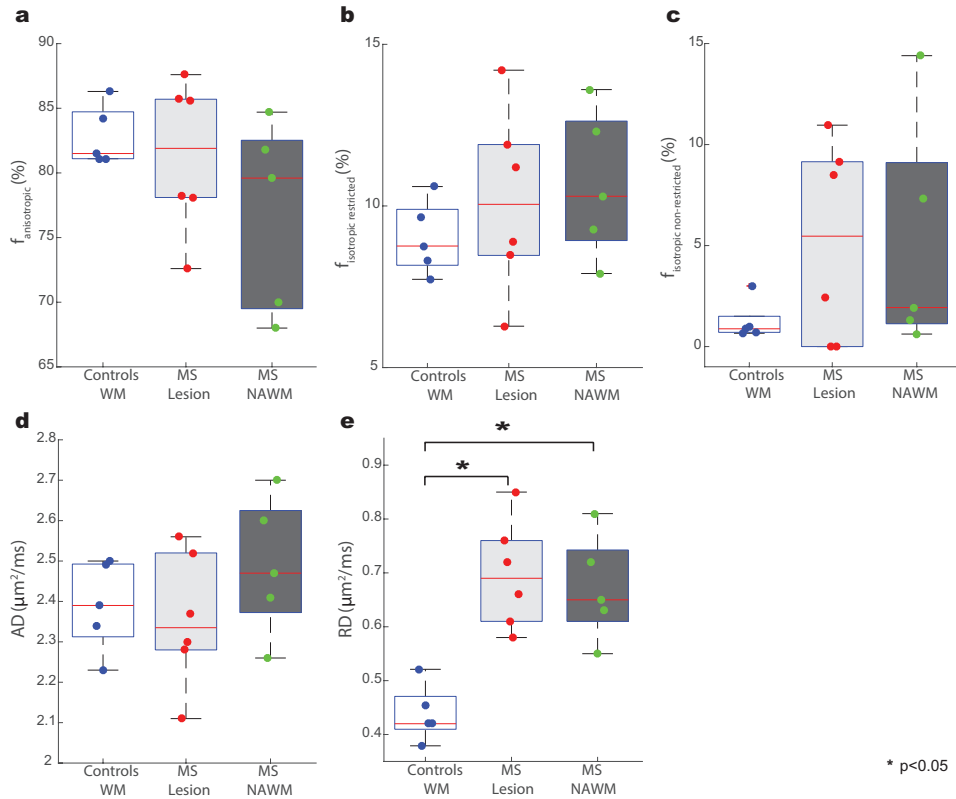


**Figure 22: Boxplots highlighting group trends for DBSI-derived indices in healthy controls and MS patients.** (a) Anisotropic fraction, (b) Isotropic restricted fraction, (c) Isotropic non-restricted fraction, (d) AD for anisotropic tensor, and (e) RD for anisotropic are displayed.

Figure 23 shows the p-value maps from the Chi-square goodness-of-fit test for the same healthy control (Figure 23a) and MS patient 1 (Figure 23d) in Figure 21. Blue voxels are highlighted as having  $p < 0.05$ , which indicates that there is a significant difference between the fit and the data. The mean p-value over healthy white matter in this control ( $p = 0.32$ ) indicates a reasonable model fit to the data over white matter voxels.

For the MS patient, the Chi-square goodness-of-fit indicates a significant difference ( $p < 0.01$ ) between the model fit and the test yields a mean p-value of 0.008 over all the white matter voxels. Interestingly, the misfits ( $p < 0.05$ ) are not localized to lesions, but rather, highlight all of the voxels in the spinal cord, indicating a poor fit with the DBSI model.

The normalized signal and the DBSI fit is plotted in Figure 23b and e, along with the residuals of the data and fit in Figure 23c and f. It can be observed from these figures that the DBSI model more adequately fits the data for the healthy control, consequently resulting in lower residuals for the healthy control.

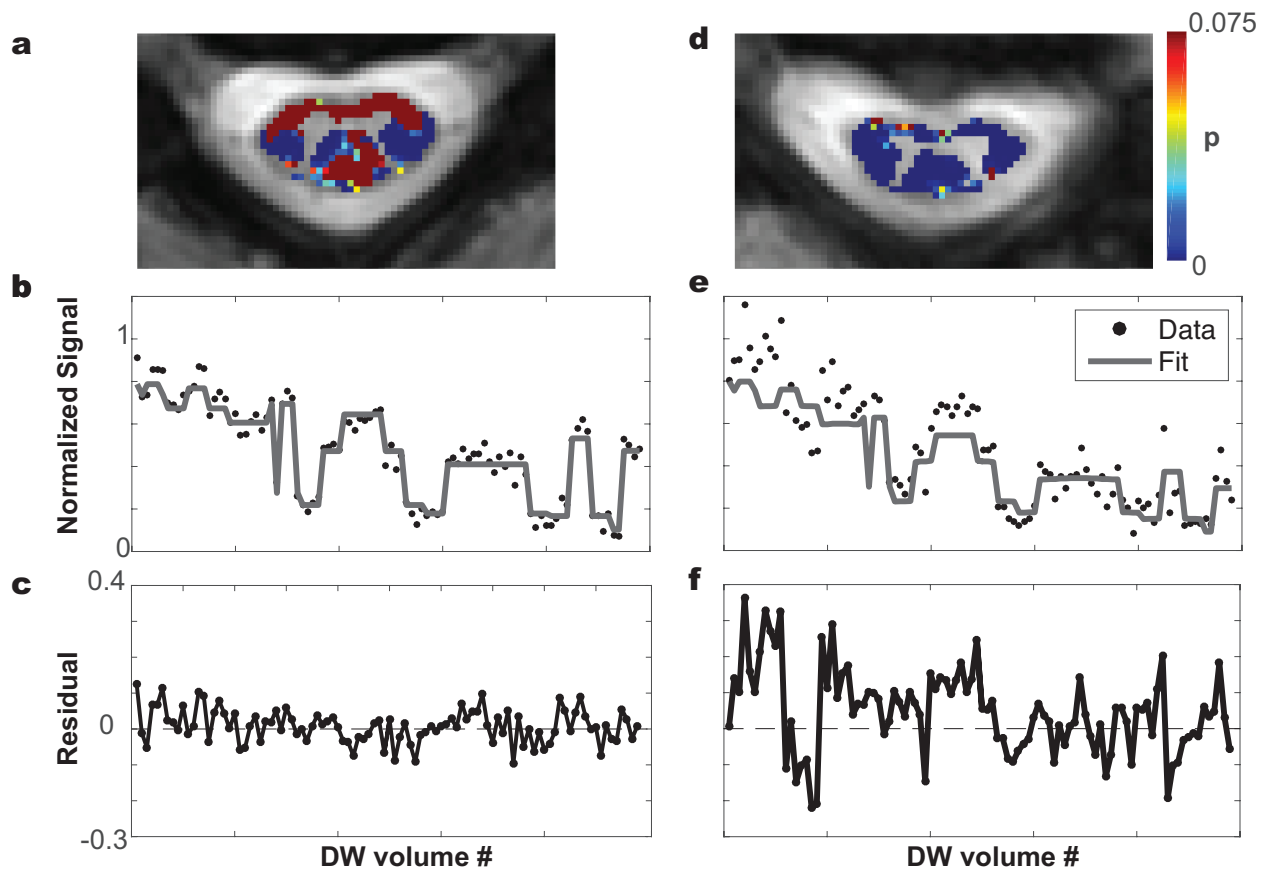


**Figure 23: Goodness-of-fit comparison for healthy control and MS patient.** Left column displays example for a healthy control, showing (a) the Chi-square goodness of fit map, (b) the normalized signal in black along with the predicted fit, and (c) a plot of the residuals. Right column shows same plots but for a MS patient (d,e,f).

## 6.4 Discussion

The goals of this study was to assess (i) the feasibility of DBSI in the human spinal cord in vivo and (ii) the sensitivity of DBSI-derived indices in the spinal cord of MS.

DBSI offers the ability to separate inflammation-associated effects arising from



vasogenic edema and increased cellularity. In MS, increased cellularity, along with the presence of axonal and myelin injury, can occur; with DTI, the representation of this process would be simplified to underestimated demyelination (RD) and overestimation of axonal injury (AD). In a more severe case of MS, axonal loss can occur, and the resulting isotropic unrestricted diffusion can overexaggerate AD and RD. Due to the possible bias in DTI measurements resulting from MS pathology, there is a need to adequately model the effects induced by inflammation and axonal loss. DBSI has demonstrated a lot of promise in several animal models including EAE mice for the spinal cord (76) and optic nerve (11), in addition to in vivo human MS applications for the brain (67,77). Recently, DBSI has been demonstrated in the spinal cord of cervical spondylotic myelopathy patients (78), however it is important to note that this protocol was limited to a b-value of  $800 \text{ s/mm}^2$ , which would be difficult to adequately probe restricted diffusion.

Our results indicate that DBSI is feasible in healthy controls, however, the model is unable to accurately characterize the underlying pathology in MS. DBSI demonstrated high reproducibility in the healthy controls, however this is a much more simplified case than the MS patients. The only validation for correct separation of isotropic restricted diffusion and isotropic non-restricted diffusion is the correct identification of gray matter and CSF respectively. The model did not seem to adequately fit the data for the MS patients, as indicated by the Chi-square goodness-of-fit tests, where all of the patient data yielded significant differences between the fit and the model. One possible reason for this lack of sensitivity to MS is the inability to separate the isotropic diffusion. This may be due to the lower SNR in spinal cord diffusion MRI, which could make it difficult to distinguish isotropic restricted diffusion ( $0 \leq \text{ADC} \leq 0.3 \text{ } \mu\text{m}^2/\text{ms}$ ) from the noise floor (138). Additionally, since the DBSI model is complex, the fitting may consequently require more SNR than the other two methods investigated in this work (NODDI and SMT). It would be worthwhile to investigate the reproducibility of the isotropic spectrum fitting, in addition to optimizing the number of uniformly discretized points in that spectrum to determine whether the model fit would be more stabilized with less points. It is also worth noting that the model does not consider the fast exchange between the restricted isotropic components due to the lack of myelin, and this could be considered in future work.

Lastly, a known degeneracy in fitting biophysical models exists (133,139), where it has been demonstrated that a signal can be fit equally as well by two different solutions using the

same model. The complexity of the DBSI model may result in several local minima, and due to the noisier DW images inherent to spinal cord imaging, it may be difficult to choose the correct set of parameters when several sets may yield low objective function values. Constraining the fit for the MS cohort may help yield results that more aligned with expected pathology; however further investigation is necessary before doing so in order to validate any assumptions. Additionally, acquiring more information, such as by varying the diffusion time, may help identify the correct solution (140).

In summary, DBSI holds promise in separating inflammation effects from other diffusion properties, which would allow for increased specificity and sensitivity of AD and RD in the presence of pathology. Currently, however, the method may be limited in its application of the spinal cord due to low SNR, however, efforts towards DBSI in the spinal cord should be continued.

## CHAPTER 7

### Comparison of Biophysical Models to DTI and DKI

#### Text adapted partially from:

By S, Xu J, Box BA, Bagnato FR, Smith SA. Application and evaluation of NODDI in the cervical spinal cord of multiple sclerosis patients. *NeuroImage: Clinical* 2017. doi: 10.1016/j.nicl.2017.05.010.

#### 7.1 Introduction

The last three chapters have investigated the implementation of biophysical models (NODDI, SMT, and DBSI) in the spinal cord of healthy controls and MS patients. NODDI, SMT, and DBSI all vary in complexity, have different assumptions, and provide different properties of the tissue microstructure. In Chapter 4, we explored the value of NODDI in the spinal cord of MS, which has the potential to provide estimates of axonal volume fractions and orientation dispersion. We observed that NODDI-derived  $v_{in}$  and ODI were significantly different in healthy controls and in patients, and the observed trends in patients were in agreement to what is known in MS. In Chapter 5, we investigated the utility of SMT, a recently developed model that addresses some of the questionable assumptions in NODDI. Similarly, however, a decrease in SMT-derived axonal fractions  $v_{ax}$  was observed in MS patients in comparison to healthy controls. Finally, in Chapter 6, the DBSI model was implemented, which could provide additional value over NODDI and SMT in that DBSI could provide measures of gliosis and vasogenic edema. While the indices were reproducible in healthy controls, the model showed no sensitivity to the MS cohort.

The goal of this chapter is to compare these biophysical models to two signal models, DTI and DKI. DTI analysis can provide another measure of credibility for the biophysical models, should the trends in both provide expected observations. With DKI, higher b-values are also used, and therefore, DKI allows us to answer the question of whether the sensitivity of the previously implemented methods arises from the use of higher b-value data or from the biophysical model itself.

## 7.2 Methods

### 7.2.1 Human Subjects

Local institutional review board approval and written informed consent were obtained prior to imaging. The same controls and patients in the NODDI (Chapter 4) and SMT (Chapter 5) were enrolled. Eight healthy controls ( $29.0 \pm 5.0$  years, 5M/3F) participated in this study; to assess reproducibility, four healthy controls were rescanned within a month. Six relapsing-remitting MS patients ( $39.3 \pm 6.1$  years, 6F) were recruited for this study. Patients' disability was rated using the Expanded Disability Status Scale (EDSS) score (22), and ranged from 0 to 6 for the patients enrolled in this study. Although some of the patients were known to have spinal cord disease from previous clinical scans, none of them was experiencing an acute exacerbation. All patients had been free from steroid administration for at least 6 months.

### 7.2.2 In Vivo Imaging

Scans were performed on a 3.0T whole body MR scanner (Philips Achieva, Best, Netherlands), using a dual channel body coil for excitation and a 16-channel SENSE neurovascular coil for reception. Again, the same exact dataset used for the NODDI and SMT study was used for this study. Two b-shells were acquired, including a  $b=711 \text{ s/mm}^2$  shell uniformly sampling 32 non-coplanar directions and a  $b=2855 \text{ s/mm}^2$  shell sampling 64 non-coplanar directions. A total of two non-diffusion-weighted scans ( $b=0 \text{ s/mm}^2$  or  $b_0$ ) were acquired, one at the beginning of each b-value shell acquisition. Total acquisition time was 18:11 min.

### 7.2.3 Image Processing

Conventional diffusion tensor analysis was performed using a nonlinear fit in Camino (104) utilizing only the 32 directions from the  $b = 711 \text{ s/mm}^2$  shell and provided FA, MD, AD and RD indices.

Additionally, using all of the same data as NODDI and SMT, DKI fitting was performed with a weighted linear least squares estimator (141) using the freely available NYU DKI toolbox (142). The resulting DKI maps included the mean kurtosis (MK), axial kurtosis (AK), and radial kurtosis (RK). For clarity, the kurtosis estimates the non-Gaussian nature of a distribution, where MK indicates the average diffusion kurtosis over all directions; AK indicates the diffusion

kurtosis along the primary axis of the kurtosis tensor and is typically low in healthy white matter tissue since the diffusion along axons is relatively unrestricted; RK indicates the diffusion kurtosis along the axis perpendicular to the primary axis of the spinal cord and is typically high in healthy tissue due to the more heterogeneous pattern in the presence of myelin sheaths (58).

### 7.2.3 Image Pre-Processing

The data was processed as described in Chapters 4 and 5, following the same pipeline for image registration and segmentation.

### 7.2.4 Statistical Analysis

Reproducibility of the DTI- and DKI-derived indices in white matter of healthy controls were assessed using Bland-Altman (105), where the mean difference, 95% confidence interval (CI) for the mean difference and the normalized Bland Altman difference ( $D_{BA}$ ) were assessed in white matter. Additionally, a nonparametric Wilcoxon signed rank was performed, in addition to the Bland Altman analysis, to determine whether a significant difference exists between the median of each diffusion-derived index for each of the two scans at  $\alpha=0.05$ .

Group comparisons between healthy controls and MS patients were performed to assess differences in DTI- and DKI-derived indices. For controls, the mean value was calculated over all white matter, which was defined using the automatically segmented ROIs as previously described; for MS patients, white matter was further manually delineated into lesion and normal appearing white matter (NAWM) from the mFFE images. For each index three non-parametric Wilcoxon rank sum tests were performed to compare (i) healthy white matter vs. lesions, (ii) healthy white matter vs. NAWM and (iii) lesions vs. NAWM at a significant threshold of  $\alpha=0.05$ .

### 7.2.5 Contrast of Derived Indices in MS Patients

Image contrast between lesions and NAWM in the MS patients was calculated for the derived maps for NODDI, SMT, DTI, and DKI, where contrast was defined as:

$$C = \frac{|\mu_{lesion} - \mu_{NAWM}|}{\frac{1}{2}(\mu_{lesion} + \mu_{NAWM})} \quad (42)$$

with  $\mu_x$  representing the mean over the specified region of interest. Note DBSI was not included in this comparison, as it was not able to provide sensitivity of MS.

### 7.2.6 Evaluation of Model Fit

Since NODDI, SMT and DKI used all of the exact diffusion data, these models can be compared directly to one another using the Bayesian Information Criterion (BIC):

$$BIC = k * \ln (n) - 2 * \ln (L^{\wedge}) \quad (43)$$

where  $L^{\wedge}$  is the likelihood of the estimated model, n is the number of data points (i.e. n=98), and k is the number of free parameters that are estimated. The log likelihood from the n measurements can be calculated as:

$$\ln(L^{\wedge}) = \sum_{i=1}^n \ln (\tilde{A}_i) - 2 \ln \sigma + \frac{A_i \tilde{A}_i}{\sigma^2} - \frac{\ln \left( \frac{2\pi A_i \tilde{A}_i}{\sigma^2} \right)}{2} - \frac{A_i^2 + \tilde{A}_i^2}{2\sigma^2} \quad (44)$$

where  $\sigma$  is the square root of the noise variance,  $\tilde{A}_i$  is the measurement and  $A_i$  is the predicted model signal (16). For NODDI, SMT, and DKI, k=5, 2, and 21, respectively. The model yielding the lowest BIC is the favored model.

## 7.3 Results

### 7.3.1 Reproducibility of DKI and DTI

Table 10 lists the reproducibility metrics for each DKI- and DTI-derived index. It is important to note that the 95% confidence intervals for the mean difference of all of the derived indices overlap 0 and the Wilcoxon sign rank p-value is greater than 0.05, indicating that the metrics are not significantly different from one another in the two different time points. Additionally, the  $D_{BA}$  for all of the indices is under 10%, indicating that that the variability between the two scans is low for DKI and DTI.

Table 10: Reproducibility metrics for DKI and DTI.

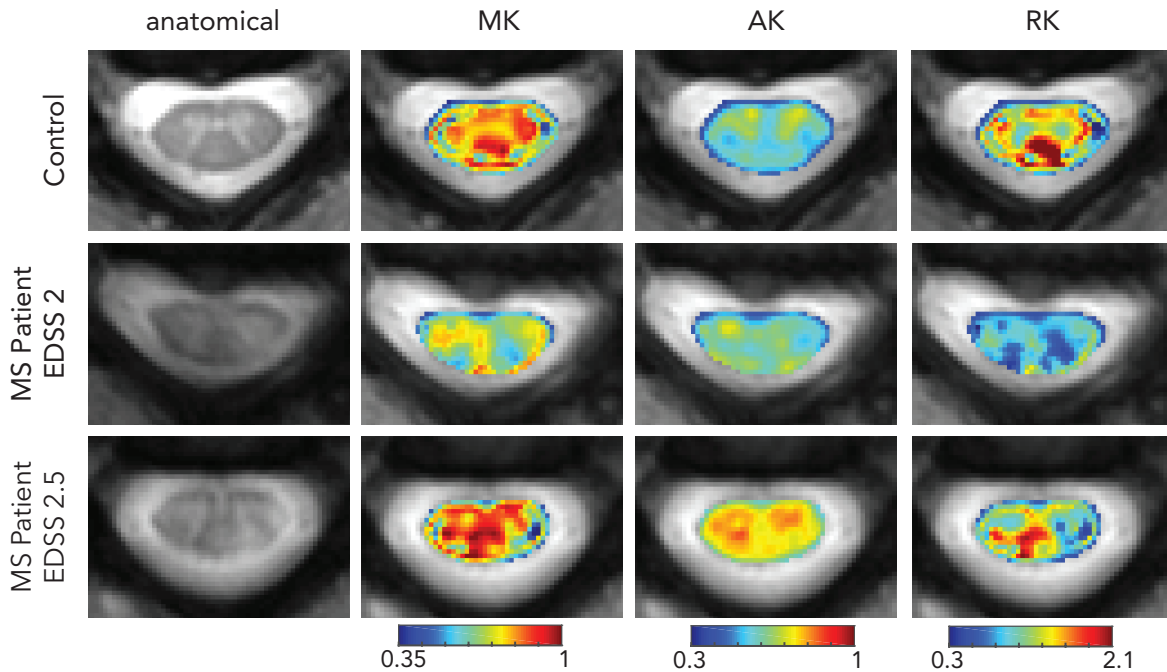
	<b>Scan 1</b>	<b>Scan 2</b>	<b>Bland-Altman</b>		<b>WSR</b>	
	<i>mean±s.d.</i>	<i>mean±s.d.</i>	<i>Difference</i>	<i>95% CI</i>	<i>D<sub>BA</sub> (%)</i>	<i>p-value</i>
<b>DKI</b>						
<i>MK</i>	0.81±0.04	0.78±0.10	0.03	[-0.13, 0.19]	3.89	1
<i>AK</i>	0.53±0.04	0.56±0.02	-0.03	[-0.10, 0.04]	5.39	0.25
<i>RK</i>	1.56±0.16	1.49±0.20	0.07	[-0.25, 0.40]	4.77	0.63
<b>DTI</b>						
<i>FA</i>	0.70±0.06	0.71±0.03	-0.01	[-0.10, 0.08]	1.34	0.88
<i>MD*</i>	1.15±0.04	1.08±0.09	0.07	[-0.01, 0.16]	6.49	0.13
<i>AD*</i>	2.28±0.21	2.15±0.14	0.13	[-0.01, 0.27]	5.81	0.13
<i>RD*</i>	0.58±0.06	0.54±0.07	0.04	[-0.11, 0.19]	7.81	0.38

\*units of  $\mu\text{m}^2/\text{ms}$

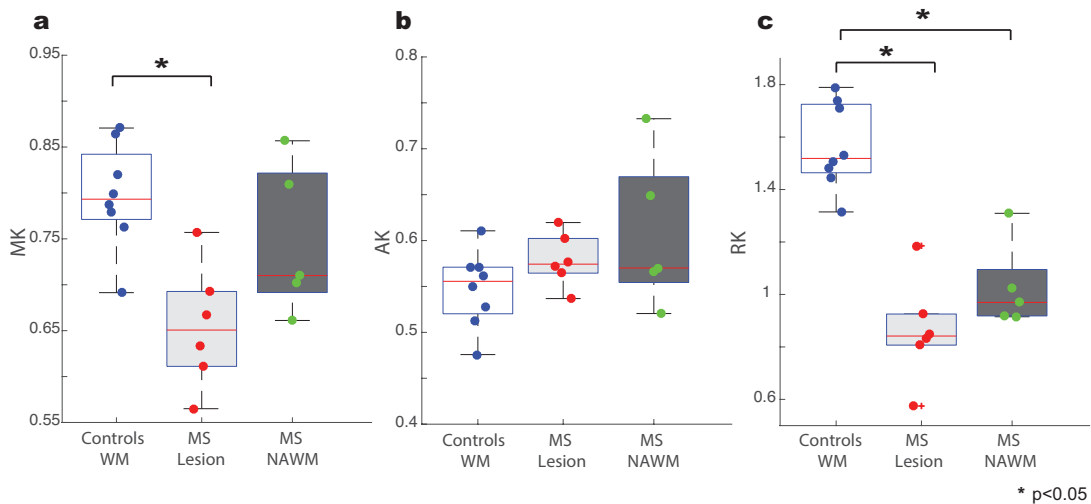
### 7.3.2 Application of DKI in MS

Figure 24 shows the derived DKI images from the same control and MS patients as in Chapters 4 (Figure 14), 5 (Figure 18) and 6 (Figure 21). In the healthy control, the contrast between white matter and gray matter is low in both the MK (mean image contrast=0.02) and RK (mean image contrast=0.11) maps, as there are areas of inconsistent estimation in the white matter, particularly in the dorsal and lateral columns. There is, however, a noticeable decrease in MK and RK at the site of the lesions. For MS patient 1 (middle row), a larger decrease in MK and RK is observed in other areas outside the lesion.

Group comparisons for the DKI-derived metrics are shown in Figure 25. A decrease in MK in the lesions of MS patients is detected ( $p=0.003$ ). No significant differences were observed between healthy white matter and MS white matter for AK. For RK, a significant decrease was observed between healthy white matter and lesions in MS patients ( $p<0.001$ ). Additionally, a decrease was observed between healthy white matter and NAWM in MS patients ( $p=0.016$ ), albeit to a lesser degree than what was observed in lesions.



**Figure 24: Example images from DKI.** Representative control is shown in the first row, followed by examples from two MS patients. From left to right, the anatomical, MK, AK and RK are shown.



**Figure 25: Comparison of MK, AK and RK.** Boxplots highlighting the median, 25<sup>th</sup> and 75<sup>th</sup> percentiles over controls (WM) and MS patients (lesions and NAWM) for (a) MK, (b) AK and (c) RK. Mean values from each subject plotted and asterisks indicate significant differences between the groups. Kurtosis metrics are unitless.



### 7.3.3 Application of DTI in MS

Figure 26 shows the FA, MD, AD and RD maps for the same control and MS patients as shown in Figure 24. The healthy control provides maps with expected features. For FA, there are higher values in white matter than in gray matter (FA contrast=1.40). For MD, the contrast is low between gray and white matter and the values are around  $1 \mu\text{m}^2/\text{ms}$ . For AD, the white matter has very high diffusivity in the direction parallel to the fibers, whereas much lower diffusivity values perpendicular to the fibers can be observe in the RD maps. In the MS patients, the most noticeable changes are observed in the FA and RD maps, but it is still difficult to delineate the lesions from NAWM in patient 1 (FA contrast=0.024, RD contrast=0.130) and patient 2 (FA contrast=0.070, RD contrast=0.090). There is a slight decrease in AD in the MS

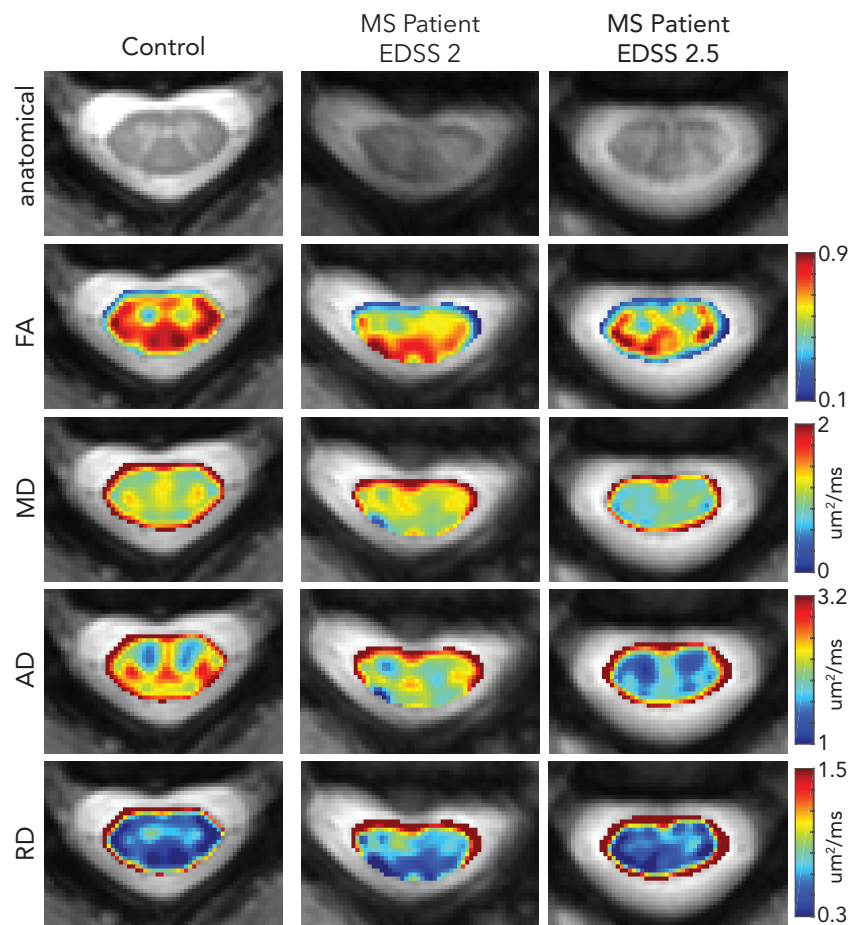


**Figure 26: Example images from DTI.** Representative control is shown in the first row, followed by examples from two MS patients. From left to right, the anatomical, FA and RD are shown.

patients, however no significant change can be observed in the MD maps.

Figure 27 displays the boxplots for each DTI-derived index, highlighting the median and interquartile range for DTI-derived indices over all volunteers.

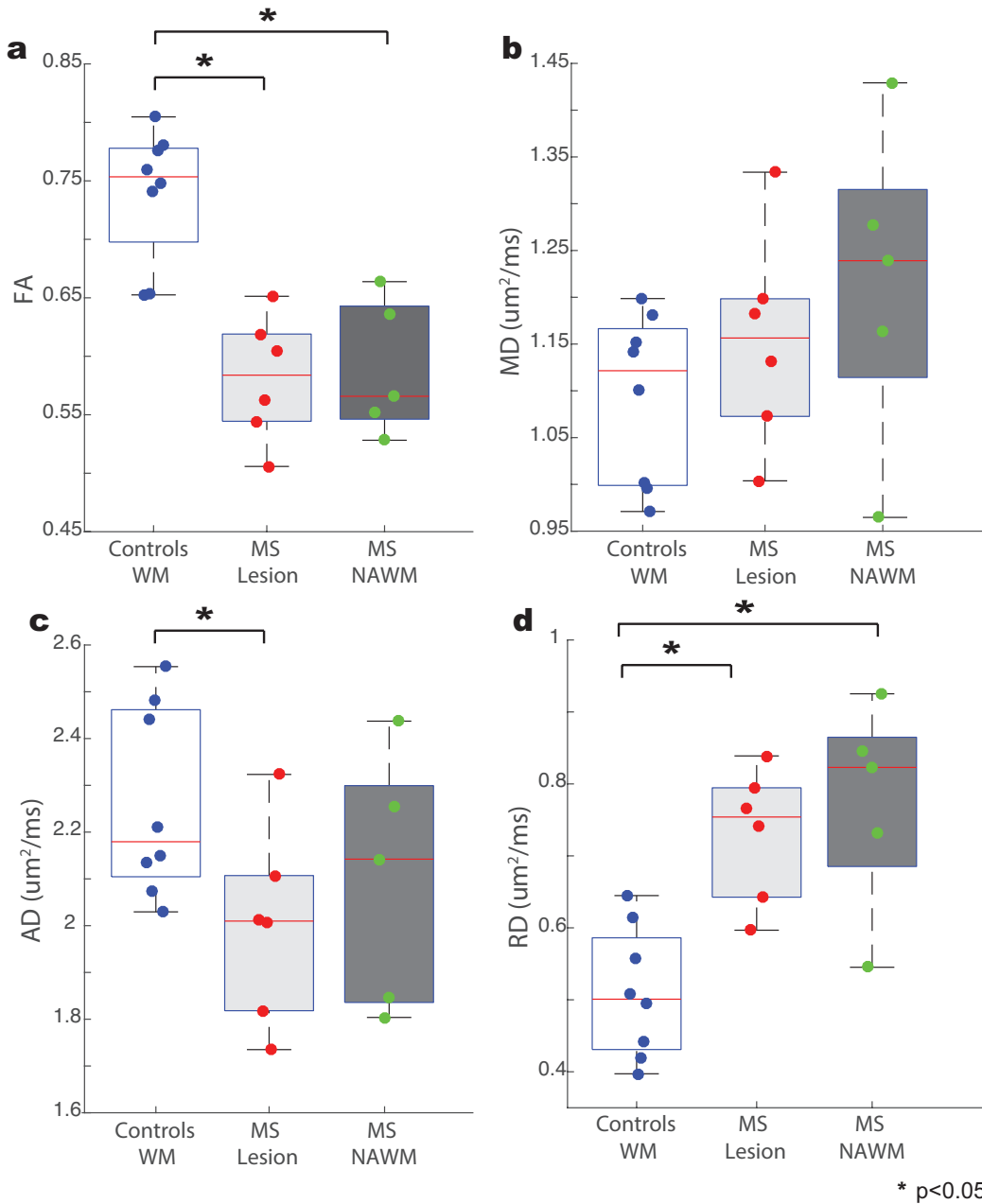


**Figure 27: Comparison of FA, MD, AD and RD.** Boxplots highlighting the median, 25<sup>th</sup> and 75<sup>th</sup> percentiles over controls (WM) and MS patients (lesions and NAWM) for (a) FA, (b) MD, (c) AD, and (d) RD. Mean values from each subject plotted and asterisks indicate significant differences between the groups.

FA (Figure 27a) is reduced in both lesions (mean=0.58±0.05, p<0.001) and NAWM (mean=0.59±0.06, p<0.01). No significant differences are detected for MD (Figure 27b), however there is a trend towards an increased MD. There is a significant decrease in AD (healthy=2.26±0.20, lesion=2.01±0.17μm<sup>2</sup>/ms, p=0.03), and lastly, differences in RD were also seen (Figure 27d) in both lesions (mean=0.73±0.10, p=0.005) and NAWM (mean 0.77±0.15 μm<sup>2</sup>/ms p=0.01).

### 7.3.3 Comparison of Contrast

Figure 28 compares the mean contrast, along with the standard deviation, between lesion and NAWM over all of the patients for the indices that provided the ability to distinguish disparity between healthy controls (i.e., NODDI-derived  $v_{in}$  and ODI, SMT-derived  $v_{ax}$ , DKI-derived MK and RK, and DTI-derived FA, AD and RD). It is apparent that the biophysical models NODDI and SMT provide higher contrast between NAWM and lesions than both signal models DKI and DTI. DKI-derived MK provides reasonable contrast, however the inter-subject variability is large.

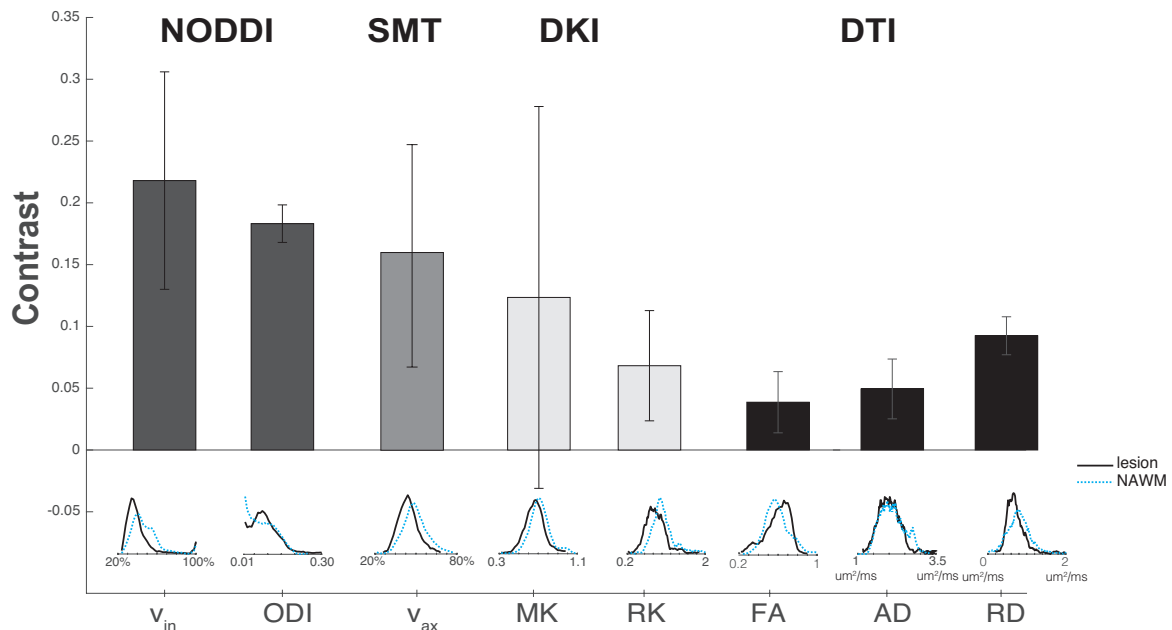


**Figure 28: Contrast in diffusion maps.** Mean contrast between lesions and NAWM over all patients is shown, with error bars indicating the standard deviation over all of the patients. Histograms of all the voxels over each patient are shown for lesions (black) and NAWM (dashed blue), where large overlap between the two would indicate low contrast.

Below the bar plot, a histogram of all the voxels delineating lesions (black) and NAWM (dashed blue) over all patients is shown. In all cases, the contrast between lesion and NAWM from the NODDI indices, either  $v_{in}$  ( $0.20 \pm 0.08$ ) or ODI ( $0.15 \pm 0.02$ ), and SMT's  $v_{ax}$  ( $0.16 \pm 0.09$ ) was greater than any of the DKI (MK:  $0.13 \pm 0.15$ , RK:  $0.07 \pm 0.05$ ) or DTI indices (FA:  $0.04 \pm 0.02$ , AD:  $0.05 \pm 0.02$  RD:  $0.10 \pm 0.02$ ). Furthermore, the histograms demonstrate that the distributions of the lesion and NAWM voxels mostly overlap one another for the DKI and DTI indices, whereas the histograms of the NODDI indices indicate greater deviation from one another. In particular, the  $v_{in}$  histogram for the NAWM highlights a bump to the right of the lesion histogram, indicating a large frequency of increased  $v_{in}$  values in the NAWM. With ODI, a global increase throughout the cord was observed, so there is overlap in the histograms for NAWM and lesion voxels, but a more distinct peak is seen in the lesion histogram.

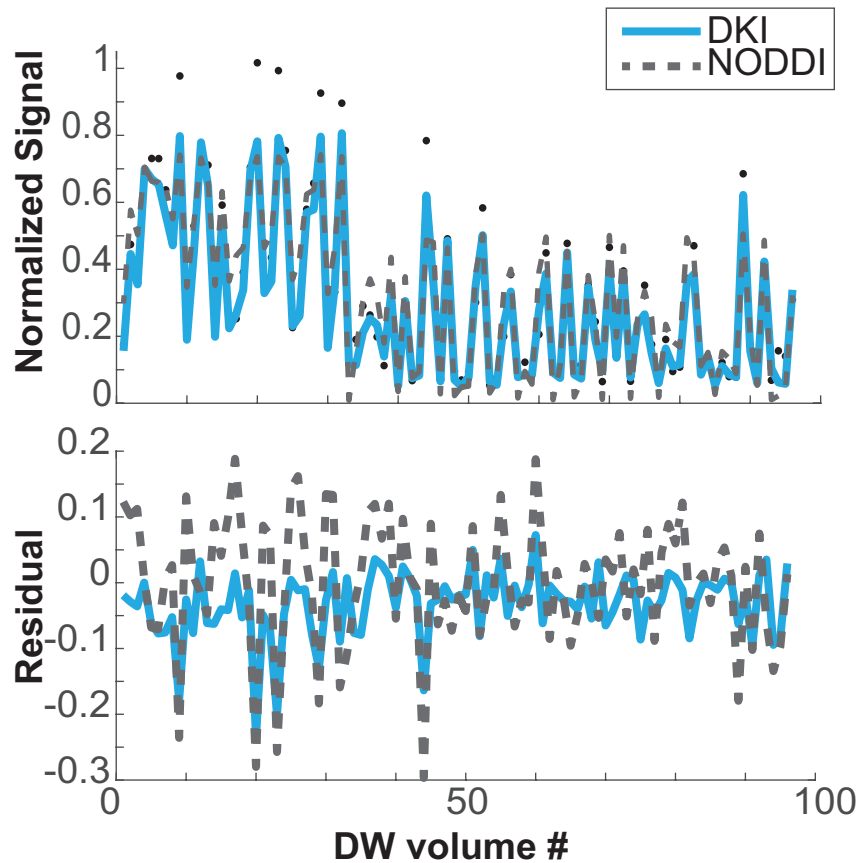
### 7.3.4 Evaluation of BIC

Table 11 lists the mean BIC for the NODDI, SMT, and DKI fittings over all white matter voxels. Both healthy controls and MS patient data are listed, where the lowest BIC is favored.

Table 11: BIC of NODDI, SMT and DKI.

	<b>NODDI</b>	<b>SMT</b>	<b>DKI</b>
C1	2.89E+05	879.8	1.48E+05
C2	1.49E+04	10.3	5.32E+03
C3	4.30E+07	2.17E+04	1.93E+07
C4	1.25E+04	0.57	3.30E+03
C5	6.29E+06	830.85	3.40E+06
C6	7.33E+04	0.89	3.03E+04
C7	1.61E+04	-1.11	6.37E+03
C8	2.26E+07	1.18E+03	1.13E+07
MS1	9.17E+05	320.66	4.41E+05
MS2	5.02E+06	435.93	2.98E+06
MS3	8.49E+02	2.14	2.93E+02
MS4	7.92E+06	2.63E+03	4.94E+06
MS5	1.16E+07	2.20E+03	4.66E+06
MS6	5.78E+06	2.57E+03	2.43E+06

The trends are consistent throughout all of the controls and MS patients. SMT yields the lowest BIC, followed by DKI, and then NODDI. Though not shown, the DTI fitting using both b-value shells resulted in the highest BIC overall. Figure 29 shows an example DKI and NODDI fit for a white matter voxel, highlighting the larger residuals in the NODDI fit in comparison to DKI.



**Figure 29: Comparison of NODDI and DKI fit.** Top figure plots the normalized signal in a white matter voxel, with DKI fit in blue and NODDI fit in dashed gray. Bottom figure plots the residuals for both models.

## 7.4 Discussion

Without histology, it is difficult to truly validate the biophysical models and determine whether the derived measurements are closer to the ground truth than DTI and DKI. However, this study identifies which models are capable in vivo of providing reliable (in terms of reproducibility of healthy controls and evaluation of fit with BIC) information, while providing

unique contrasts to characterize MS, consistent to what is known about the underlying pathology of the disease. Rather than focusing on the accuracy of these models, the use of only clinical diffusion data consequently focuses on the precision of these models.

Here, we show that DKI and DTI analysis on the same data do provide high reproducibility, along with the ability to detect disparity between healthy controls and MS patients. A key advantage with the biophysical models is the potential to disentangle multiple effects from the diffusion signal and obtain more specific information regarding tissue microstructure, which may attribute to the increased contrast observed in the indices derived from the biophysical models (NODDI and SMT) over the indices derived by the signal models (DTI and DKI). NODDI and SMT showed more disparity between lesions and NAWM, whereas with DTI-derived FA and RD, the changes are global, resulting in a decrease in contrast. The global change in FA and RD is consistent with previous findings that point to improved quality of fit with NODDI versus DTI (75) and we hypothesize this is due to the non-specificity of the tensor model. It is important to note, however, that only the  $b=711$  s/mm<sup>2</sup> shell was used in the DTI tensor calculation since at higher b-values, the signal is more sensitive to slow diffusing time components, and it is well known that the diffusion signal no longer follows a Gaussian approximation (50). With DKI, both b-value shells are used to fit the model since the model can account for the non-Gaussianity in the diffusion weighted signal. The contrast in DKI-derived MK is higher than DTI, however there is large inter-subject variability in the contrast for MK. This may be due to the fact that more parameters are required in the fit for DKI in comparison to NODDI and SMT, and the simpler models (i.e. less parameters to fit for) will provide smoother maps (72).

Since the DTI model did not use all of the data in the NODDI and SMT acquisition, the comparison was not scan time equivalent. Previous work has demonstrated that the underlying measurement error in the DTI-derived indices in the spinal cord is negligible when increasing the number of averages from one to two for a 32-direction scheme (143). Therefore, we do not expect different conclusions in our DTI analysis, if we instead were to use a scan time equivalent comparison for DTI. However, we also chose to compare the biophysical models with the DKI model in order to have a comparison using all of the same data. This comparison has never been made for in vivo spinal cord imaging, but answers a relevant question of whether multi-compartmental and biophysically based models are indeed more sensitive than conventional

single compartment models, or whether the source of sensitivity arises from acquiring multiple b-shells. Interestingly, a significant change was observed in MK at the site of the lesion, whereas no change was detected with MD. This may indicate DKI's ability to overcome some of the limitations of DTI. To compare the differences between DKI and the biophysical models, we referred to our BIC analysis. Here, the results favored SMT, followed by DKI and then NODDI. It is important to note, however, that the comparison with SMT may be biased, as the likelihood calculation only takes into consideration two points (the mean over all gradient directions for a given b-value), whereas DKI and NODDI examine the fit over all 98 points. To this end, though the original data is the same, it is expected that the variations in two points for SMT is much smaller. However, it is fair to compare DKI and NODDI directly, in which case the BIC analysis favors DKI. This may be attributed to the fact that the complexity of the NODDI model requires several assumptions. Although these assumptions are able to provide reasonable biophysical parameters, too many assumptions may restrict the model from capturing all of the effects observed in the signal. Therefore, future work is still necessary to improve on these biophysical models.

SMT and NODDI both provide estimates of axonal volume fractions, however the implemented assumptions in the models are different. In particular, NODDI's assumptions of fixed intrinsic diffusivity and modeling of orientation dispersion using only a single distribution have been questioned (139). The high similarity in estimates from both models may indicate that for in vivo implementation of NODDI in the spinal cord, the assumptions are reasonable. The spinal cord provides a more ideal environment for assessment of these diffusion models than the brain, as the fibers are primarily aligned along one axis. Furthermore, the orientation dispersion is very low and crossing fibers are not as present as they are in the brain. However, with SMT, a trend towards decreased intrinsic diffusivity was observed, and it would be worthwhile to investigate both methods in patients with more progressive disease to determine whether or not the intrinsic diffusivity will bias the axonal fractions derived by NODDI and SMT.

A limitation in this work is that the implemented protocol was optimized for NODDI (10) and not SMT. Less variability in the SMT-derived indices may be observed when using schemes with less gradient directions in each b-value shell, but with more b-value shells (68). Therefore, optimization of the SMT protocol in terms of number of b-value shells and number of gradient directions in each shell should be investigated for future studies. Lastly, it would be interesting to

implement the white matter tract integrity (WMTI) model, using the kurtosis information, to extract biophysical parameters (66).



## CHAPTER 8

### Towards Clinical Applicability: Reducing Scan Times and Increasing Coverage of Multi-Shell Diffusion Protocols

#### 8.1 Introduction

Up to now, the biophysical models have been implemented in order to maximize SNR in one slice, and therefore resulted in a long acquisition time and limited coverage. To move NODDI and SMT towards clinical adoption, it is important to consider the scan time and potential coverage for the overall utility of these techniques. To this end, this chapter investigates the optimization of these techniques using a two-pronged approach. First, to decrease scan time, the effect of reduced acquisition schemes (i.e. fewer gradient directions sampled) on the derived indices will be investigated. Second, to increase coverage, a multi-slice acquisition can be used given the long repetition times implemented; furthermore, the use of multiband will be investigated in order to provide additional coverage.

Multiband strategies enable excitation and acquisition of multiple slices simultaneously (144-146), and would be well suited for speeding up acquisition of or increasing coverage in diffusion sequences (119). Theoretically, a multiband composite RF, comprised of  $n$  sinc pulses with different frequency offsets, can be used to acquire multiple slices simultaneously without sacrificing in-plane resolution in the slice direction. The RF receive coil array then provides the spatial encoding to separate the simultaneously acquired slices (147). While there is no intrinsic penalty on SNR due to the reduction factor  $R$ , as in SENSE, the SNR of the multiband SENSE acquisition is dependent on the  $g$ -factor of the coil setup (i.e. there must be sufficient coil sensitivity along the slice direction). Additionally, RF phase cycling is generally employed to make unfolding images easier, where a phase shift is applied between slices during the simultaneous excitation. For single-shot EPI sequences, since a single excitation pulse is used, RF phase cycling is not useful. Individual slices can be shifted in-plane through implementation of linear phase modulations over  $k$ -space blips in the slice direction, which shifts the coil sensitivities and makes the aliased pixels easier to unfold (131). Generally in brain diffusion MRI, full brain coverage is feasible, and multiband is used to accelerate the scan time by acquiring more slices per TR. However, our spinal cord diffusion sequence is limited by the

cardiac cycle, so the primary benefit in using a multiband acquisition is to gain more volume coverage.

## 8.2 Methods

### 8.2.1 Influence of Acquisition Schemes on NODDI and SMT Accuracy

The dependency of the accuracy of NODDI- and SMT-derived indices on number of gradient directions was investigated by subsampling the fully acquired dataset (see Sections 4.2 and 5.2). The fully-acquired gradient direction scheme (32 directions at  $b=711$  s/mm<sup>2</sup>, 64 directions at  $b=2855$  s/mm<sup>2</sup>) was ordered using Camino’s orderpoints function (148), which orders the directions by minimizing the electrostatic energy of the subsampled sets. Three subsampled schemes were analyzed: (i) ‘acq\_2/3’, where 2/3 of the acquired data was used (12 min), consisting of 32 directions in the  $b=711$  s/mm<sup>2</sup> shell and 32 directions in the  $b=2855$  s/mm<sup>2</sup>, (ii) ‘acq\_1/2’, where 1/2 of the acquired data was used (9 min), consisting of 16 directions in the  $b=711$  s/mm<sup>2</sup> shell and 32 directions in the  $b=2855$  s/mm<sup>2</sup>, and (iii) ‘acq\_1/3’, where 1/3 of the acquired data was used (6 min), consisting of 16 directions in the  $b=711$  s/mm<sup>2</sup> shell and 16 directions in the  $b=2855$  s/mm<sup>2</sup>. Table 12 summarizes the number of directions in each subsampled scheme.

Table 12: Summary of Reduced Acquisition Schemes.

	Lower b-shell (711 s/mm <sup>2</sup> )	Upper b-shell (2855 s/mm <sup>2</sup> )	Total Number of Directions
acq 2/3	32	32	64
acq 1/2	16	32	48
acq 1/3	16	16	32

In controls, the root mean squared error (RMSE) was calculated over white matter using the full acquisition as the gold standard. For RMSE, accuracy was quantified as the bias, or the difference from the gold standard; precision was calculated as the standard deviation of the difference between the chosen scheme’s derived maps and the gold standard (94,95). RMSE units are expressed in the same units as the estimator it is quantifying. In patients, the sensitivity

to lesion presence and conspicuity between lesion and NAWM was observed for each data reduction scheme.

### 8.2.2 Implementation of Reduced Acquisition Schemes with Multi-Slice Imaging

Local institutional review board approval and written informed consent were obtained prior to imaging. Three healthy controls (32.0±5.51 years, 1M/2F) participated in this study. For the rest of this chapter, all scans were performed on a 3.0T whole body MR scanner (Philips Ingenia, Best, Netherlands), using a dual channel body coil for excitation and a 52-channel dStream head/spine coil for reception. The half scheme (same as ‘acq\_1/2’ above, herein also referred to as ‘Half Acquisition’) was implemented, where two b-shells were acquired, including a b=711 s/mm<sup>2</sup> shell uniformly sampling 16 non-coplanar directions and a b=2855 s/mm<sup>2</sup> shell sampling 32 non-coplanar directions. A total of two non-diffusion-weighted scans (b=0 s/mm<sup>2</sup> or b<sub>0</sub>) were acquired, one at the beginning of each b-value shell acquisition. Other relevant parameters include: slices=3, TR=4 beats. All other acquisition parameters were unchanged from the protocol previously described in Chapters 4 and 5. Total acquisition time was 11:53 min. Additionally, an anatomical image (mFFE) was acquired for image registration and segmentation. For comparison, the full acquisition was also acquired to evaluate the RMSE in the same scan session.

### 8.2.3 Implementation of Reduced Acquisition Schemes with Multiband Imaging

Increased coverage was further tested through the use of multiband imaging. First, the feasibility of multiband imaging was tested on a phantom. The phantom consisted of a test tube filled with water, submerged in a tub of water to ensure sufficient coil loading. Imaging consisted of the half acquisition as described in the previous section (Section 8.2.2), but with the following relevant parameters changed: SENSE=1, multiband factor (MB factor)=2, slices=6. To assess the effect of slice gap, the scan was repeated with a slice gap of 0, 2, 5, 10 and 20 mm. A dynamic noise scan was acquired, such that SNR could be characterized as:

$$SNR = \frac{1/2 (mean(S(r, k1) + S(r, k2)))}{1/\sqrt{2} (stdev(S(r, k1) - S(r, k2)))} \quad (45)$$

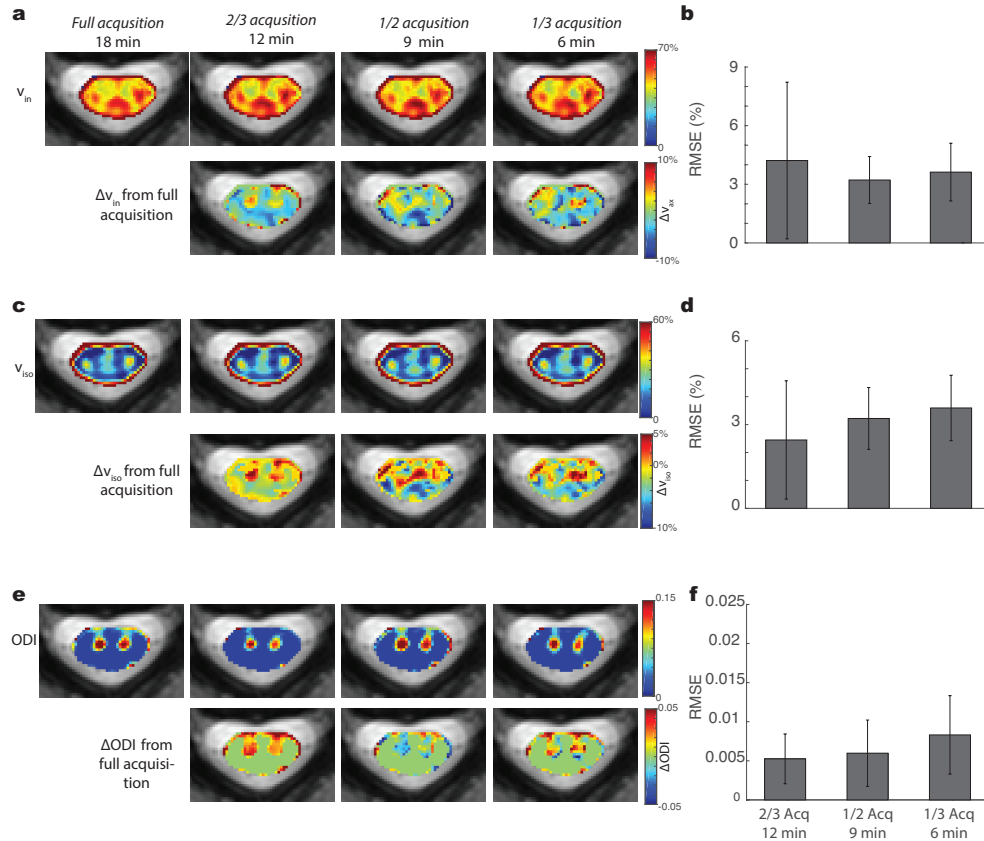
where  $S(r, ki)$  is the signal of the  $i$ -th image for the  $r$  position in a given ROI. In vivo imaging was performed in the same scan session as described in the previous section (Section 8.2.2) for all of the same healthy controls. SNR of non-diffusion-weighted images were acquired. The multiband sequence (herein referred to as “Multiband”) consisted of: TE=73 ms, TR=4 beats, FOV=68x51x85 mm<sup>3</sup>, resolution=1.25x1.25x10 mm<sup>3</sup>, slice gap=5 mm, slices=6, MB factor=2, SENSE=1, NSA=3. Total acquisition time as 10:13 minutes. An additional mFFE with the same coverage as the multiband sequence was acquired.

For comparison, a multi-slice imaging acquisition (herein referred to as “Multi-Slice”) with no multiband was acquired. In order to provide a fair comparison, scan times were kept as close to one another as possible. The multi-slice acquisition consisted of the following parameters: NSA=2, TR=6 beats, TE=65 ms, FOV=68x48x50 mm<sup>3</sup>, resolution=1.25x1.25x10 mm<sup>3</sup>, slices=5, SENSE=1.5. Total acquisition time was 11:47 minutes. For evaluation metrics, RMSE from the gold standard was calculated for the SMT- and NODDI-derived indices for the multiband and multi-slice acquisition. Second, the variability between slices was assessed by taking the mean index over all of white matter in each slice, and then taking the standard deviation across slices.

## 8.3 Results

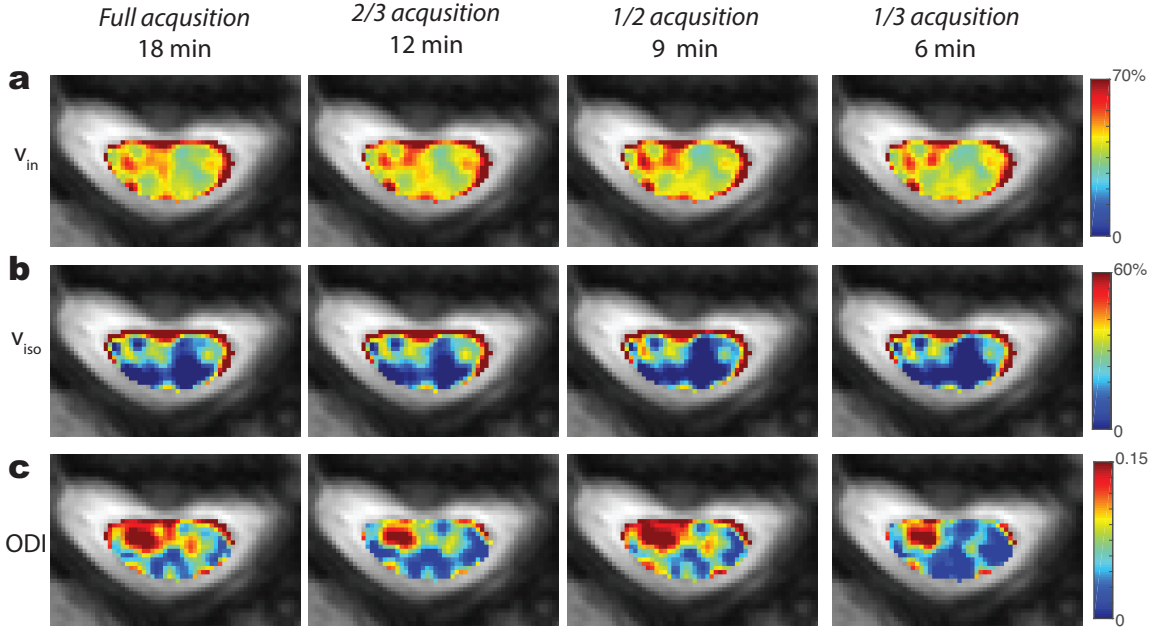
### 8.3.1 Influence of Acquisition Schemes on NODDI

Figure 30 demonstrates the effect of reduced acquisition schemes on NODDI parameters, showing the full acquisition, 2/3 acquisition, 1/2 acquisition, and 1/3 acquisition from left to right. It is important to note that the data was extracted from the full acquisition set; therefore the impact of gradient direction scheme was evaluated, not the dependency of SNR. For the different gradient acquisition schemes, the change in RMSE in  $v_{in}$  is negligible (Figure 30b), with a mean RMSE of  $3.17 \pm 2.13\%$ ,  $2.37 \pm 0.79\%$ , and  $3.35 \pm 1.27\%$  for the 2/3, 1/2, and 1/3 acquisition respectively. For all schemes, the percent error in estimated  $v_{in}$  remains under 4%. With  $v_{iso}$  (Figure 30c) and ODI (Figure 30e), the RMSE increases with less gradient directions sampled (Figure 30d and f). With the half scheme, the percent error still remains under 10% for all indices, yielding a percent error of 1.70, 6.52 and 8.01% for  $v_{in}$ ,  $v_{iso}$ , and ODI respectively.



**Figure 30: Effect of reduced acquisition schemes on NODDI-derived parameters.** (a)  $v_{in}$  maps for a healthy control for full 18 min acquisition (left), along with reduced schemes of 12 minutes, 9 minutes and 6 minutes (right). Bias maps are shown below each subsampled scheme, demonstrating an increased bias in  $v_{in}$  with reduced acquisition times, but with fairly negligible differences between all acquisitions. (b) Mean RMSE for  $v_{in}$  in white matter over all of the controls, with error bars plotting the inter-subject variability. (c)  $v_{iso}$  maps, with bias maps below, for same reduced acquisition times as shown in (a). (d) RMSE of  $v_{iso}$  increases with reduced acquisition. (e) ODI maps, with bias maps below, for same reduced acquisition times as shown in (a and c). (f) RMSE of ODI increases with reduced acquisition.

Figure 31 shows the effect of the reduced acquisition schemes on a MS patient for  $v_{in}$  (Figure 31a),  $v_{iso}$  (Figure 31b), and ODI (Figure 31c). Despite significant decreases in scan time, the observed features from the maps derived from the full acquisition scheme are still evident in the maps derived from the subsampled acquisition schemes. The most noticeable differences are in the ODI maps, where reducing the acquisition scheme to 1/3 of the full scheme loses some of the ability to estimate high ODI values (observed in full acquisition scheme) in the dorsal column of the white matter and left ventral horn of the gray matter.



**Figure 31: Effect of reduced acquisition schemes on NODDI in MS patient.** From left to right, the NODDI-derived (a)  $v_{in}$  map, (b)  $v_{iso}$  map and (c) ODI map are shown with the fully acquired dataset, 2/3 acquisition, 1/2 acquisition, and 1/3 acquisition. With decreases in acquisition schemes, and consequently scan times, NODDI does not lose sensitivity to distinguish lesions from NAWM.

### 8.3.2 Influence of Acquisition Schemes on SMT Accuracy

Figure 32 highlights the effect of reduced acquisition schemes on the SMT-derived indices,  $v_{ax}$  (Figure 32a and b) and  $D_{ax}$  (Figure 32c and d). From left to right, the derived map is shown, as calculated from a full dataset acquired, 2/3 acquired – ‘*acq\_2/3*’, 1/2 acquired – ‘*acq\_1/2*’, and 1/3 acquired dataset – ‘*acq\_1/3*’; the bias maps from the fully acquired (assumed to be the gold standard) are shown below each scheme. With reduced data for the SMT fitting, there is an overestimation in  $v_{ax}$ , as indicated by the negative  $\Delta v_{ax}$  values (blue). For *acq\_2/3*, the bias is only evident in the left dorsal column, but extends into more white matter areas for the *acq\_1/3*. The RMSE for  $v_{ax}$  (Figure 32b), however, is low for the *acq\_2/3* (mean RMSE =  $2.70 \pm 1.55\%$ ) and *acq\_1/2* acquisitions (mean RMSE =  $2.55 \pm 0.72\%$ ); additionally, the mean percent error over all controls for white matter  $v_{ax}$  is 3.06% and 2.12% for the *acq\_2/3* and *acq\_1/2* acquisitions respectively, indicating that the difference between the two reduced schemes is negligible. With *acq\_1/3*, the mean RMSE increases to 5.52%, with an increased mean percent error for averaged white matter  $v_{ax}$  of 7.13%. For  $D_{ax}$ , similar trends are observed, but RMSE

(Figure 32d) increases with reduced acquisition, yielding a mean RMSE, with respect to the fully acquired dataset, of 0.11, 0.13, and 0.21  $\mu\text{m}^2/\text{ms}$  for the *acq\_2/3*, *acq\_1/2*, and *acq\_1/3* datasets respectively.

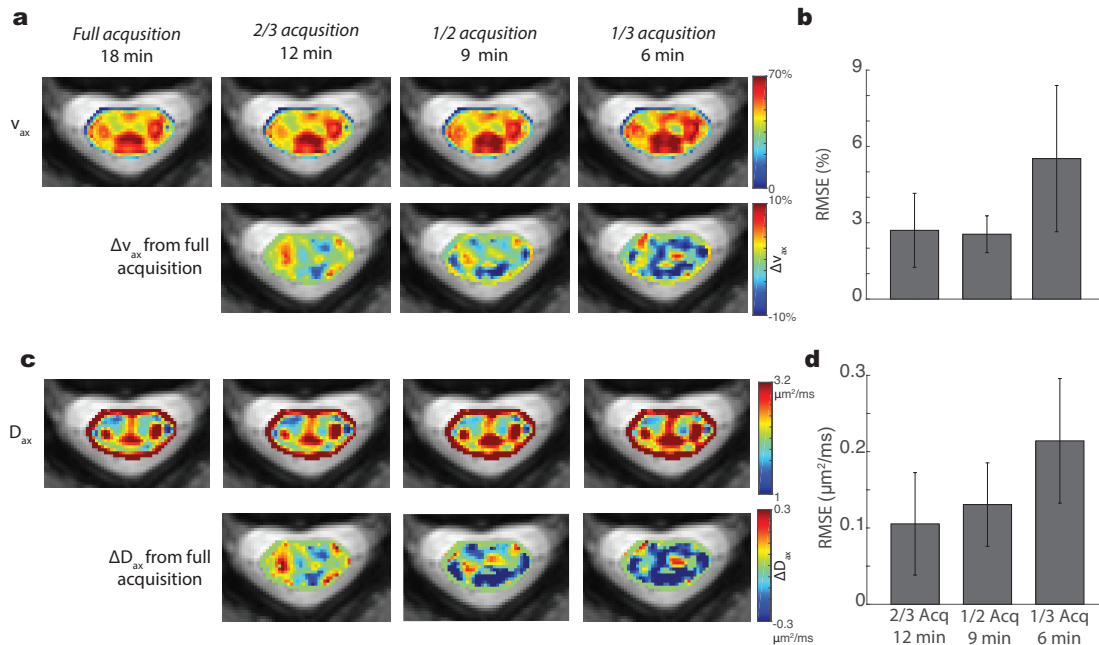


**Figure 32: Effect of reduced acquisition schemes on SMT-derived parameters.** (a) Corresponding  $v_{ax}$  maps for a healthy control for full 18 min acquisition (left), along with reduced data acquisition schemes of 12 minutes, 9 minutes and 6 minutes (right). Bias maps, with respect to full acquisition schemes, are shown below each subsampled scheme and demonstrate that there is an increased bias in  $v_{ax}$  with reduced acquisition times, but with fairly negligible differences between the 2/3 and 1/2 acquisition. (b) Mean root mean squared error (RMSE) for  $v_{ax}$  in white matter over all of the controls, with error bars plotting the inter-subject variability. (c)  $D_{ax}$  maps, with bias maps below, for same reduced acquisition times as shown in (a). (d) RMSE of  $D_{ax}$  increases with reduced acquisition.

Lastly, Figure 33 implements the reduced acquisition schemes for  $v_{ax}$  (Figure 33a) and  $D_{ax}$  (Figure 33b), in the same MS patient (patient 1) as in Figure 31. It is important to highlight that the reduced acquisition schemes do not lose sensitivity in separating lesions from NAWM, indicating that the total scan time for SMT acquisition can be reduced by 50% in the current study while keeping reasonable estimation of tissue properties.

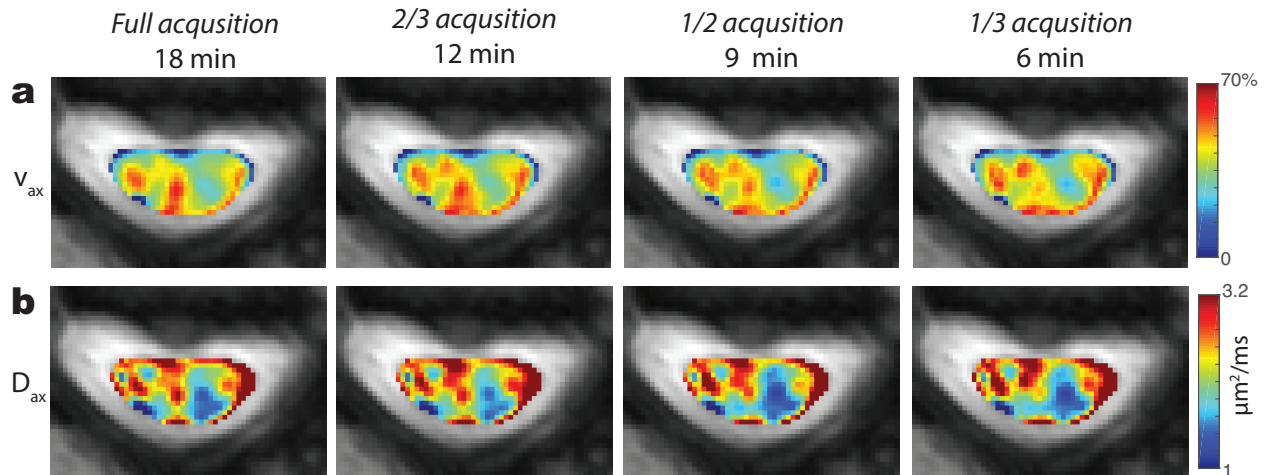


**Figure 33: Effect of reduced acquisition schemes on SMT in MS patient.** From left to right, the SMT-derived (a)  $v_{ax}$  map and (b)  $D_{ax}$  map are shown with the fully acquired dataset, 2/3 acquisition, 1/2 acquisition, and 1/3 acquisition. With decreases in acquisition time, SMT does not lose sensitivity to distinguish lesions from NAWM.

### 8.3.3 Increasing Coverage

Increasing coverage was tested two ways: 1) multiband and 2) multi-slice imaging. Figure 34 highlights the dependency of SNR and slice gap (slice gap = 0, 2, 5, 10, 20 mm) when using multiband factors of 2 in a phantom.

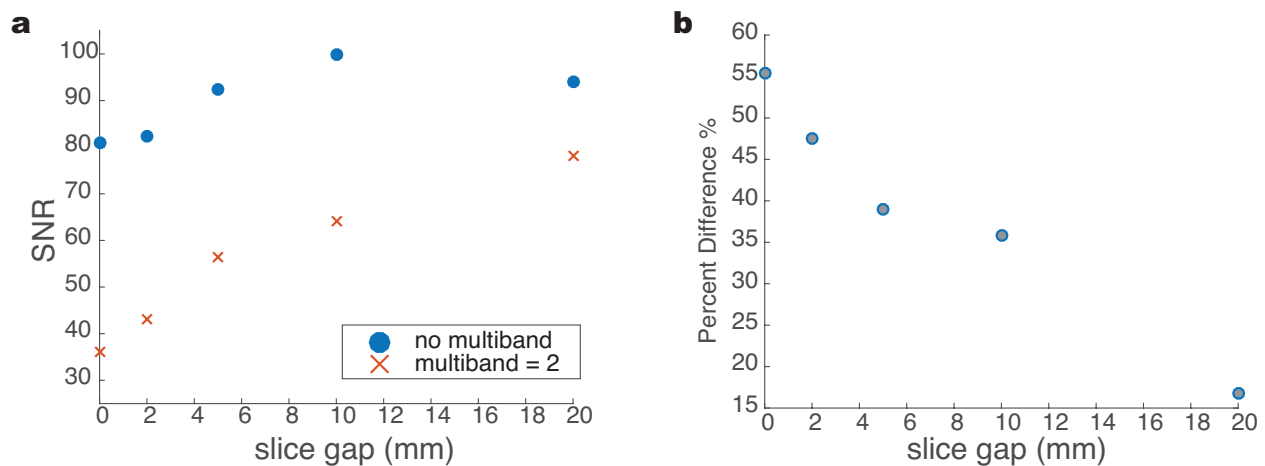


**Figure 34: SNR dependency with slice gap.** (a) With increasing slice gap, there is an increase in SNR. With multiband (red x), the dependency is greater than with no multiband (blue circles). (b) The percent difference in SNR between no multiband and multiband is plotted against slice gap. With increasing slice gaps, the percent difference decreases significantly.



With increasing slice gaps, the SNR recovers closer to the maximum SNR (when no multiband is applied). With no multiband applied, the SNR increases slightly with increasing slice gap, albeit to a lesser degree than when multiband is applied. As observed in Figure 34b, the percent difference in SNR between no multiband and multiband decreases with increasing slice gap. A substantial increase in SNR occurs when increasing the slice gap from 0 to 5 mm, while the SNR boost is relatively minor when increasing the slice gap from 5 to 10 mm. Thus, for practical purposes, a slice gap of 5 mm was implemented for the remaining in vivo tests.

Figure 35 compares the non-diffusion-weighted images for the half acquisition, the multi-slice acquisition, and the multiband acquisition.

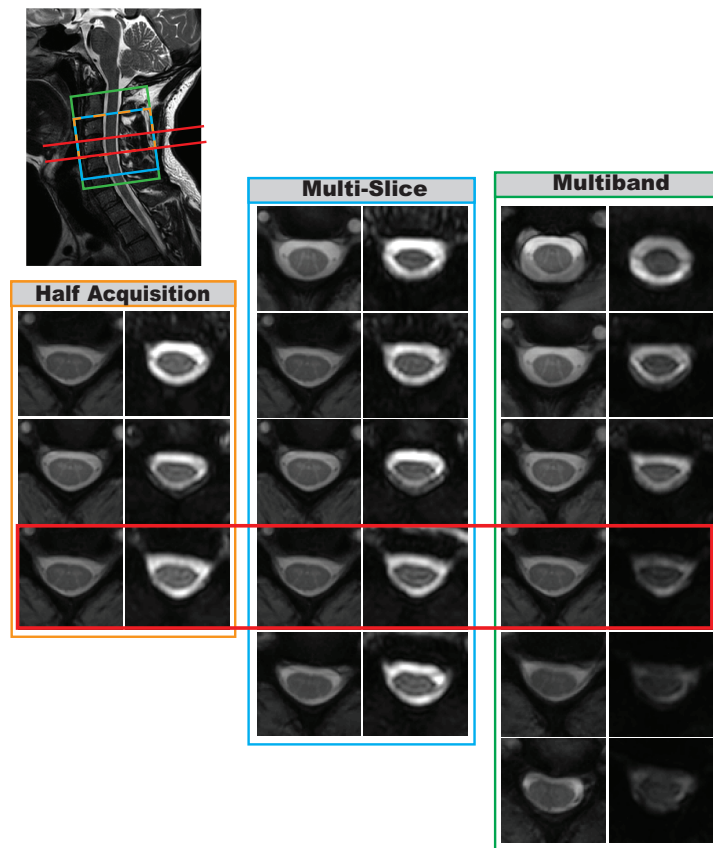


**Figure 35: Comparison of half, multi-slice, and multiband acquisition.** Top image shows slice positioning for the comparing schemes overlaid on the sagittal image, where red represents the same center slice for all of the schemes, orange for the half acquisition, blue for the multi-slice acquisition, and green for the multiband. In each box, the anatomical (mFFE) is displayed, along with the non-diffusion-weighted image for the different slices. Geometric distortion is more evident in some of the slices in the multiband sequence.

The coverage for each slice is shown in the top left, where the red box indicates where the gold standard slice was acquired. In the multiband acquisition, the signal is lower in the  $b_0$  images; additionally, geometric distortion is more evident, especially in the bottom two slices.

Figure 36 demonstrates the effect of the comparing schemes on the NODDI-derived indices  $v_{in}$  (Figure 36a and b),  $v_{iso}$  (Figure 36c and d), and ODI (Figure 36e and f).

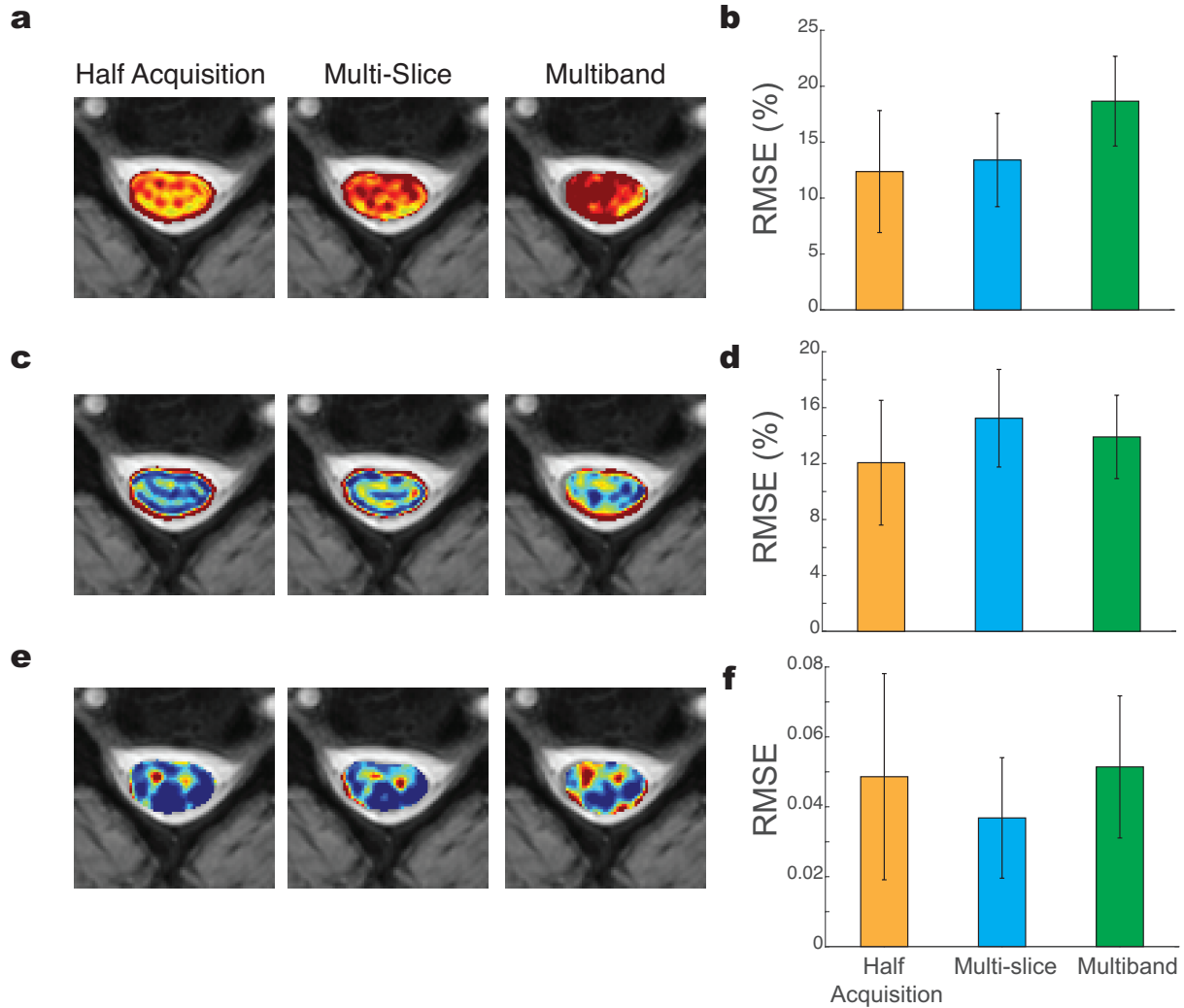


**Figure 36: NODDI-derived indices for the comparing schemes for the same slice.** (a) From left to right, the  $v_{in}$  for the half acquisition, multi-slice acquisition, and multiband acquisition is displayed. (b) RMSE plots for the acquisitions, highlighting the mean over all controls with the error bars indicating inter-subject variation. (c)  $v_{iso}$  plots for the same control and schemes as shown in (a). (d) RMSE plots for  $v_{iso}$ . (e) ODI maps for the same control and schemes as shown in (a). (f) RMSE plots for ODI.

For the axonal volume fraction ( $v_{in}$ ) estimation (Figure 36 a and b), the RMSE for the multiband sequence is highest (mean RMSE $\pm$ s.d.=18.7 $\pm$ 4.01%), whereas the RMSE for the half acquisition (12.4 $\pm$ 5.46%) and multi-slice (13.4 $\pm$ 4.17%) acquisitions are similar. The error is mainly attributed to the bias in the measurements, yielding percent errors (mean $\pm$ s.d.) of 16.5 $\pm$ 10.9%, 13.6 $\pm$ 9.96%, and 23.7 $\pm$ 24.33% for the half acquisition, multi-slice and multiband schemes respectively. The variability between slices is lowest for the half acquisition (5.35 $\pm$ 2.05%), however the variability for the multi-slice (7.45 $\pm$ 2.00%) and multiband (8.97 $\pm$ 2.85%) sequences is similar. With the isotropic volume fraction (Figure 36 c and d) and ODI (Figure 36 e and f), the errors are similar for all three acquisition schemes. The contrast between gray and white matter can still be appreciated for  $v_{in}$  and ODI in half acquisition and the multi-slice acquisition, albeit to a lesser degree than the half acquisition; with the multiband sequence, however, the bias in the fit results in difficulty in distinguishing the different tissue types from one another.

Figure 37 displays the SMT-derived  $v_{ax}$  (Figure 37a) and  $D_{ax}$  (Figure 37c), along with the corresponding error plots (Figure 37b and d) for each scheme using the full acquisition as the gold standard. The error bars indicate inter-subject variability. Qualitatively, the gray matter and white matter contrast is highest with the half acquisition scheme, while the multiband sequence provides the lowest contrast. For the axonal volume fraction estimation ( $v_{ax}$ ), with the half acquisition, the RMSE is lowest (mean RMSE $\pm$ s.d.=10.1 $\pm$ 1.50), and the variability between slices is low (mean variability $\pm$ s.d.=5.08 $\pm$ 2.93%). With the multi-slice scan, the RMSE only slightly increases to 10.6 $\pm$ 0.3% and the variability remains low (4.60 $\pm$ 2.77%). However with the multiband acquisition, the RMSE and variability both increase to 13.0 $\pm$ 2.11% and 7.36 $\pm$ 0.36% respectively. This corresponds to a mean percent error of 5.79 $\pm$ 6.3%, 6.04 $\pm$ 7.43, and 15.5 $\pm$ 17.0% for the half acquisition, multi-slice, and multiband acquisitions respectively, all of which are lower than what NODDI yielded for the same axonal volume fraction estimate. Figure 37c and d summarize the error in the comparing acquisitions for  $D_{ax}$ , where a similar trend exists, with the half acquisition providing the lowest error (0.49 $\pm$ 0.14  $\mu\text{m}^2/\text{ms}$ ). With the multi-slice acquisition, the error increases (0.64 $\pm$ 0.07  $\mu\text{m}^2/\text{ms}$ ), albeit to a smaller effect than the multiband acquisition (0.74 $\pm$ 0.14  $\mu\text{m}^2/\text{ms}$ ).

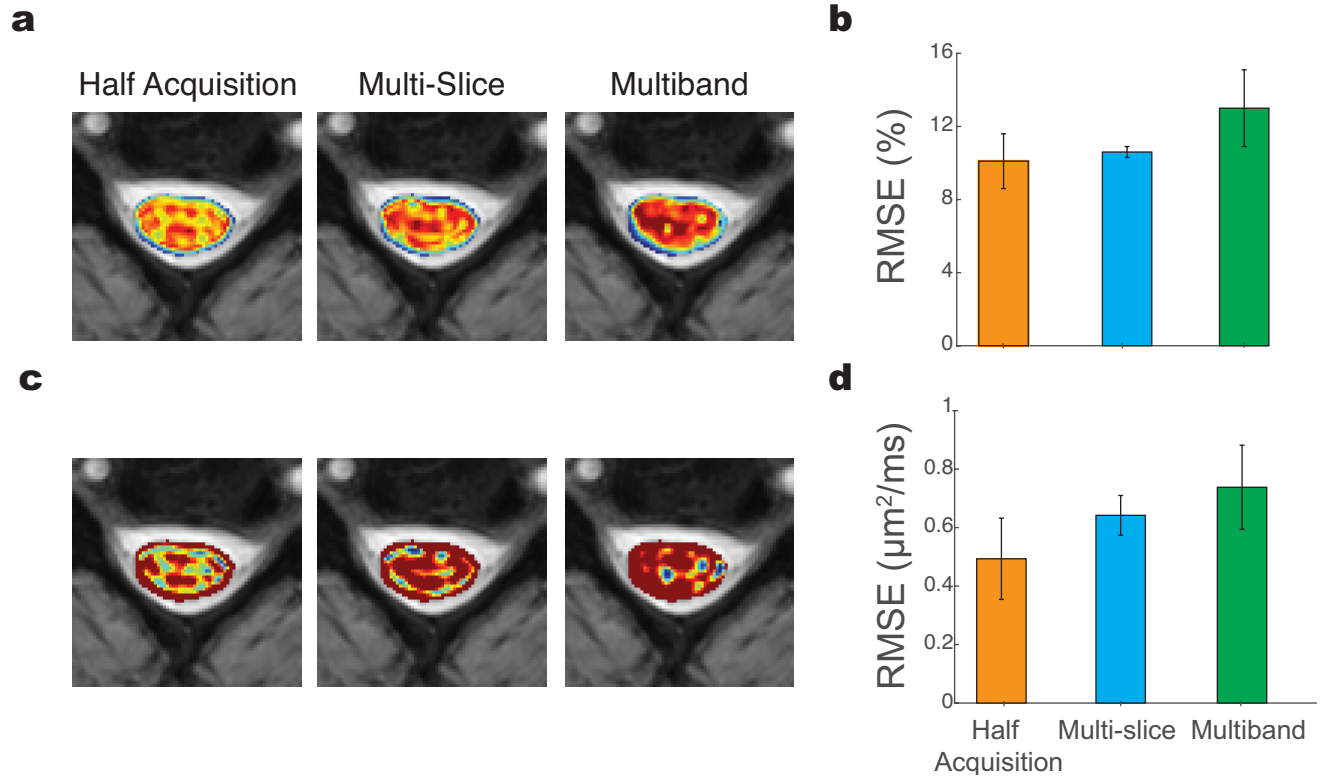


**Figure 37: SMT-derived indices for the comparing schemes for the same slice.** (a) From left to right, the  $v_{ax}$  for the half acquisition, multi-slice acquisition, and multiband acquisition is displayed. (b) RMSE plots for the acquisitions, highlighting the mean over all controls with the error bars indicating inter-subject variation. (c)  $D_{ax}$  plots for the same control and schemes as shown in (a). (d) RMSE plots for  $D_{ax}$ .

## 8.4 Discussion

With an eye towards clinical deployment, it is desirable to optimize these methods for spinal cord imaging in vivo with minimized scan time, large coverage and acceptable accuracy. To this end, we examined the possibility of 1) reducing scan times by reducing the number of gradient directions sampled in the acquisition schemes and 2) increasing coverage with conventional multi-slice imaging and simultaneous excitation of multiple slices using multiband imaging.

For the first goal of reducing scan times, reduced acquisition schemes were obtained by subsampling the originally full sampled acquisition. Therefore, the SNR of the images remained constant, and the only differing factor in the comparisons was the number of gradient directions used to fit the models. While noting that the accuracy in fits is dependent on the application at

hand, these results indicate the potential to significantly decrease scan time without sacrificing the accuracy of the derived indices. Interestingly, for the axonal volume fractions derived by both NODDI and SMT, the change in RMSE between the 2/3 and 1/2 acquisition schemes is negligible, however, for all other indices (NODDI  $v_{iso}$  and ODI, SMT  $D_{ax}$ ), there is a clear trend of increased RMSE with decreased acquisition times. When reducing the number of gradient direction in the current acquisition scheme by 50%, the error in the estimated axonal fractions for NODDI (RMSE =  $2.37 \pm 0.80\%$ ) and SMT (RMSE =  $2.55 \pm 0.72\%$ ) remained low, while also noting that the percent error of all of the NODDI- and SMT-derived indices remained under 10% for the 1/2 acquisition. Moreover, with the 1/2 acquisition, we demonstrate that the reduction in scan time does not come at a cost to sensitivity to lesions.

We also assessed the feasibility in increasing coverage with NODDI and SMT. With multiband imaging, we observed a dependency of SNR with slice gap. Given the limited number of receive coil elements in the cervical section of the neurovascular coil, increasing the slice gap would differentiate the coil sensitivities more; consequently, this would cause a reduction in the noise amplification and the ill-posed problem would be more stabilized. It is important to note that the same experiment was performed using the 32-channel head coil, and no dependency between SNR and slice gap was observed (data not shown). In vivo, the recovery in SNR from 5 mm to 10 or 20 mm was negligible, and therefore, we implemented a multiband acquisition with a slice gap of 5 mm. For SMT, in comparison to the multiband sequence, the multi-slice acquisition produced lower variability between slices, along with smaller RMSE at the center slice. The major difference between the multi-slice and multiband sequences can be attributed to the increased geometric distortion due to susceptibility present in the multiband sequence. With the multiband sequence, system restrictions (duty cycle, peripheral nerve stimulation [PNS], or specific absorption rate [SAR]) required an increase of TR from 65 to 73 ms when using high b-values (b-value  $>2000$  s/mm<sup>2</sup>); given this consequential SNR decrease, SENSE was turned off in the multiband sequence to avoid any further decreases in SNR. The inconsistency observed between slices with the multiband sequence would make it difficult to perform reliable comparisons for longitudinal and cohort studies. Furthermore, we note that some of the error in all of the non-single slice acquisitions may be attributed to possible undesirable RF excitation from different slices, preventing the perturbed magnetization from recovering fully.

We note a difference in SNR dependency between SMT and NODDI. A small increase in

the SNR can be observed by comparing the half acquisition scheme to the multi-slice scheme, as the number of averages was decreased from 3 to 2 in order to accommodate an increase in TR to minimize physiological motion and CSF pulsation effects due to the cardiac cycle. There is a larger decrease in SNR with the multiband sequence, however, and for NODDI, it is evident that the fitting is more dependent on SNR than with SMT, as observed by the large bias in the fitting for the axonal volume fraction ( $v_{in}$ ). Furthermore, for all sequence comparisons, SMT yielded lower errors (both percent error and RMSE) than NODDI. This is expected, as SMT averages over all of the gradient directions for a given b-value and therefore, inherently provides an SNR boost over NODDI. Therefore, in a clinical setting, SMT is likely more robust than NODDI.

A limitation in this study was the long scan time required in order to perform all four diffusion sequences (gold standard, half scheme, multi-slice and multiband). This is likely to produce intra-session error, and this may bias the error calculated from the gold standard, depending on when in the scan session each scheme was acquired. While the scan protocol order did not change for any of the controls, it is difficult to account for this intra-session error. However, we note that the same trends in error were observed for all controls, and therefore this intra-session error should not effect the overall conclusions drawn from comparison of these methods.

In conclusion, we demonstrate the possibility of imaging multiple levels of the cervical spinal cord in a reasonable scan time without sacrificing confidence in the SMT-derived indices. For NODDI, we observed a dependency to SNR on the accuracy of the derived measurements, and therefore, it is more challenging to translate NODDI clinically in terms of providing large coverage in a reasonable scan time. Taken together, this represents an important step forwards in the field of MS imaging given the shortage of sequences sensitive to axonal loss and the paramount need of these MRI methods.

## CHAPTER 9

### Conclusions and Future Directions

Theoretical physicist Howard Georgi in a review article (149) states, “One of the most astonishing things about the world we live in is that there seems to be interesting physics at all scales. To do physics amid this remarkable richness, it is convenient to be able to isolate a set of phenomena from all the rest, so that we can describe it without having to understand everything. Fortunately this is often possible. We can divide the parameter space of the world into different regions, in each of which there is a different appropriate description of the important physics.” In essence, this quote describes the main goal of this work: to understand the limitations of different diffusion models for in vivo characterization of the spinal cord.

This work has described the microstructural characterization of the human spinal cord in vivo. To enable this, first, we investigated the bias in conventional DTI measurements. Conventional DTI techniques were optimized in terms of accuracy and reproducibility, concluding that a sequence of 15 directions in 9 minutes yielded low error. Second, we explored the feasibility of advanced biophysical diffusion methods, which offers the ability to provide measures of axonal volume fractions. While there are a number of possible methods to implement, we focused our attention to three methods in particular: 1) NODDI, 2) SMT and 3) DBSI. Given the promise in disentangling specific aspects of DTI indices, these biophysical models have gained traction in the past few years, but have not been extensively applied to the spinal cord in disease cohorts. These methods were individually assessed based on reproducibility, model fit (BIC, goodness-of-fit), and sensitivity to distinguish disparity between MS patients and healthy controls, in addition to comparing their performance to signal models DTI and DKI. In the second aim, we concluded that NODDI and SMT are both feasible, however, DBSI still remains challenging in accurately characterizing the data in the patient population. Lastly, we investigated the potential sources of error in these biophysical models (SMT and NODDI) to optimize the acquisition schemes in terms of reduced acquisition time and increased coverage. Using data reduction strategies and conventional multi-slice imaging, it was feasible to acquire up to five levels in the cervical segment in less than 10 minutes.

Taken together, the results herein favored SMT over NODDI in terms of clinical

translation. In a high SNR regime, NODDI and SMT provided similar measures of axonal volume fractions, in addition to comparable reproducibility. However, SMT provided more robustness to optimized schemes for shorter acquisition times and increased coverage. This is expected, as NODDI's complex model requires more constraints, which are not necessarily easily applied to a large cohort of patients. Future work involving histological validation of SMT would be worthwhile and could propel the clinical translation of SMT. With histological validation, the accuracy of the SMT measurements would be validated. Furthermore, optimization of the SMT protocol in terms of number of b-value shells and number of gradient directions in each shell may provide more sensitivity in the derived indices. Another technical direction stemming from this work would be the investigation of more complex biophysical modeling using the SMT approach. For example, a three-compartment model could be implemented, accounting for the isotropic component (cerebrospinal fluid, gliosis in pathology, etc.) of the diffusion signal.

Targeting the overarching potential of this work, another interesting extension would be the implementation of SMT to a larger, and more diverse, cohort of MS patients, including correlation to clinical measures. While the work in this dissertation served as a promising preliminary application, a larger study will allow assessment of its prognostic capability. Doing so may enable longitudinal tracking of treatment plans and disease progression. Axonal loss can be the main cause of irreversible, neurological impairment, and given the advent of neuroprotective therapies (150), the ability to capture axonal loss prior to disability would provide significant clinical implications and improved patient quality of life. To this end, NODDI and SMT should also be considered in a multi-modality study, which may be beneficial in the understanding of MS. For example, the combination of quantitative magnetization transfer (qMT) (151), chemical exchange saturation transfer (CEST) (152), and diffusion such as NODDI or SMT, could provide a comprehensive assessment of the spinal cord in terms of myelin, metabolic and axonal content respectively.

Given the superior fit of DKI over NODDI, investigation of the white matter tract integrity (WMTI) model in the spinal cord would be interesting. With WMTI, biophysical parameters, such as the axonal volume fraction, are estimated from the kurtosis (66). While the methods discussed in this work quantify axonal volume fractions, mapping axon diameters is another active area of study. Studies involving postmortem tissue have demonstrated that smaller



axons have a higher probability of being targeted in chronic and acute lesions of MS (153). A recent study has used Human Connectome gradients ( $G \sim 300$  mT/m) in order to estimate axon diameter sizes in the spinal cord using AxCaliber. Such methods would be difficult to implement currently on clinical scanners ( $G \sim 60$  mT/m), where the gradients are far less advanced than those implemented on the Human Connectome scanner, as a resolution limit exists (154). Oscillating gradient spin echo (OGSE), however, has become a promising technique to achieve shorter diffusion times (17,155), and hence, is an attractive method to map axon diameters clinically, but has never been studied in the human spinal cord in vivo.

The use of the Human Connectome gradients, however, may be a viable option to explore the potential of DBSI in the human spinal cord in vivo. Studies have reported the impact of gradient strength on the possible axon diameter estimation limit (156), where the lower limit on clinical scanners is about  $4 \mu\text{m}$ ; using Human Connectome gradients, however, the limit is  $2 \mu\text{m}$ . These improvements may enable better separation of the isotropic component in the spinal cord using the DBSI model.

In conclusion, the work presented here describes the feasibility and potential of novel diffusion methods for the cervical spinal cord, serving as a vital stepping stone towards the clinical implementation of characterizing spinal cord microstructure.

## BIBLIOGRAPHY

1. Dendrou CA, Fugger L, Friese MA. Immunopathology of multiple sclerosis. *Nat Rev Immunol* 2015;15(9):545-558.
2. Nair G, Absinta M, Reich DS. Optimized T1-MPRAGE sequence for better visualization of spinal cord multiple sclerosis lesions at 3T. *AJNR Am J Neuroradiol* 2013;34(11):2215-2222.
3. Basser PJ, Mattiello J, LeBihan D. MR diffusion tensor spectroscopy and imaging. *Biophys J* 1994;66(1):259-267.
4. Song SK, Yoshino J, Le TQ, Lin SJ, Sun SW, Cross AH, Armstrong RC. Demyelination increases radial diffusivity in corpus callosum of mouse brain. *Neuroimage* 2005;26(1):132-140.
5. Oh J, Zackowski K, Chen M, Newsome S, Saidha S, Smith SA, Diener-West M, Prince J, Jones CK, Van Zijl PC. Multiparametric MRI correlates of sensorimotor function in the spinal cord in multiple sclerosis. *Mult Scler J* 2012:427-435.
6. Budde MD, Kim JH, Liang HF, Russell JH, Cross AH, Song SK. Axonal injury detected by in vivo diffusion tensor imaging correlates with neurological disability in a mouse model of multiple sclerosis. *NMR Biomed* 2008;21(6):589-597.
7. Kärger J. NMR self-diffusion studies in heterogeneous systems. *Adv Colloid Interface Sci* 1985;23:129-148.
8. Assaf Y, Cohen Y. Assignment of the water slow-diffusing component in the central nervous system using q-space diffusion MRS: implications for fiber tract imaging. *Magn Reson Med* 2000;43(2):191-199.
9. Jensen JH, Helpern JA, Ramani A, Lu H, Kaczynski K. Diffusional kurtosis imaging: the quantification of non-gaussian water diffusion by means of magnetic resonance imaging. *Magn Reson Med* 2005;53(6):1432-1440.
10. Zhang H, Schneider T, Wheeler-Kingshott CA, Alexander DC. NODDI: practical in vivo neurite orientation dispersion and density imaging of the human brain. *Neuroimage* 2012;61(4):1000-1016.
11. Chiang CW, Wang Y, Sun P, Lin TH, Trinkaus K, Cross AH, Song SK. Quantifying white matter tract diffusion parameters in the presence of increased extra-fiber cellularity and vasogenic edema. *Neuroimage* 2014;101:310-319.

12. Assaf Y, Blumenfeld-Katzir T, Yovel Y, Basser PJ. AxCaliber: a method for measuring axon diameter distribution from diffusion MRI. *Magn Reson Med* 2008;59(6):1347-1354.
13. Assaf Y, Basser PJ. Composite hindered and restricted model of diffusion (CHARMED) MR imaging of the human brain. *Neuroimage* 2005;27(1):48-58.
14. Stanisz GJ, Szafer A, Wright GA, Henkelman RM. An analytical model of restricted diffusion in bovine optic nerve. *Magn Reson Med* 1997;37(1):103-111.
15. Behrens TE, Woolrich MW, Jenkinson M, Johansen-Berg H, Nunes RG, Clare S, Matthews PM, Brady JM, Smith SM. Characterization and propagation of uncertainty in diffusion-weighted MR imaging. *Magn Reson Med* 2003;50(5):1077-1088.
16. Alexander DC. A general framework for experiment design in diffusion MRI and its application in measuring direct tissue-microstructure features. *Magn Reson Med* 2008;60(2):439-448.
17. Xu J, Li H, Harkins KD, Jiang X, Xie J, Kang H, Does MD, Gore JC. Mapping mean axon diameter and axonal volume fraction by MRI using temporal diffusion spectroscopy. *Neuroimage* 2014;103:10-19.
18. Stroman PW, Wheeler-Kingshott C, Bacon M, Schwab JM, Bosma R, Brooks J, Cadotte D, Carlstedt T, Ciccarelli O, Cohen-Adad J, Curt A, Evangelou N, Fehlings MG, Filippi M, Kelley BJ, Kollias S, Mackay A, Porro CA, Smith S, Strittmatter SM, Summers P, Tracey I. The current state-of-the-art of spinal cord imaging: methods. *Neuroimage* 2014;84:1070-1081.
19. What is MS? Volume 2017: National Multiple Sclerosis Society.
20. Brück W. The pathology of multiple sclerosis is the result of focal inflammatory demyelination with axonal damage. *J Neurol* 2005;252(5):v3-v9.
21. Compston A, Coles A. Multiple sclerosis. *Lancet* 2008;372(9648):1502-1517.
22. Kurtzke JF. Rating neurologic impairment in multiple sclerosis: an expanded disability status scale (EDSS). *Neurology* 1983;33(11):1444-1452.
23. Prineas JW, Parratt JD. Oligodendrocytes and the early multiple sclerosis lesion. *Ann Neurol* 2012;72(1):18-31.
24. Medana I, Esiri M. Axonal damage: a key predictor of outcome in human CNS diseases. *Brain* 2003;126(3):515-530.

25. Trapp BD, Peterson J, Ransohoff RM, Rudick R, Mork S, Bo L. Axonal transection in the lesions of multiple sclerosis. *N Engl J Med* 1998;338(5):278-285.
26. Ferguson B, Matyszak MK, Esiri MM, Perry VH. Axonal damage in acute multiple sclerosis lesions. *Brain* 1997;120(3):393-399.
27. Polman CH, Reingold SC, Banwell B, Clanet M, Cohen JA, Filippi M, Fujihara K, Havrdova E, Hutchinson M, Kappos L. Diagnostic criteria for multiple sclerosis: 2010 revisions to the McDonald criteria. *Ann Neurol* 2011;69(2):292-302.
28. Bot JC, Barkhof F, Polman CH, Lycklama a Nijeholt GJ, de Groot V, Bergers E, Ader HJ, Castelijns JA. Spinal cord abnormalities in recently diagnosed MS patients: added value of spinal MRI examination. *Neurology* 2004;62(2):226-233.
29. Barkhof F. The clinico-radiological paradox in multiple sclerosis revisited. *Curr Opin Neurol* 2002;15(3):239-245.
30. Einstein A. On the motion required by the molecular kinetic theory of heat of small particles suspended in a stationary liquid. *Annalen der Physik* 1905;17(549).
31. Beaulieu C. The basis of anisotropic water diffusion in the nervous system - a technical review. *NMR Biomed* 2002;15(7-8):435-455.
32. Jones DK. *Diffusion MRI : theory, methods, and applications*. 2011.
33. Stejskal EO, Tanner JE. Spin diffusion measurements: spin echoes in the presence of a time-dependent field gradient. *J Chem Phys* 1965;42(1):288-292.
34. Bloch F. Nuclear induction. *Phys rev* 1946;70(7-8):460.
35. Torrey HC. Bloch Equations with Diffusion Terms. *Phys rev* 1956;104(3):563-565.
36. Le Bihan D, Breton E. Imagerie de diffusion in-vivo par résonance magnétique nucléaire. *Comptes-Rendus de l'Académie des Sciences* 1985;93(5):27-34.
37. Le Bihan D, Breton E, Lallemand D, Grenier P, Cabanis E, Laval-Jeantet M. MR imaging of intravoxel incoherent motions: application to diffusion and perfusion in neurologic disorders. *Radiology* 1986;161(2):401-407.
38. Kingsley PB. Introduction to diffusion tensor imaging mathematics: Part II. Anisotropy, diffusion-weighting factors, and gradient encoding schemes. *Concepts Magn Reson Part A* 2006;28A(2):123-154.

39. Zollinger LV, Kim TH, Hill K, Jeong EK, Rose JW. Using diffusion tensor imaging and immunofluorescent assay to evaluate the pathology of multiple sclerosis. *J Magn Reson Imaging* 2011;33(3):557-564.
40. Klawiter EC, Schmidt RE, Trinkaus K, Liang HF, Budde MD, Naismith RT, Song SK, Cross AH, Benzinger TL. Radial diffusivity predicts demyelination in ex vivo multiple sclerosis spinal cords. *Neuroimage* 2011;55(4):1454-1460.
41. DeBoy CA, Zhang J, Dike S, Shats I, Jones M, Reich DS, Mori S, Nguyen T, Rothstein B, Miller RH, Griffin JT, Kerr DA, Calabresi PA. High resolution diffusion tensor imaging of axonal damage in focal inflammatory and demyelinating lesions in rat spinal cord. *Brain* 2007;130(Pt 8):2199-2210.
42. Budde MD, Xie M, Cross AH, Song S-K. Axial diffusivity is the primary correlate of axonal injury in the experimental autoimmune encephalomyelitis spinal cord: a quantitative pixelwise analysis. *J Neurosci* 2009;29(9):2805-2813.
43. Kearney H, Miller DH, Ciccarelli O. Spinal cord MRI in multiple sclerosis-diagnostic, prognostic and clinical value. *Nature reviews Neurology* 2015;11(6):327-338.
44. Agosta F, Benedetti B, Rocca MA, Valsasina P, Rovaris M, Comi G, Filippi M. Quantification of cervical cord pathology in primary progressive MS using diffusion tensor MRI. *Neurology* 2005;64(4):631-635.
45. Valsasina P, Rocca MA, Agosta F, Benedetti B, Horsfield MA, Gallo A, Rovaris M, Comi G, Filippi M. Mean diffusivity and fractional anisotropy histogram analysis of the cervical cord in MS patients. *Neuroimage* 2005;26(3):822-828.
46. Agosta F, Absinta M, Sormani MP, Ghezzi A, Bertolotto A, Montanari E, Comi G, Filippi M. In vivo assessment of cervical cord damage in MS patients: a longitudinal diffusion tensor MRI study. *Brain* 2007;130(Pt 8):2211-2219.
47. Hesseltine SM, Law M, Babb J, Rad M, Lopez S, Ge Y, Johnson G, Grossman RI. Diffusion tensor imaging in multiple sclerosis: assessment of regional differences in the axial plane within normal-appearing cervical spinal cord. *AJNR Am J Neuroradiol* 2006;27(6):1189-1193.
48. Assaf Y, Cohen Y. Non-mono-exponential attenuation of water and N-acetyl aspartate signals due to diffusion in brain tissue. *J Magn Reson* 1998;131(1):69-85.
49. Bar-Shir A, Avram L, Ozarslan E, Basser PJ, Cohen Y. The effect of the diffusion time and pulse gradient duration ratio on the diffraction pattern and the structural information estimated from q-space diffusion MR: experiments and simulations. *J Magn Reson*

2008;194(2):230-236.

50. Farrell JA, Smith SA, Gordon-Lipkin EM, Reich DS, Calabresi PA, van Zijl PC. High b-value q-space diffusion-weighted MRI of the human cervical spinal cord in vivo: feasibility and application to multiple sclerosis. *Magn Reson Med* 2008;59(5):1079-1089.
51. Farrell JA, Zhang J, Jones MV, Deboy CA, Hoffman PN, Landman BA, Smith SA, Reich DS, Calabresi PA, van Zijl PC. q-space and conventional diffusion imaging of axon and myelin damage in the rat spinal cord after axotomy. *Magn Reson Med* 2010;63(5):1323-1335.
52. Assaf Y, Mayk A, Cohen Y. Displacement imaging of spinal cord using q-space diffusion-weighted MRI. *Magn Reson Med* 2000;44(5):713-722.
53. Ong HH, Wehrli FW. Quantifying axon diameter and intra-cellular volume fraction in excised mouse spinal cord with q-space imaging. *Neuroimage* 2010;51(4):1360-1366.
54. Niendorf T, Dijkhuizen RM, Norris DG, van Lookeren Campagne M, Nicolay K. Biexponential diffusion attenuation in various states of brain tissue: Implications for diffusion-weighted imaging. *Magn Reson Med* 1996;36(6):847-857.
55. Biton IE, Mayk A, Kidron D, Assaf Y, Cohen Y. Improved detectability of experimental allergic encephalomyelitis in excised swine spinal cords by high b-value q-space DWI. *Exp Neurol* 2005;195(2):437-446.
56. Biton IE, Duncan ID, Cohen Y. High b-value q-space diffusion MRI in myelin-deficient rat spinal cords. *Magn Reson Imaging* 2006;24(2):161-166.
57. Ong HH, Wright AC, Wehrli SL, Souza A, Schwartz ED, Hwang SN, Wehrli FW. Indirect measurement of regional axon diameter in excised mouse spinal cord with q-space imaging: simulation and experimental studies. *Neuroimage* 2008;40(4):1619-1632.
58. Steven AJ, Zhuo J, Melhem ER. Diffusion kurtosis imaging: an emerging technique for evaluating the microstructural environment of the brain. *AJR Am J Roentgenol* 2013.
59. Raz E, Bester M, Sigmund E, Tabesh A, Babb J, Jaggi H, Helpert J, Mitnick R, Inglese M. A better characterization of spinal cord damage in multiple sclerosis: a diffusional kurtosis imaging study. *AJNR Am J Neuroradiol* 2013;34(9):1846-1852.
60. Cheung M, Hui E, Wu E, Wu E. Comparison of directional diffusion kurtoses and diffusivities in EAE-induced spinal cord. *Proc Int Soc Magn Reson Med*, 2008; 3328.
61. Kelm ND, West KL, Carson RP, Gochberg DF, Ess KC, Does MD. Evaluation of

- diffusion kurtosis imaging in ex vivo hypomyelinated mouse brains. *Neuroimage* 2016;124, Part A:612-626.
62. Mulkern RV, Gudbjartsson H, Westin C-F, Zengingonul HP, Gartner W, Guttman CR, Robertson RL, Kyriakos W, Schwartz R, Holtzman D. Multi-component apparent diffusion coefficients in human brain. *NMR Biomed* 1999;12:51-62.
  63. Komlosch ME, Özarlan E, Lizak MJ, Horkayne-Szakaly I, Freidlin RZ, Horkay F, Basser PJ. Mapping average axon diameters in porcine spinal cord white matter and rat corpus callosum using d-PFG MRI. *Neuroimage* 2013;78:210-216.
  64. Alexander DC, Hubbard PL, Hall MG, Moore EA, Ptito M, Parker GJ, Dyrby TB. Orientationally invariant indices of axon diameter and density from diffusion MRI. *Neuroimage* 2010;52(4):1374-1389.
  65. Jespersen SN, Kroenke CD, Østergaard L, Ackerman JJH, Yablonskiy DA. Modeling dendrite density from magnetic resonance diffusion measurements. *Neuroimage* 2007;34(4):1473-1486.
  66. Fieremans E, Jensen JH, Helpers JA. White matter characterization with diffusional kurtosis imaging. *Neuroimage* 2011;58(1):177-188.
  67. Wang Y, Wang Q, Haldar JP, Yeh FC, Xie M, Sun P, Tu TW, Trinkaus K, Klein RS, Cross AH, Song SK. Quantification of increased cellularity during inflammatory demyelination. *Brain* 2011;134(Pt 12):3590-3601.
  68. Kaden E, Kelm ND, Carson RP, Does MD, Alexander DC. Multi-compartment microscopic diffusion imaging. *Neuroimage* 2016.
  69. Kaden E, Kruggel F, Alexander DC. Quantitative mapping of the per-axon diffusion coefficients in brain white matter. *Magn Reson Med* 2016;75(4):1752-1763.
  70. Panagiotaki E, Schneider T, Siow B, Hall MG, Lythgoe MF, Alexander DC. Compartment models of the diffusion MR signal in brain white matter: a taxonomy and comparison. *Neuroimage* 2012;59(3):2241-2254.
  71. Ferizi U, Schneider T, Panagiotaki E, Nedjati-Gilani G, Zhang H, Wheeler-Kingshott CAM, Alexander DC. A ranking of diffusion MRI compartment models with in vivo human brain data. *Magn Reson Med* 2014;72(6):1785-1792.
  72. Ferizi U, Schneider T, Witzel T, Wald LL, Zhang H, Wheeler-Kingshott CAM, Alexander DC. White matter compartment models for in vivo diffusion MRI at 300 mT/m. *Neuroimage* 2015;118:468-483.

73. Jespersen SN, Bjarkam CR, Nyengaard JR, Chakravarty MM, Hansen B, Vosegaard T, Ostergaard L, Yablonskiy D, Nielsen NC, Vestergaard-Poulsen P. Neurite density from magnetic resonance diffusion measurements at ultrahigh field: comparison with light microscopy and electron microscopy. *Neuroimage* 2010;49(1):205-216.
74. Grussu F, Schneider T, Yates R, Tachrount M, Newcombe J, Zhang H, Alexander D, DeLuca G, Wheeler-Kingshott C. Histological metrics confirm microstructural characteristics of NODDI indices in multiple sclerosis spinal cord. *Proc Intl Soc Mag Reson Med*, 2015; 0909.
75. Grussu F, Schneider T, Zhang H, Alexander DC, Wheeler-Kingshott CA. Neurite orientation dispersion and density imaging of the healthy cervical spinal cord in vivo. *Neuroimage* 2015;111:590-601.
76. Wang X, Cusick MF, Wang Y, Sun P, Libbey JE, Trinkaus K, Fujinami RS, Song SK. Diffusion basis spectrum imaging detects and distinguishes coexisting subclinical inflammation, demyelination and axonal injury in experimental autoimmune encephalomyelitis mice. *NMR Biomed* 2014;27(7):843-852.
77. Wang Y, Sun P, Wang Q, Trinkaus K, Schmidt RE, Naismith RT, Cross AH, Song SK. Differentiation and quantification of inflammation, demyelination and axon injury or loss in multiple sclerosis. *Brain* 2015;138(Pt 5):1223-1238.
78. Murphy RK, Sun P, Xu J, Wang Y, Sullivan S, Gamble P, Wagner J, Wright NN, Dorward IG, Riew D, Santiago P, Kelly MP, Trinkaus K, Ray WZ, Song SK. Magnetic Resonance Imaging Biomarker of Axon Loss Reflects Cervical Spondylotic Myelopathy Severity. *Spine* 2015;9:751-756.
79. Duval T, McNab JA, Setsompop K, Witzel T, Schneider T, Huang SY, Keil B, Klawiter EC, Wald LL, Cohen-Adad J. In vivo mapping of human spinal cord microstructure at 300 mT/m. *Neuroimage* 2015;118:494-507.
80. Setsompop K, Kimmlingen R, Eberlein E, Witzel T, Cohen-Adad J, McNab JA, Keil B, Tisdall MD, Hoecht P, Dietz P, Cauley SF, Tountcheva V, Matschl V, Lenz VH, Heberlein K, Potthast A, Thein H, Van Horn J, Toga A, Schmitt F, Lehne D, Rosen BR, Wedeen V, Wald LL. Pushing the limits of in vivo diffusion MRI for the Human Connectome Project. *Neuroimage* 2013;80:220-233.
81. Smith SA, Edden RA, Farrell JA, Barker PB, Van Zijl PC. Measurement of T1 and T2 in the cervical spinal cord at 3 tesla. *Magn Reson Med* 2008;60(1):213-219.
82. Wilm BJ, Svensson J, Henning A, Pruessmann KP, Boesiger P, Kollias SS. Reduced field-of-view MRI using outer volume suppression for spinal cord diffusion imaging. *Magn Reson Med* 2007;57(3):625-630.



83. Dowell NG, Jenkins TM, Ciccarelli O, Miller DH, Wheeler-Kingshott CAM. Contiguous-slice zonally oblique multislice (CO-ZOOM) diffusion tensor imaging: Examples of in vivo spinal cord and optic nerve applications. *J Magn Reson Im* 2009;29(2):454-460.
84. Summers P, Staempfli P, Jaermann T, Kwiecinski S, Kollias S. A preliminary study of the effects of trigger timing on diffusion tensor imaging of the human spinal cord. *AJNR Am J Neuroradiol* 2006;27(9):1952-1961.
85. Elster AD. Cardiac Gating Parameters. *Questions and Answers in MRI. Volume 2017;* 2017.
86. Alexander AL, Lee JE, Lazar M, Field AS. Diffusion tensor imaging of the brain. *Neurotherapeutics* 2007;4(3):316-329.
87. Basser PJ, Pierpaoli C. Microstructural and physiological features of tissues elucidated by quantitative-diffusion-tensor MRI. *Journal of magnetic resonance Series B* 1996;111(3):209-219.
88. Bozzali M, Falini A, Franceschi M, Cercignani M, Zuffi M, Scotti G, Comi G, Filippi M. White matter damage in Alzheimer's disease assessed in vivo using diffusion tensor magnetic resonance imaging. *Journal of neurology, neurosurgery, and psychiatry* 2002;72(6):742-746.
89. Kandel ER, Schwartz JH, Jessell TM. *Principles of neural science: McGraw-hill New York;* 2000.
90. Clark CA, Werring DJ. Diffusion tensor imaging in spinal cord: methods and applications - a review. *NMR Biomed* 2002;15(7-8):578-586.
91. Anderson AW. Theoretical analysis of the effects of noise on diffusion tensor imaging. *Magn Reson Med* 2001;46(6):1174-1188.
92. Skare S, Hedehus M, Moseley ME, Li TQ. Condition number as a measure of noise performance of diffusion tensor data acquisition schemes with MRI. *J Magn Reson* 2000;147(2):340-352.
93. Jones DK, Basser PJ. "Squashing peanuts and smashing pumpkins": how noise distorts diffusion-weighted MR data. *Magn Reson Med* 2004;52(5):979-993.
94. Landman BA, Farrell JAD, Jones CK, Smith SA, Prince JL, Mori S. Effects of diffusion weighting schemes on the reproducibility of DTI-derived fractional anisotropy, mean diffusivity, and principal eigenvector measurements at 1.5T. *Neuroimage*

2007;36(4):1123-1138.

95. Farrell JAD, Landman BA, Jones CK, Smith SA, Prince JL, van Zijl PCM, Mori S. Effects of signal-to-noise ratio on the accuracy and reproducibility of diffusion tensor imaging–derived fractional anisotropy, mean diffusivity, and principal eigenvector measurements at 1.5T. *J Magn Reson Im* 2007;26(3):756-767.
96. Ni H, Kavcic V, Zhu T, Ekholm S, Zhong J. Effects of number of diffusion gradient directions on derived diffusion tensor imaging indices in human brain. *AJNR Am J Neuroradiol* 2006;27(8):1776-1781.
97. Lee JW, Kim JH, Kang HS, Lee JS, Choi JY, Yeom JS, Kim HJ, Chung HW. Optimization of acquisition parameters of diffusion-tensor magnetic resonance imaging in the spinal cord. *Invest Radiol* 2006;41(7):553-559.
98. Wheeler-Kingshott CAM, Hickman SJ, Parker GJM, Ciccarelli O, Symms MR, Miller DH, Barker GJ. Investigating Cervical Spinal Cord Structure Using Axial Diffusion Tensor Imaging. *Neuroimage* 2002;16(1):93-102.
99. Santarelli X, Garbin G, Ukmar M, Longo R. Dependence of the fractional anisotropy in cervical spine from the number of diffusion gradients, repeated acquisition and voxel size. *Magn Reson Imaging* 2010;28(1):70-76.
100. Held P, Dorenbeck U, Seitz J, Fründ R, Albrich H. MRI of the abnormal cervical spinal cord using 2D spoiled gradient echo multiecho sequence (MEDIC) with magnetization transfer saturation pulse. A T2\* weighted feasibility study. *J Neuroradiol* 2003;30(2):83-90.
101. Jenkinson M, Beckmann CF, Behrens TE, Woolrich MW, Smith SM. *Fsl*. *Neuroimage* 2012;62(2):782-790.
102. Leemans A, Jones DK. The B-matrix must be rotated when correcting for subject motion in DTI data. *Magn Reson Med* 2009;61(6):1336-1349.
103. Asman AJ, Bryan FW, Smith SA, Reich DS, Landman BA. Groupwise multi-atlas segmentation of the spinal cord’s internal structure. *Med Image Anal* 2014;18(3):460-471.
104. Cook PA, Bai Y, Nedjati-Gilani S, Seunarine KK, Hall MG, Parker GJ, Alexander DC. Camino: Open-Source Diffusion-MRI Reconstruction and Processing. *Proc Intl Soc Mag Reson Med*. Seattle, WA, USA, 2006; 2759.
105. Bland JM, Altman DG. Statistical methods for assessing agreement between two methods

- of clinical measurement. *Lancet* 1986;1:307-310.
106. Pierpaoli C, Jezzard P, Basser PJ, Barnett A, Di Chiro G. Diffusion tensor MR imaging of the human brain. *Radiology* 1996;201(3):637-648.
  107. Choe AS, Belegu V, Yoshida S, Joel S, Sadowsky CL, Smith SA, van Zijl PC, Pekar JJ, McDonald JW. Extensive neurological recovery from a complete spinal cord injury: a case report and hypothesis on the role of cortical plasticity. *Front Hum Neurosci* 2013;7:290-305.
  108. Koskinen E, Brander A, Hakulinen U, Luoto T, Helminen M, Ylinen A, Öhman J. Assessing the state of chronic spinal cord injury using diffusion tensor imaging. *J Neurotrauma* 2013;30(18):1587-1595.
  109. Kamble RB, Venkataramana NK, Naik AL, Rao SV. Diffusion tensor imaging in spinal cord injury. *Indian J Radiol Imaging* 2011;21(3):221-224.
  110. Song T, Chen W-J, Yang B, Zhao H-P, Huang J-W, Cai M-J, Dong T-F, Li T-S. Diffusion tensor imaging in the cervical spinal cord. *European Spine Journal* 2011;20(3):422-428.
  111. Jones DK. The effect of gradient sampling schemes on measures derived from diffusion tensor MRI: a Monte Carlo study. *Magn Reson Med* 2004;51(4):807-815.
  112. Cohen-Adad J, Benali H, Hoge RD, Rossignol S. In vivo DTI of the healthy and injured cat spinal cord at high spatial and angular resolution. *Neuroimage* 2008;40(2):685-697.
  113. Cohen-Adad J, El Mendili MM, Lehericy S, Pradat PF, Blancho S, Rossignol S, Benali H. Demyelination and degeneration in the injured human spinal cord detected with diffusion and magnetization transfer MRI. *Neuroimage* 2011;55(3):1024-1033.
  114. Saritas EU, Cunningham CH, Lee JH, Han ET, Nishimura DG. DWI of the spinal cord with reduced FOV single-shot EPI. *Magn Reson Med* 2008;60(2):468-473.
  115. Toosy AT, Kou N, Altmann D, Wheeler-Kingshott CA, Thompson AJ, Ciccarelli O. Voxel-based cervical spinal cord mapping of diffusion abnormalities in MS-related myelitis. *Neurology* 2014;83(15):1321-1325.
  116. Lebel C, Benner T, Beaulieu C. Six is enough? Comparison of diffusion parameters measured using six or more diffusion-encoding gradient directions with deterministic tractography. *Magn Reson Med* 2012;68(2):474-483.
  117. Setsompop K, Cohen-Adad J, Gagoski BA, Raij T, Yendiki A, Keil B, Wedeen VJ, Wald

- LL. Improving diffusion MRI using simultaneous multi-slice echo planar imaging. *Neuroimage* 2012;63(1):569-580.
118. Jones DK, Horsfield MA, Simmons A. Optimal strategies for measuring diffusion in anisotropic systems by magnetic resonance imaging. *Magn Reson Med* 1999;42(3):515-525.
  119. Wen Q, Kelley DAC, Banerjee S, Lupo JM, Chang SM, Xu D, Hess CP, Nelson SJ. Clinically feasible NODDI characterization of glioma using multiband EPI at 7 T. *NeuroImage Clinical* 2015;9:291-299.
  120. Billiet T, Mädler B, D'Arco F, Peeters R, Deprez S, Plasschaert E, Leemans A, Zhang H, Van den Bergh B, Vandebulcke M. Characterizing the microstructural basis of “unidentified bright objects” in neurofibromatosis type 1: A combined in vivo multicomponent T2 relaxation and multi-shell diffusion MRI analysis. *Neuroimage Clin* 2014;4:649-658.
  121. Winston GP, Micallef C, Symms MR, Alexander DC, Duncan JS, Zhang H. Advanced diffusion imaging sequences could aid assessing patients with focal cortical dysplasia and epilepsy. *Epilepsy Res* 2014;108(2):336-339.
  122. Schneider T, Brownlee W, Zhang H, Ciccarelli O, Miller D, Wheeler-Kingshott C. Application of multi-shell NODDI in multiple sclerosis. 2014.
  123. Zhang H, Hubbard PL, Parker GJ, Alexander DC. Axon diameter mapping in the presence of orientation dispersion with diffusion MRI. *Neuroimage* 2011;56(3):1301-1315.
  124. Mardia KV, Jupp PE. *Directional statistics*: John Wiley & Sons; 2009.
  125. Szafer A, Zhong J, Gore JC. Theoretical model for water diffusion in tissues. *Magn Reson Med* 1995;33(5):697-712.
  126. Avants BB, Tustison NJ, Song G, Cook PA, Klein A, Gee JC. A reproducible evaluation of ANTs similarity metric performance in brain image registration. *Neuroimage* 2011;54(3):2033-2044.
  127. Haselgrove JC, Moore JR. Correction for distortion of echo-planar images used to calculate the apparent diffusion coefficient. *Magn Reson Med* 1996;36(6):960-964.
  128. Geurts JGG, Barkhof F. Grey matter pathology in multiple sclerosis. *The Lancet Neurology* 2008;7(9):841-851.

129. Cohen-Adad J, Descoteaux M, Rossignol S, Hoge RD, Deriche R, Benali H. Detection of multiple pathways in the spinal cord using q-ball imaging. *Neuroimage* 2008;42(2):739-749.
130. Mohammadi S, Moller HE, Kugel H, Muller DK, Deppe M. Correcting eddy current and motion effects by affine whole-brain registrations: evaluation of three-dimensional distortions and comparison with slice-wise correction. *Magn Reson Med* 2010;64(4):1047-1056.
131. Setsompop K, Gagoski BA, Polimeni JR, Witzel T, Wedeen VJ, Wald LL. Blipped-controlled aliasing in parallel imaging for simultaneous multislice echo planar imaging with reduced g-factor penalty. *Magn Reson Med* 2012;67(5):1210-1224.
132. Taso M, Girard OM, Duhamel G, Le Troter A, Feiweier T, Guye M, Ranjeva J-P, Callot V. Tract-specific and age-related variations of the spinal cord microstructure: a multi-parametric MRI study using diffusion tensor imaging (DTI) and inhomogeneous magnetization transfer (ihMT). *NMR Biomed* 2016;29(6):817-832.
133. Jelescu IO, Veraart J, Fieremans E, Novikov DS. Degeneracy in model parameter estimation for multi-compartmental diffusion in neuronal tissue. *NMR Biomed* 2016;29(1):33-47.
134. Nijeholt GJ, Bergers E, Kamphorst W, Bot J, Nicolay K, Castelijns JA, van Waesberghe JH, Ravid R, Polman CH, Barkhof F. Post-mortem high-resolution MRI of the spinal cord in multiple sclerosis: a correlative study with conventional MRI, histopathology and clinical phenotype. *Brain* 2001;124(Pt 1):154-166.
135. Xie M, Tobin JE, Budde MD, Chen CI, Trinkaus K, Cross AH, McDaniel DP, Song SK, Armstrong RC. Rostrocaudal analysis of corpus callosum demyelination and axon damage across disease stages refines diffusion tensor imaging correlations with pathological features. *J Neuropathol Exp Neurol* 2010;69(7):704-716.
136. Kim JH, Loy DN, Liang HF, Trinkaus K, Schmidt RE, Song SK. Noninvasive diffusion tensor imaging of evolving white matter pathology in a mouse model of acute spinal cord injury. *Magn Reson Med* 2007;58(2):253-260.
137. Ramirez-Manzanares A, Rivera M, Vemuri BC, Carney P, Mareci T. Diffusion basis functions decomposition for estimating white matter intravoxel fiber geometry. *IEEE Trans Med Imaging* 2007;26(8):1091-1102.
138. Nilsson M, van Westen D, Ståhlberg F, Sundgren PC, Lätt J. The role of tissue microstructure and water exchange in biophysical modelling of diffusion in white matter. *Magma* 2013;26(4):345-370.

139. Jelescu IO, Veraart J, Adisetiyo V, Milla S, Novikov DS, Fieremans E. One diffusion acquisition and different white matter models: How does microstructure change in human early development based on WMTI and NODDI? *Neuroimage* 2015;107:242-256.
140. Jespersen SN, Olesen JL, Hansen B, Shemesh N. Diffusion time dependence of microstructural parameters in fixed spinal cord. *arXiv preprint arXiv:170503630* 2017.
141. Veraart J, Sijbers J, Sunaert S, Leemans A, Jeurissen B. Weighted linear least squares estimation of diffusion MRI parameters: strengths, limitations, and pitfalls. *Neuroimage* 2013;81:335-346.
142. Veraart J, Poot DHJ, Van Hecke W, Blockx I, Van der Linden A, Verhoye M, Sijbers J. More accurate estimation of diffusion tensor parameters using diffusion kurtosis imaging. *Magn Reson Med* 2011;65(1):138-145.
143. By S, Smith AK, Dethrage LM, Lyttle BD, Landman BA, Creasy JL, Pawate S, Smith SA. Quantifying the impact of underlying measurement error on cervical spinal cord diffusion tensor imaging at 3T. *J Magn Reson Imaging* 2016:1608-1618.
144. Moeller S, Yacoub E, Olman CA, Auerbach E, Strupp J, Harel N, Ugurbil K. Multiband multislice GE-EPI at 7 tesla, with 16-fold acceleration using partial parallel imaging with application to high spatial and temporal whole-brain fMRI. *Magn Reson Med* 2010;63(5):1144-1153.
145. Ugurbil K, Xu J, Auerbach EJ, Moeller S, Vu AT, Duarte-Carvajalino JM, Lenglet C, Wu X, Schmitter S, Van de Moortele PF, Strupp J, Sapiro G, De Martino F, Wang D, Harel N, Garwood M, Chen L, Feinberg DA, Smith SM, Miller KL, Sotiropoulos SN, Jbabdi S, Andersson JL, Behrens TE, Glasser MF, Van Essen DC, Yacoub E, Consortium WU-MH. Pushing spatial and temporal resolution for functional and diffusion MRI in the Human Connectome Project. *Neuroimage* 2013;80:80-104.
146. Blaimer M, Choli M, Jakob PM, Griswold MA, Breuer FA. Multiband phase-constrained parallel MRI. *Magn Reson Med* 2013;69(4):974-980.
147. Larkman DJ, Hajnal JV, Herlihy AH, Coutts GA, Young IR, Ehnholm G. Use of multicoil arrays for separation of signal from multiple slices simultaneously excited. *J Magn Reson Imaging* 2001;13(2):313-317.
148. Cook PA, Symms M, Boulby PA, Alexander DC. Optimal acquisition orders of diffusion-weighted MRI measurements. *J Magn Reson Imaging* 2007;25(5):1051-1058.
149. Georgi H. Effective field theory. *Annu Rev Nucl Part Sci* 1993;43(1):209-252.

150. Villoslada P. Neuroprotective therapies for multiple sclerosis and other demyelinating diseases. *Multiple Sclerosis and Demyelinating Disorders* 2016;1(1):1.
151. Smith AK, Dortch RD, Dethrage LM, Smith SA. Rapid, high-resolution quantitative magnetization transfer MRI of the human spinal cord. *Neuroimage* 2014;95(0):106-116.
152. By S, Barry RL, Smith AK, Lyttle BD, Box BA, Bagnato FR, Pawate S, Smith SA. Amide proton transfer CEST of the cervical spinal cord in multiple sclerosis patients at 3T. *Magn Reson Med* 2017.
153. Ganter P, Prince C, Esiri MM. Spinal cord axonal loss in multiple sclerosis: a post-mortem study. *Neuropathol Appl Neurobiol* 1999;25(6):459-467.
154. Dyrby TB, Sogaard LV, Hall MG, Ptito M, Alexander DC. Contrast and stability of the axon diameter index from microstructure imaging with diffusion MRI. *Magn Reson Med* 2013;70(3):711-721.
155. Li H, Gore JC, Xu J. Fast and robust measurement of microstructural dimensions using temporal diffusion spectroscopy. *J Magn Reson* 2014;242:4-9.
156. Nilsson M, Lasič S, Drobnjak I, Topgaard D, Westin C-F. Resolution limit of cylinder diameter estimation by diffusion MRI: The impact of gradient waveform and orientation dispersion. *NMR Biomed* 2017;30(7).